Thesis for the degree
Doctor of Philosophy

Submitted to the Scientific Council of the
Weizmann Institute of Science
Rehovot, Israel

עבודת גמר (תזה) לתואר
דוקטור לפילוסופיה

מוגשת למועצה המדעית של
מכון ויצמן למדע
רחובות, ישראל

By
Yehonathan Segev

מאת
יהונתן שגב

מיקרוסקופיה מגנטית של פאזות המערבולות במוליכי על
Magnetic Microscopy of Vortex Phases in Superconductors

Advisor:
Prof. Eli Zeldov

מנחה:
פרופ' אלי זלדוב

January, 2011

שבט התשע"א

Contents

Acknowledgements

My deep gratitude is given to my mentor and advisor Prof. Eli Zeldov, for giving me the opportunity to work on the exciting projects the group works on, for teaching me how to tackle large scale projects, for offering precious insights when they were much needed and for flexibly adjusting to my irregular circumstances at the final stages of my work. Eli has taught me the value of details and of doing things thoroughly and so has given me tools that go beyond solving Physics problems.

I wish to thank Yuri Myasoedov for teaching me all the lab practices, and for always being there for me, ready to mend emergencies or help with demanding lab procedures. I also wish to thank Michael Rappaport for being a constant source of good advice and resourceful solutions. Without Michael's and Yuri's help my project might have been insurmountable.

I wish to thank Amit Finkler for being a great and synergetic partnership. I wish to thank Sarah Goldberg, for having me work the magneto-optics system in practically no time and Ilia Gutman for the collaboration on the Josephson Vortices projects.

I wish to thank Prof. Martin Huber for long hours of teaching SQUID theory and practice and Prof. Grigorii Mikitik and Prof. Ernst Helmut Brandt for a willing collaboration.

I wish to thank the Faculty professional and administrative support staff, the Cryogenics Unit, the Mechanical Workshop, the Electronics Workshop and the Condensed Matter Secretariat for doing their best to support my work.

Finally, I thank my wife Yarin, for her encouragement, practical advice and support.

List of Abbreviations

1D	one dimension or one dimensional
2D	two dimensions or two dimensional
3D	three dimensions or three dimensional
AC	alternating current
AL	Abrikosov lattice
BSCCO	$Bi_2Sr_2CaCu_2O_{8+\delta}$
CCD	charge coupled device
DC	direct current
DMO	differential-magneto-optics
FF	flux flow
FOT	first order transition
FWHM	full width at half maximum
GB	geometrical barrier
IP	in-plane
JV	Josephson vortex
MBG	moving Bragg glass
MO	magneto-optics
MOI	magneto-optical indicator
MRFM	magnetic resonance force microscope
μSR	muon spin relaxation
NSOM	near-field scanning optical microscope
NV	nitrogen vacancy
PLL	phase locked loop
PV	pancake vortex
ROI	region of interest
SC	superconductor
SNR	signal to noise ratio
SOT	SQUID on tip
SPM	scanning probe microscopy
SQUID	superconducting quantum interference device
TF	tuning fork
ud-BSCCO	under doped BSCCO
YBCO	$YBa_2Cu_3O_7$

Abstract

The study of vortices in superconductors is driven by the fact that it provides a case study for the interplay of interactions, disorder, temperature and surface effects, which result in diverse phenomena and rich equilibrium and non-equilibrium phases. Magnetic microscopy, which allows imaging single vortices seems like the ideal tool for such a study, as it provides direct knowledge of the vortex order, local density and dynamics and can distinguish thermodynamic and bulk effects from surface effects.

Recently, a novel nanomagnetic sensitive device, which should significantly widen the phase space accessible to single vortex imaging, was developed [1]. The device, which is called a SQUID on a Tip (SOT), is a superconducting quantum interference device (SQUID) made of aluminum, which is deposited on the apex of a pulled quartz tube. Its simple geometry is ideal for scanning probe microscopy (SPM) and it shows a magnetic flux sensitivity, which is as good as the state of the art SQUIDs. By mechanically coupling the SOT to a quartz tuning fork we created a composite sensor, which allows the detection of surface topography as well as the local magnetic field. This sensor was used to build a scanning SOT microscope capable of imaging local fields few nanometers from the sample surface with a sensitivity better than 1 $\mathrm{mG}/\sqrt{\mathrm{Hz}}$ and can easily image single vortices in superconductors. In a parallel effort, replacements for the aluminum superconducting film, which the SOT was made of, were sought and lead (Pb) was found to be a good candidate. By making a series of adjustments to the SOT fabrication process we fabricated Pb-SOTs, which can be used with liquid ^{4}He and have about two orders of magnitude better sensitivity— showing a spin sensitivity of 2 $\mu_B/\sqrt{\mathrm{Hz}}$.

Single Josephson vortex (JV) stacks in BSCCO were also visualized over a wide range of in-plane fields using magneto-optical (MO) microscopy. The high visibility was achieved in part by improving the way the magneto-optical indicator is attached to the sample— basically by minimizing the distance between the specimen and the magnetic sensitive sensor. As a result we were able to study the effect of Josephson vortices on the magnetic hysteresis and on the melting of the vortex lattice. We found that at elevated temperatures, the hysteresis results from the geometrical edge barrier and that this mechanism

is reduced significantly by applying a constant in-plane field. By directly imaging the barrier width, on and off the JV stacks, we were able to assert that the barrier is reduced locally on the JV stacks and managed to attribute this effect to demagnetization currents flowing along the JVs. The JV stacks also affect the melting of the pancake vortex lattice. We have found that at temperatures close to T_c the melting field is locally reduced on JV stacks by about 0.5 Oe causing melting to nucleate on the JV stacks in regions that would have been uniform in the absence of in-plane field. We have also observed that there is melting which nucleates in different regions at different fields (or temperatures) but nucleates on the same JV stack, a fact that suggests that the JV lattice is not fully destroyed by the pancake vortex melting transition.

Finally, we have used differential magneto-optics (DMO) to map the phase diagram of underdoped BSCCO and image the thermally-induced and disorder induced first-order transitions as well as the second-order glass transition. The way the phase transition propagates across the sample, as the superconductor goes through each of the three transitions, is remarkably different implying that they are affected by different types of disorder and are characterized by different length scales. Furthermore, we have found that for a given applied field the vortex density is maximal as the glass line is approached either from low or high temperatures. This suggests that the lattice energy around the transition is minimal and the effectiveness of pinning to disorder, maximal.

1. Introduction

1.1 Vortex Static Phases and Flow

1.1.1 Equilibrium Phases

Type-II superconductors (SC's) are superconductors which are pierced by vortices if a magnetic field, within a finite range, which depends on the material and temperature, is applied. The field penetrates the superconductor in form of repelling flux lines, each carrying a magnetic flux of $\Phi_0 = 20.07$ G μm^2. The supercurrents circulating the flux line give it its name— a vortex. Vortices are characterized by two lengths scales, the coherence length ξ and the penetration length λ. The former is the characteristic length scale for changes in the superconductor order parameter and defines the width of the core of the vortices where superconductivity is suppressed. The penetration length is the length scale of changes of the magnetic fields inside a superconductor. The ratio of the two scales classifies superconductors. Type II superconductors are superconductors that have a Ginzburg-Landau parameter, $\kappa \equiv \lambda/\xi > 1/\sqrt{2}$, and as a result energetically favor this breakdown of the magnetic flux into an integer number of vortices [2].

Since two vortices repel each other due to the supercurrents surrounding them, one may think that at zero temperature, a vortex system is a tightly packed ordered lattice, as described by Abrikosov in 1957 [2]. A melting transition of this Abrikosov lattice (AL) is expected at finite temperatures. As the temperature is increased the mean displacement of the vortices from their equilibrium position is increased. The elastic energy of such displacements is given by $H = 1/2\Omega \sum_{\alpha\beta} \sum_q c_{\alpha\beta}(q) u_\alpha(q) u_\beta(-q)$ where $\alpha, \beta = x, y, z$, Ω is the sample surface, $c_{\alpha\beta}$ are the elastic coefficients, and $u_\alpha(q)$ is the Fourier transform of the displacement of the vortex from its equilibrium position. The Lindemann criterion states that if the mean displacement, $|u|$, is a sizable fraction of the lattice spacing, then the lattice melts.

The AL picture is however, oversimplified. The key ingredient it overlooks is the effect of pinning to disorder. In 1970 Larkin showed that with the introduction of arbitrarily weak quenched disorder, the long range order characterizing the AL is lost [3]. Instead

there is a finite length, called the Larkin length R_a, at which the displacements are of the order of the lattice constant a. Thus, in the presence of any disorder, the perfect lattice cannot exist. In its place, at sufficiently low temperatures and pinning strengths, one finds a Bragg Glass phase [4–6], which is topologically as ordered as the Abrikosov lattice (each vortex has six nearest neighbors). In this phase, the average displacement of the vortices from their equilibrium position, $\overline{\langle [u(r) - u(0)]^2 \rangle}$, where the average is over disorder and thermal fluctuations, is diverging, but only logarithmically, resulting in quasi-long-range order.

The static vortex phase diagram is a result of the competition between elastic, thermal and pinning energies. An experimental phase diagram for $Bi_2Sr_2CaCu_2O_{8+\delta}$ (BSCCO), a high-T_c, type-II, superconductor, is shown in Fig. 1.1 (taken from Ref. 7). The figure shows the elastic dominated Bragg Glass phase at low temperature and low magnetic field, the thermally dominated liquid at high temperatures, the pinning dominated vortex glass at high magnetic field and an intermediate ordered crystal phase where, as the authors suggest, the pinning due to disorder is reduced by the temperature.

The phase diagram that is shown in Fig. 1.1 is schematically similar to what one expects in all high-T_c superconductors. There is, however, one important difference between BSCCO and other high-T_c's, such as $YBa_2Cu_3O_7$ (YBCO), for example, and it is the fact that BSCCO is strongly layered. As such, it should be theoretically treated as a stack of Josephson coupled two dimensional (2D) superconductors and the vortices should accordingly be considered as 2D pancake vortices (PVs) [8], as described in more detail in Sec. 1.2. Being layered, it also shows a stronger effect of thermal fluctuations on the lattice order, similar to 2D superconductor films. Hence, the disordered phase occupies wider portions of its phase diagram [9], making the transitions more accessible to experiment and the BSCCO crystals— excellent case studies for vortex matter physics research.

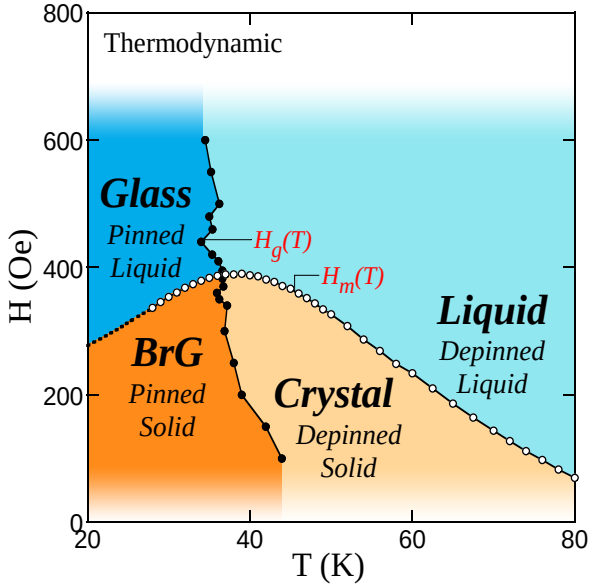

Figure 1.1: *The experimental phase diagram of BSCCO (taken from Ref. 7). $H_m(T)$ and $H_g(T)$ are the melting and glass transition lines.*

The first-order phase transition line that separates the crystalline phase from the liquid

phase is usually referred to as the melting line, $H_m(T)$. In isotropic superconductors, crossing this transition line from the disordered state to the ordered state is accompanied by a complete loss of resistivity [9, 10]. However, in BSCCO the drop in resistance is less dramatic due to very weak pinning at elevated temperatures and the resistivity in this case is mainly governed by surface properties [11]. In BSCCO, it was also found that the melting transition is accompanied by a decoupling transition where the PVs from different layers, which, in the ordered phase, are stacked forming line vortices, decouple and lose their inter-layer correlation [12].

As the temperature is decreased the first-order transition smoothly crosses over from a thermally-induced transition to a disorder-induced transition— the 'inverse melting' transition [13, 14]. At low vortex densities the vortex lattice unit cell can adjust to the pinning potential and the lattice keeps its quasi-long-range order. However, as the density grows and the average vortex spacing a, decreases, and the displacement due to the pinning becomes relatively larger, leading to a order-disorder phase transition. At low enough temperatures this transition depends only on the pinning strength and vortex density and is thus temperature independent, but as the temperature increases the vortices are pinned less efficiently, pushing the inverse melting curve to higher vortex densities [15]. In order to measure this transition, one has to overcome the vortex pinning, which is very effective at low temperatures and creates hysteresis that prevents observing equilibrium phenomena. In order to overcome this limitation, Avraham *et al.* used a strong oscillatory in-plane magnetic field in order to assist vortex relaxation, in a method called vortex-shaking, and measure this transition at equilibrium conditions [14]. Using Hall bar arrays, they measured a discontinuous jump in the magnetic induction, verifying that this too is a first-order transition. Before that, the evidence for this transition was indirect and the transition manifested itself by a sharp loss of the correlation volume, i.e., a sharp decrease in the Larkin length R_a, which indicates larger distortions to the lattice, and thus an increase of the critical current and induction irreversibility. This effect was referred to as the peak effect or second magnetization peak and was measured in BSCCO using Hall bars as well [15].

The glass transition separates the thermally dominated part of the phase diagram from the pinning dominated part at low T. It is a second-order phase transition which shows very weak field dependence at fields higher than H_m. The transition which is commonly identified with the onset of bulk pinning and the subsequent loss of linear resistance, was mapped in BSCCO, at high fields, using Hall sensors for local magnetization measurements [15, 16] and using Hall sensors to measure the self field at the low field part of the phase diagram [17]. Subsequently Hall bars were used in Refs 7, 18 to measure a kink in

$B(T)$ at the transition (i.e. a step-like discontinuity in dB/dT), giving direct evidence for the second-order nature of the transition. In his thesis, H. Beidenkopf measured the equilibrium magnetization and the self field due to an excitation current, as well as its frequency dependence. He found that the glass transition (manifested as the kink in magnetization) and the onset of bulk pinning occur simultaneously only in the limit of strictly DC currents indicating that latter does not directly reflect the thermodynamic phase transition [19].

The glass transition gets its name following the work of MPA Fisher who postulated a continuous transition where the vortex line liquid freezes, becoming a disordered glass [20, 21]. The transition into the vortex glass state is accompanied by diverging time and length scales, which result in collective pinning with diverging barriers and hence zero resistance at the limit of $J \to 0$. Experimental evidence supporting this theory was shown in YBCO, a relatively isotropic high-T_c superconductor [22–24]. However, the applicability of this idea to BSCCO is not trivial since for two dimensional superconductors the glass transition should take place only at $T = 0$. In strongly layered superconductors, such as BSCCO, this transition thus can only take place at low fields, below the decoupling transition from vortex lines to pancake vortices. The experimental results for YBCO raised some controversy as well, and it seems that the glass behavior that was reported is in fact due to the glassy behavior of the pinning at the twin boundaries (a defect, characteristic of this material) and not a trait of the true bulk superconductor [25, 26]. Thus the origin of the sharp glass transition which bisects the phase map as well as the nature of the phases at high fields are still an open puzzle.

1.1.2 Vortex Flow

If a driving current is introduced into the superconducting sample and the vortices are mobile, the current density, J, exerts a Lorentz force, $\mathbf{f}$, on the magnetic lines, $\mathbf{f} = \mathbf{j} \times \mathbf{\Phi_0}$, where $|\mathbf{\Phi_0}| = \Phi_0$ and $\mathbf{\Phi_0} \parallel \mathbf{B}$. The vortices, unless pinned by defects in the host superconductor, move with some velocity $\mathbf{v}$. This flux flow (FF) results in a resistive electric field $\mathbf{E} = \mathbf{B} \times \mathbf{v}$ and the perfect conductivity of the superconductor is destroyed.

The dynamics of the Abrikosov lattice is as rich as the equilibrium phase diagram. At low driving forces, slightly above the pinning force, some of the vortices depin and plastic vortex flux flow occurs. It is predicted by numerical simulations [27, 28] and seen in experiments [29], that the flow in this regime is very non-homogeneous, as some of the vortices stay pinned while others slip by them. The distribution of the velocity in such a flow, and therefore also the voltage noise, is wide and shows a peak at zero

frequency. As the driving force is increased relative to the pinning force, all the vortices eventually depin, but their velocity distribution remains wide and varies in space. There are many phenomena related to the plastic FF— avalanches, slip stick flow and channel formation [27, 30], some of which have been seen using Lorentz microscopy [29].

Neutron diffraction [31] and transport [32] experiments, performed at higher drives, suggest that while order is lost as the vortex lattice depins, it is restored at higher driving currents. This led to the model of dynamic melting [33], which suggests that at large velocities the system averages over disorder, and may recrystalize. Further evidence of the recrystallization picture was later given in transport measurements [34–36].

However, this model is incomplete, since it does not take into account the periodicity in the direction transverse to the vortex flow. Such a periodicity is subject to a static disorder that is not averaged out, and thus destroys the transverse order, by Larkin's argument. Refs. 37, 38 claim that at high drives, rather than having a moving lattice where the vortices follow each other in straight lines *parallel* to the driving force, the flow is in the phase of a moving transverse glass; the vortices indeed exactly follow each other in a channel flow, but the channels themselves deviate from straight lines parallel to the flow with a logarithmic divergence, similar to the static Bragg glass description. If the drive is high enough, the vortices in the channels are coupled and the flow is elastic, each vortex keeping its nearest neighbors while flowing through the sample. This elastic flow was named a moving Bragg glass (MBG). In this flow phase, a local velocity measurement will show, if we assume the sensor to be fast and small enough, a narrow peak above the channels and zero signal between them.

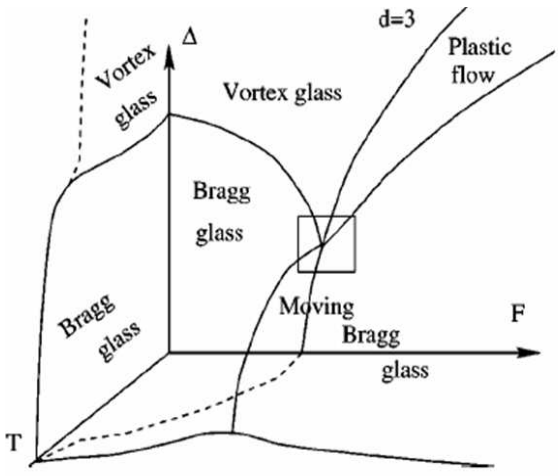

Figure 1.2: *A schematic flow phase diagram, taken from Ref. 38.* **F** *and* Δ *are the driving and pinning forces and* T *is the temperature. The crossover phase of the smectic glass is not shown for clarity.*

At intermediate drives the flux flows in a plastic moving transverse glass flow, which is known as a smectic flow. In this regime the vortices keep their beads-on-string-like channel flow, but the channels are not coupled, each having a different velocity. Here the local velocity field measurement is expected to show zero signal between the channels and a constant velocity above each channel. However, the velocity distribu-

tion in the entire sample, is expected to be wider than the MBG velocity distribution. Hence, if DC current is applied and the voltage noise is measured, the spectrum should get narrower at the crossover from the smectic flow to the MBG.

A few numerical simulations were performed to support these ideas [28, 30, 39, 40]. The predicted flow phases are shown schematically in Figure 1.2, taken from Ref. 38. Experimental evidence for the theory is, however, scarce. The MBG was probed by muon spin relaxation (μSR) and small angle neutron diffraction [41] and the existence of stable channel flow was argued to be seen by quasi-static magnetic decoration [42,43]. The latter technique, however, raised some controversy and its results are under debate. Finally, transport measurements measured the broad-band noise associated with the plastic flow and the narrow band noise at the washboard frequency, ν, associated the movement of a periodic system in a random potential [44, 45],

$$\nu = \frac{v}{a} \tag{1.1}$$

where v is the average lattice velocity, and a is the lattice spacing. While the existence of broad-band noise at the plastic flow regime was shown unambiguously, the source of the washboard frequency noise and its association to a smectic or ordered phase are not clear [46].

These open questions and the lack of the experimental data lead us to set the vortex dynamic phases as the designated target of research for the SQUID-on-tip microscope we were developing.

1.2 Introduction to Crossing Lattices

The hypothesis that in highly anisotropic, layered superconductors, vortices due to fields parallel and perpendicular to the layers are different than those in isotropic SC's dates back to the early 1990's [47–49]. The argument is quite straight-forward if we consider these superconductors as stacks of two-dimensional superconductors interacting through Josephson coupling. Magnetic fields normal to the layers cause vortices in the form of stacks of two dimensional vortices with a disc-shaped normal core, which gave them the name pancake vortices [8]. The PV tendency to stack in a column results from the attractive magnetic interaction of PVs in different layers and from the Josephson coupling. Since the PVs in the same layer repel each-other, a layered Abrikosov lattice is formed. In contrast, if the layer spacing, s, is larger than the coherence length in the perpendicular direction $\xi_z = \xi_\parallel/\gamma$, where γ is the anisotropy parameter, then the normal core of a vortex due to magnetic field parallel to the layers can be *between* the planes. This way the high energetic price of having the normal core crossing a superconducting plane can be avoided. As a result the vortices formed by a parallel magnetic field cause Josephson vortices (JVs) that have no normal core within the superconducting layers. The currents they induce in the layers cause them to repel each other, so they also form an Abrikosov type lattice, although highly-distorted and oblate, due to the superconductor's anisotropy. Hence, for an applied magnetic field that has two components, in and out of the plane, two lattices will form and the superconductor will acquire a *crossing-lattice* state. The first experimental evidence of such a state was seen using Bitter decoration in 1991 [50].

About a decade later it turned out that the description above is too simplistic and that the two lattices interact, forming a very rich and diverse phase space [51–56]. In Ref. 51 the author observed that the currents induced by a JV in the superconducting planes above and below it exert a Lorentz force on pancake vortices in these planes, pushing them in opposite directions (see Fig. 1.3 c). The energy of a PV in the n'th layer displaced by u_n from its rest position due to the sheet current j_n has two components, the Lorentz potential term, $-\frac{s\Phi_0}{c} j_n u_n$, and a spring-like, restoring term which is positive and quadratic in u_n. For small displacements the linear term will dominate and therefore the energy of a PV stack is lowered by the JV crossing and the PV stack is attracted to the JV. The PV displacement also causes an attractive dipole-dipole interaction between PVs on the same JV stack leading to an increased density of PV stacks on the JVs [54].

Thus, PVs in a superconductor with a high enough anisotropy under a finite in-plane magnetic field, have few configurations depending on the PV density. For a small H_z, the PV stacks enter the sample only on the JVs and the sample acquires a *chain state*.

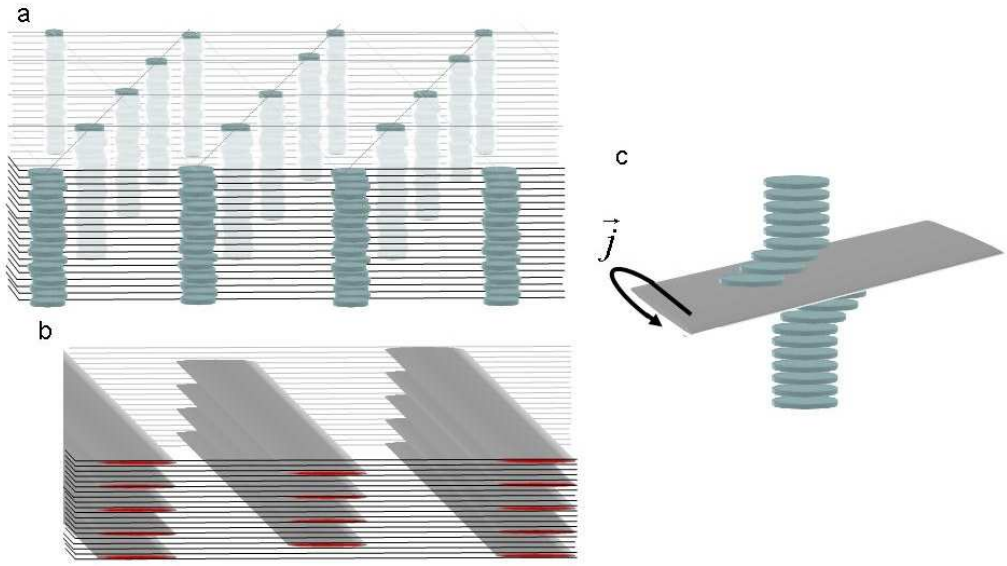

Figure 1.3: *A schematic image of the vortex lattice in layered superconductors. (a) The pancake vortex lattice due to an out-of-plane field. (b) The in-plane Josephson vortex lattice. (c) The interaction of a JV with a PV stack that causes a deformation to the latter.*

At higher H_z and higher PV densities, PVs leak out of the chains and form stripes of Abrikosov lattices between the chains (*mixed- chain and lattice state*). As H_z is further increased the configuration continuously crosses over to a *modulated Abirkosov lattice* where each JV contains a few (or more) PV rows ordered in a lattice but slightly displaced from their equilibrium position. At high enough H_z when the field is almost normal to the superconducting planes the JV are no longer stable and a *tilted lattice* configuration is assumed.

The early experimental work used Bitter decoration to get "frozen" images of the crossing lattice state [50,57]. As the theory developed more experiments were done and the different vortex configurations were visualized using scanning Hall probe microscopy [58, 59], Lorentz microscopy [60] and magneto-optics [61–63]. Very few experiments were done, however, other than those intended for the verification of Koshelev's theory of crossing lattices. As we show in Section 3.3, one can image the JV stacks using magneto-optical microscopy. We take advantage of this and aim our research at the study of the effect of the JVs on well established vortex phenomena that were studied without considering, theoretically or experimentally, the effect of the underlying JV lattice. Specifically we consider the effect of the JVs on the magnetic hysteresis (Section 4.1) and on vortex melting (Section 4.2).

1.3 Introduction to SOTs

The superconducting quantum interference device (SQUID) can be used as an extremely sensitive magnetometer and as such it is often used for the study of superconductors. Its scanning versions, the scanning SQUID microscopes, are sensitive enough to resolve single vortices and are thus an effective tool for the study of vortices in superconductors [64]. In this section the basic principles of SQUIDs are reviewed followed by a description of the novel SQUID-on-tip sensors— a new design for a SQUID, which is ideal for scanning applications.

1.3.1 SQUIDs

As its name implies, the superconducting quantum interference device measures the interference of two superconducting wave functions, connected by two weak links, or Josephson junctions [65], whose phases are modulated by the magnetic flux they enclose. The SQUID is used as a very sensitive magnetometer by measuring $I_c(B)$, the maximal current that can flow through it without dissipation— a quantity, which is highly dependent on the magnetic induction. The idea is sketched below very briefly (more detailed discussions may be found in many texts; e.g. 66, 67).

Following the Ginzburg Landau theory [68], one assigns a macroscopic wave function $\psi_j = \sqrt{n_j}\exp(i\theta_j), j = 1, 2$ to two superconducting slabs connected by weak links, where n_j is the Cooper pair density and θ_j is the phase of the wave function describing slab j. According to the Schrödinger equation, the time evolution of the wave functions can then be described by [69]

$$i\hbar\frac{\partial}{\partial t}\begin{pmatrix}\psi_1\\ \psi_2\end{pmatrix} = \begin{pmatrix}U_1 & K\\ K & U_2\end{pmatrix}\begin{pmatrix}\psi_1\\ \psi_2\end{pmatrix}, \tag{1.2}$$

where U_j and K are the energy and the coupling of the wave functions in the superconductors, respectively. By diagonalizing this simple matrix, taking the zero energy to be halfway between U_1 and U_2 so that $U_1 = -U_2 = -V$, and substituting $J = -2e\frac{\partial(n_1-n_2)}{\partial t}$, one obtains the Josephson relations,

$$J = J_c \sin\phi \tag{1.3}$$

$$\frac{\partial\phi}{\partial t} = \frac{2e}{\hbar}V \tag{1.4}$$

where J_c is the maximal current that may flow between the two superconductors without dissipation and ϕ is the phase difference of the two wave functions. J_c depends on the

quantity K, which depends on the junction geometry, material and temperature and can be derived in some cases from the microscopic BCS theory. The phase difference should be defined in a gauge invariant way if magnetic fields are introduced:

$$\phi = \theta_2 - \theta_1 + \frac{2e}{\hbar}\int_1^2 \overrightarrow{A}(x,t)\cdot\overrightarrow{dl}. \tag{1.5}$$

The last equation shows that with the introduction of a magnetic field, the (gauge invariant) phase difference between the two slabs is not constant in space, and thus through Eq. (1.3) neither is J. If the junction is extended (compared to the penetration depth λ), the maximal critical current $I_c(B)$ through a junction is given by the integral of the critical current density $J(\mathbf{r};B)$ across the junction. One can show that, similar to Fraunhofer diffraction, the maximal dissipationless current through the junction is given by the Fourier transform of a function describing the transmission of the junction, $J_c(\mathbf{r})$. If we consider the junction to be in the yz plane and the magnetic field pointing in the z direction, by defining the one dimensional maximal current density $J_c(y) = \int J_c(y,z)dz$, the maximal current at zero voltage through the junction reduces to

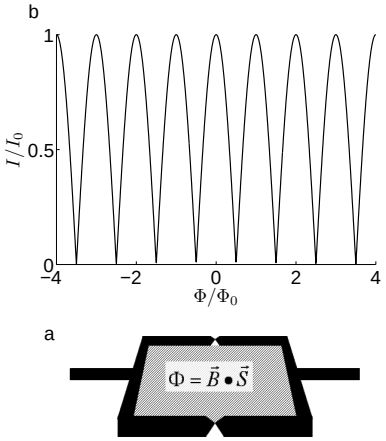

Figure 1.4: *A simple description of a SQUID loop with 2 point like weak links (a) and the corresponding two slit interference pattern (b).*

$$I_c(B) = \left|\int_{-\infty}^{\infty} J_c(y)e^{i\beta y}dy\right|, \tag{1.6}$$

where $\beta = 2e(2\lambda + d)B/\hbar$ and d is the junction width.

The simplest description of a SQUID loop is a loop with two equal point-like weak links (Fig. 1.4a). Let the SQUID loop plane be the xy plane, and the magnetic field perpendicular to it in the z direction. The two weak links can be thought of as one extended junction at the yz plane, with two delta-function like points of non-zero transmission at $x, z = 0,\ y = \pm w$, so that $J_c(y) = I_0/2\,(\delta(y-w) + \delta(y+w))$. Thus, the critical current dependence on the magnetic field is given by a sinc-function, similar to a two slit interference pattern (see Fig. 1.4b). A more realistic description considers slits of finite width that add a decaying envelope to the interference pattern.

1.3.2 SQUID-on-Tip Sensors

Most of the magnetic microscopy techniques available for imaging weak fields with high spatial resolution are variants of scanning probe microscopy (SPM, described in Sec. 2.1). The exceptions to this rule, namely, Lorentz microscopy [29, 60, 70, 71], Bitter decoration [72–74], and magneto-optics [75], are less sensitive and allow imaging single vortices only at relatively low magnetic fields [76]. The SPM methods utilize a very small and sensitive magnetic sensor to scan the surface of a magnetic specimen from a very short distance, and map the magnetic field point by point. In order to image magnetic fields on the sub-micron and nanometer scale, the magnetic sensor should have both high field sensitivity and high spatial resolution. A relevant quantity that classifies the nanomagnetic sensors is their sensitivity to the electron spin, which is measured in units of Bohr magnetons per square root Hertz, $\mu_B/\sqrt{\text{Hz}}$. This sensitivity depends on the probes' field sensitivity, the typical probe-dipole distance (the working distance), and the ratio of the spin characteristic length $r_e = 2.82 \times 10^{-15}$ m, and the pickup-loop size.

A common approach to making submicrometer magnetic sensitive probes is to fabricate field sensitive devices (Hall probes [77] and SQUIDs [78, 79]) on a flat chip's corner. Small sensor-sample distances are achieved, in these chip-based techniques, by tilting the sensor relative to the sample by a small angle, so that the chip's corner defines the distance. The sensor, which is close to the corner is therefore close to the sample. The working distances in these techniques are limited by the geometry of the chip to the order of 1 μm. This distance, which is more than two orders of magnitude larger than the sensor-sample distance in tip based scanning probe microscopes, lowers the probe dipole sensitivity. High standoff heights also limit the ability to resolve vortices at high densities (fields) or high acquisition rates since the modulation of the magnetic field above a vortex lattice is exponentially dependent on the height above the sample [80] (with the vortex spacing as the characteristic decay length). The standoff height dependence of a simulated vortex

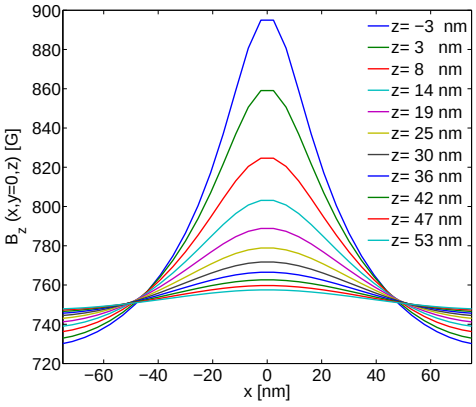

Figure 1.5: *The magnetic field due to a single vortex at various heights from the sample's surface. The abscissa represents a transverse direction on the sample surface, with a vortex located at $x = 0$. The parameters of the simulation fit a 1.6 μm thick $NbSe_2$ crystal ($\lambda = 1323\text{Å}$) at an applied field of 750 Oe. The vortex lattice constant is $a_0 = 160$ nm.*

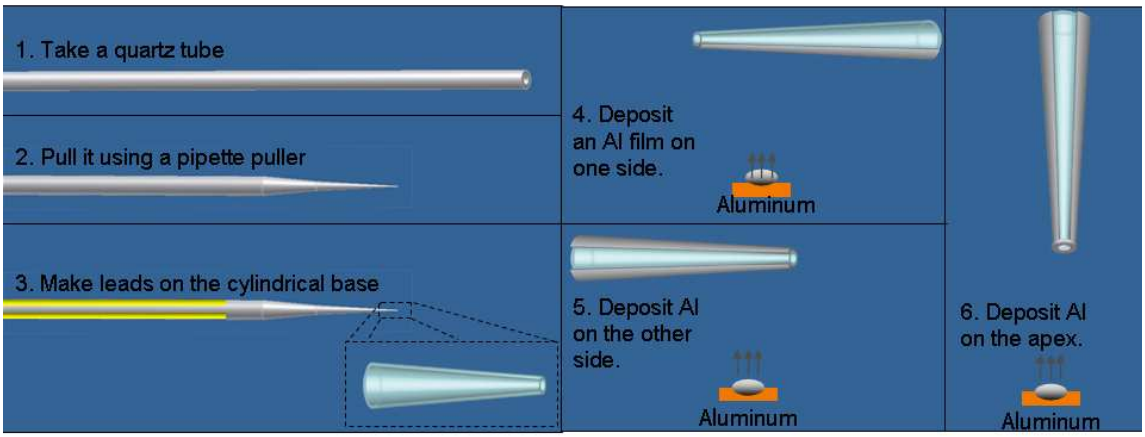

Figure 1.6: *The simple 6 step recipe for making an SOT.*

signal is shown in Fig. 1.5. A thumb rule given by Refs 76, 81 is that one can only image vortices if their spacing is larger than the sensor-sample distance.

Another approach to increase field sensitivity while keeping the dimensions small is to use resonant probes. The simplest example is the magnetic force microscope which uses a resonating cantilever to detect the magnetic force between its ferromagnetic tip and the sample. The magnetic resonance force microscopy (MRFM) [82] uses the same principle to measure nuclear and electron magnetic resonances in a method that currently holds the record for spin sensitivity with a spin sensitivity less than $0.1\mu_B/\sqrt{\text{Hz}}$. Recently, the nuclear magnetic resonance in nitrogen vacancies (NV) in diamond [83–85] were also shown to be very sensitive and are also expected to be able to detect single spins. The main drawback of the techniques based on magnetic resonance, on top of the obvious experimental complexity, is their limited bandwidth, which makes them unsuitable for some experiments and in particular the study of vortex dynamics.

Compared with the SQUIDs usually used for scanning applications the SQUID-on-tip (SOT) sensor we have developed in our lab has much simpler design. While the former are fabricated using a multilayered lithography process and complex etching methods to ensure the proximity of the device to the substrate corner [79], our sensors rely on the geometry of the substrate— a pulled quartz tube — to form a SQUID device, which is located inherently on the apex of a sharp tip. The SOT sensors are made by depositing a thin superconducting film on two sides of the tip and then on the tip apex as shown in Fig. 1.6. The SQUID device has two Dayem-bridge-type weak links as is shown in the schematic two dimensional unfolding in Fig.1.7a. The size of the SQUID is set by the size of the pulled tube, which is tunable in the range of about 50–500nm. The SOTs are an ideal sensor for nanomagnetic imaging, because their lateral size is small, their sensitivity

is high and their shape allows bringing the SOT pickup SQUID loop very close to the sample surface.

As shown in the inset of Fig. 1.8, the SOTs are voltage driven by putting an $R_b \approx 1\Omega$ resistor in parallel with the SQUID, and the current through them is measured using a SQUID array amplifier [86], which is inductively coupled to the SOT circuit branch. Typical $V - I$ curves are shown in Fig. 1.8a. At low voltage the current through the SOT branch is lower than the SOT critical current and most of the driving current flows through this branch giving a linear $V - I$ dependence, whose slope is dictated by the parasitic series resistance R_s and the shunt bias resistance R_b. Slightly above the critical current, the DC average of the current oscillations at the Josephson frequency shows up as negative differential resistance in the $V - I$ curve. At high drives the SQUID is Ohmic and the V-I curve increases linearly (not shown).

The first SOTs we have made and the ones which we based our first scanning microscope on, are made of aluminum. A color plot of the $V - I$ curves for different applied magnetic fields is shown in Fig. 1.8b, which clearly demonstrates the pronounced critical current oscillations. The field sensitivity at the sensitive bias point is of order 1 mV/G, which translates to a field sensitivity of 1 mG/$\sqrt{\text{Hz}}$ in our measurement system. In terms of spin sensitivity the Al SOT shows a sensitivity of $70\mu_B/\sqrt{\text{Hz}}$ at 10 kHz , assuming the spin is located less than 100 nm from the SOT [1] under the loop center. The critical current oscillations are apparent at fields as high as 5000 G, which means that SOTs can be used up to relatively high fields. Another important characteristic of the SOTs is that they are asymmetric with respect to the polarity of the bias voltage. This asymmetry is a significant advantage since it allows the SOT to be sensitive practically in any applied field by choosing a correct biasing point.

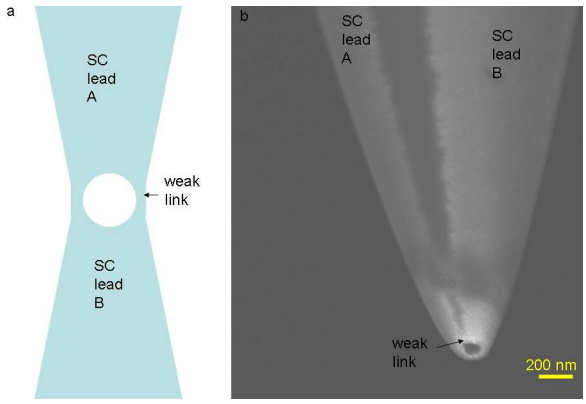

Figure 1.7: *(a) A schematic 2D unfolding of an SOT. (b) An SEM image of an aluminum SOT.*

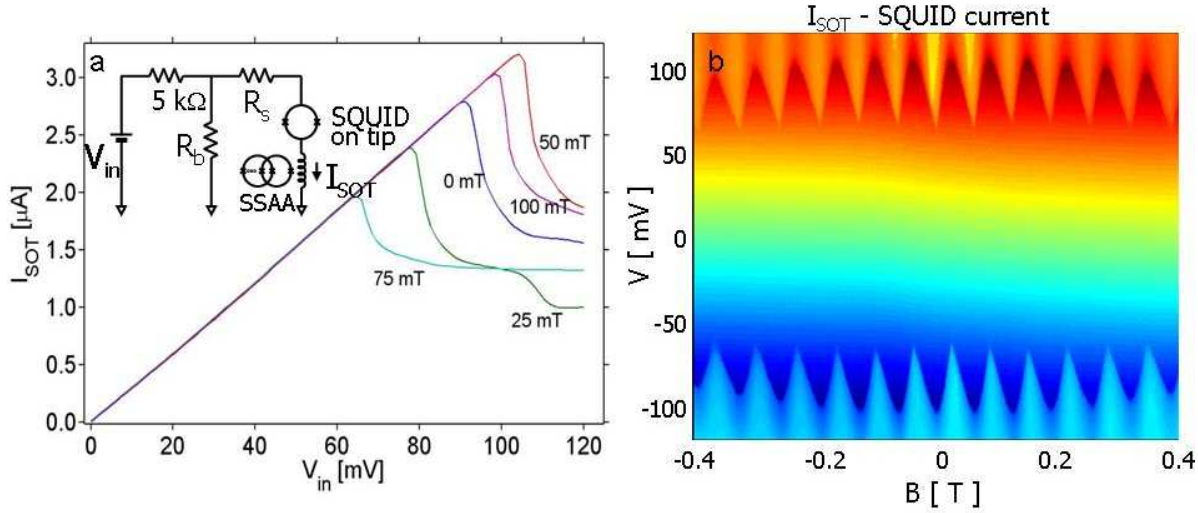

Figure 1.8: *(a) Aluminum SOT V-I characteristic curves at various applied fields. Inset: SOT measurement circuit. (b) False color plot of the SOT current vs. applied field and bias voltages showing the quantum interference pattern typical of SQUID devices. The color scale corresponds to* -3 μA *(blue) to* 3 μA *(red).*

2. SOT Project Methods and Results

The goal of my research was to develop a scanning SQUID microscope based on the SQUID-on-tip sensor that we were developing, in parallel, in our lab and then to use it and study vortex dynamics. Although the first part of the project, namely the development of the microscope, was completed, the second was not due to time limitations. Due to the developmental nature of this project the methodology and the results are presented below together.

2.1 Scanning Probe Microscopy

In order to extract a magnetic image using our SOTs they should be incorporated in a scanning-probe-microscope type setup. These microscopes are schematically quite simple and conceptually are all similar to the design of our SOT microscope, which is described next and shown schematically in Fig. 2.1. The heart of our microscope consists of a rigid cylinder (not shown), which supports the sensor assembly on one side and the sample assembly on the other. The sensor assembly is fixed directly to the flange, while the sample assembly is mounted on top of a commercial stack of piezo-electric motors and scanners (by Attocube AG), which allows for a motion of the sample relative to the sensor. This stack consists of three stepper motors with a typical step size ranging from a few nm's to about a micron, intended for coarse alignment in the three spatial directions. Additionally there is a piezo scanner which allows three axes precise scanning with a sub-nm resolution and a scan range of 30 μm in the lateral directions and 15 μm in the so called z axis—perpendicular to the sample. In this way a magnetic pseudo-image can be extracted by scanning the senor relative to the sample (or vice versa) and extracting the magnetic field in a pointwise manner.

Since the measured field depends strongly on the sensor-sample distance, at least in the range where the former is interesting, one needs to be able to control it with high accuracy and stability. Thus, in all scanning probe microscopes there is some method of detecting the sample topography. A topography sensor is also needed for the initial

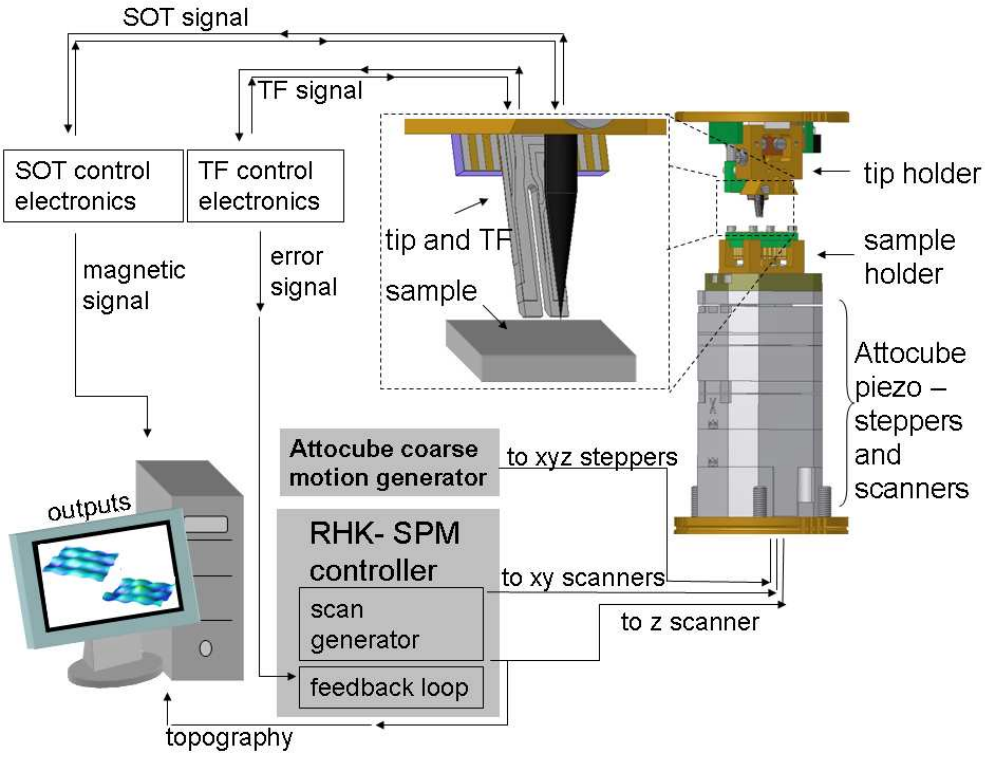

Figure 2.1: *The scanning SOT schematic setup. The SOT and tuning fork are mounted together on one support flange. The sample is mounted on a flange on the other side of a rigid support cylinder (not shown) on top of a tower of modular coarse and fine piezo actuators by Attocube AG which enable the relative sample-probe displacement. Closed loop control of the height above the sample is possible by feeding back the TF resonance frequency or amplitude to the "z axis" piezo scanner (perpendicular to the sample). The feedback loop is a sub-system of the main SPM controller, which also does the scan generation and, through the host computer, also the data collection. The output images are the magnetic and topography signals plotted in pseudo-color or gray scale for each scan point.*

procedure of getting the sensor close to the sample in order to prevent tip crashes. In our microscope the SOT is attached to a quartz tuning fork, which acts as a topography sensor and a signal from its readout electronics is fed back to the z scanner in order to maintain a constant height.

2.2 Tuning Fork Microscopy

Tuning forks (TF's) are piezoelectric oscillators, which have a well defined and sharp resonance frequency and can therefore be used as very precise force sensors. They have been first used in microscopy in near field scanning optical microscopy (NSOM)

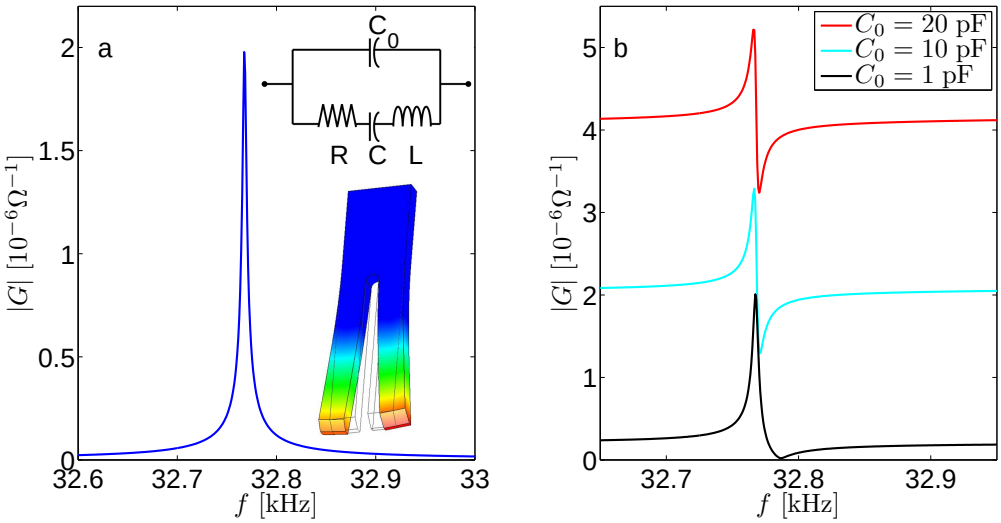

Figure 2.2: *(a) The electric signal from the tuning fork resonance is equivalent to the resonance of the capacitively-shunted RLC circuit shown in the inset. A TF resonating at the main resonance peak, the first planar antisymmetric mode (shown in the inset), with $f = 32768$ Hz and $Q = 8.6 \times 10^3$ is equivalent to the following circuit parameters, 0.5 MΩ, $L = 20.5$ kH, $C = 1.15$ fF. Here the stray capacitance is negligible, $C_0 \ll C$, so the peak has the shape of a Lorentzian. (b) For larger values of C_0 the shape of the resonance peak gets distorted and decreases while the off-resonance, background, signal increases.*

in 1995 [87], and are now widely used in all types of SPM's. The oscillators we use are small, 0.3 mm × 0.6 mm × 6 mm, commercial quartz tuning forks designed to give a time base for digital clocks. Their main oscillation mode is the first planar asymmetric mode as illustrated in the inset of Fig. 2.2a, which has the nominal resonance frequency of $2^{15} = 32768$ Hz. Since the TF's are made from single crystals of piezoelectric quartz, their mechanical resonance gives an electrical resonant signal, which can be very well approximated by a capacitively shunted RLC element as shown in inset of Fig. 2.2a. The actual values of the equivalent RLC components depend on the exact tuning fork geometry, which may vary for different manufacturers, and the damping due to a glued tip. The simulated resonance curve shown in Fig. 2.2a is characteristic of a TF with a glued tip [88] and has $R = 0.5$ MΩ, $L = 20.5$ kH, $C = 1.15$ fF and negligible $C_0 \ll 1$ fF resulting in resonance frequency of $f_0 = 1/2\pi\sqrt{LC} = 32.76$ kHz and a quality factor $Q \equiv f_0/\mathrm{FWHM} = 2\pi f_0 L/R = 8550$, where FWHM is the full width at half maximum of the resonance peak. Bare tuning forks in vacuum typically have Q factors, which are larger by an order of magnitude and accordingly smaller values of R. The value of the shunt capacity C_0 depends on the measurement setup and the wiring as is discussed below.

When a tuning fork (or a tip well-coupled to it) is brought close to a specimen the latter exerts dissipative and reactive forces on the tuning fork which alter its resonance—

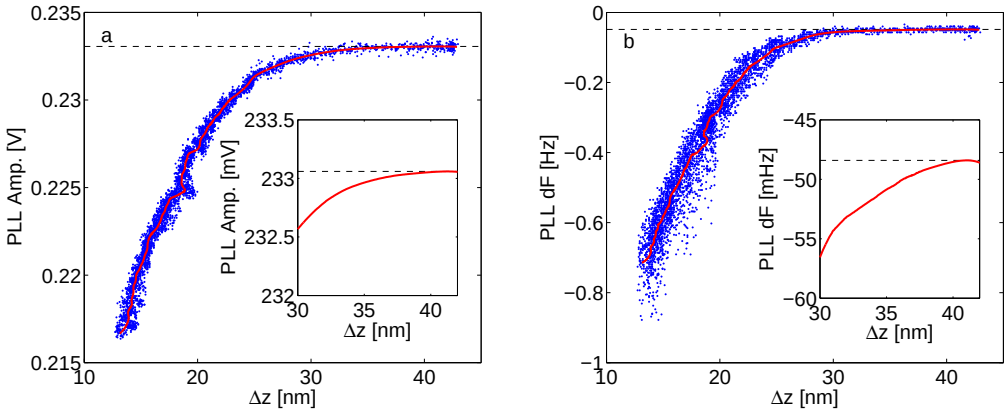

Figure 2.3: *The resonance amplitude (a) and frequency (b), of a tuning fork and an SOT at 300 mK, as measured by a phase locked loop (PLL) as the distance to the sample is modulated by modulating the set-point of the height feedback loop (blue dots). The red curve is extracted from the blue data points by smoothing using second degree local regression. The black dashed line is the maximum of the red curve and represents the behavior of the TF far from the sample. The width of the marker scatter corresponds to the experimental error. In this measurement, due to a high off-resonance signal, we did not bring the TF to the point of full sample - probe contact (where the amplitude approaches zero). By comparison to Ref. 88 we have estimated the position of the sample surface and have shifted Δz so that $\Delta z = 0$ represents the surface position. The insets show closer views of the plots at the Δz region where the resonance starts sensing the sample.*

changing the resonance frequency and reducing its amplitude and Q factor. Each one of these three signals can be used as an error signal for the topography feedback loop. An example of the dependence of the resonance amplitude and frequency on the distance to the sample surface is shown in Fig. 2.3. The figure shows data which we have collected at 300 mK, with our SOT coupled to a TF at contact with the sample. In these measurements, the resonance frequency shift served as the error signal for the z piezo feedback loop while its setpoint was modulated at about 0.1 Hz and the corresponding shift in the resonance amplitude, frequency and z piezo extension were recorded at a high rate. The measurement points are seen as blue dots in the plot, the red curve is extracted from them by smoothing using second degree local regression and the black dashed line is simply the maximum of the red curve and represents the behavior of the TF far from the sample. The insets of the two plots show close ups on the resonance parameters at a relatively high sample sensor distance (showing just the averaged curve for clarity). The figure demonstrates the sharp change in the resonance parameters as the sample surface is approached. Note that this measurement was not pushed to the limit of the amplitude going to zero, which represents full TF-sample contact and so the interaction range cannot be extracted from it. However, by comparing this data with the one shown in Ref. 88, we can estimate

a probe-surface interaction range of about 40 nm. The figure also demonstrates that the amplitude and frequency bith start deviating from the $\Delta z = \infty$ behavior (dashed line) at the same distance, $\Delta z \approx 40$ nm. However, in some other measurements we have done, and also in Ref. 88, the amplitude seems to have a longer range than the frequency shift. This can be expected from electronics that have fixed frequency resolution and tuning forks that might have significantly lower Q factors. The frequency change of these TF's, which have much broader resonance is harder to detect. The scatter width of the data points results from microscope vibrations whose amplitude and main frequency can be extracted from the raw time domain curves (not shown), $\delta z_{\text{vib}} = 1$ nm (peak to peak) at $f_{\text{vib}} \approx 25$ Hz. The amplitude of the vibrations of the whole microscope structure (and cryostat) has been reduced by about two orders of magnitude after it was mounted on a one ton marble block resting on pneumatic legs and enclosed in a sound proof enclosure.

2.2.1 Tuning Fork How To's

Obviously, when an SPM probe is coupled to a TF it damps it, and typically great care should be taken in order to find the correct way to strongly couple the two together without damping the TF completely. There are two geometries that are typically used to couple the TF to a probe. The conventional shear mode has the probe glued to the TF in parallel with the long axis of the TF inducing a tip motion in the xy plane [87]. In this geometry, the induced oscillation is the one shown in the inset of Fig. 2.2a and is characterized by a node at the TF base where the latter is fixed. The tip mass and stiffness break the symmetry of the two TF prongs and may cause a displacement of the node relative to the TF base causing a broadening of its resonance. Thus, one has to make sure that minute amounts of glue are applied and that the probe that is used should be very light. If it is long and heavy, as is our tip (and also the optical fiber used in NSOM's), the probe should be flexible enough and supported separately. Alternatively, one can use a tapping mode [89] where the probe is mounted on one of the prongs perpendicular to the TF long axis and the other prong is cemented firmly to a heavy base. This geometry breaks the symmetry of the two prongs completely and has the TF prong oscillating in a cantilever mode. The resonance in this mode is not damped due to mass imbalance. However, it is damped when coupled to large probes that are independently supported, since the tip motion, induced by the TF, is parallel to its symmetry axis tending to move the tip up and down in contrast to the lateral movement induced by the shear configuration. In both modes one should make sure that energy is efficiently transferred from the tip apex to the point where it is coupled to the TF, otherwise, the effect of the surface will not be

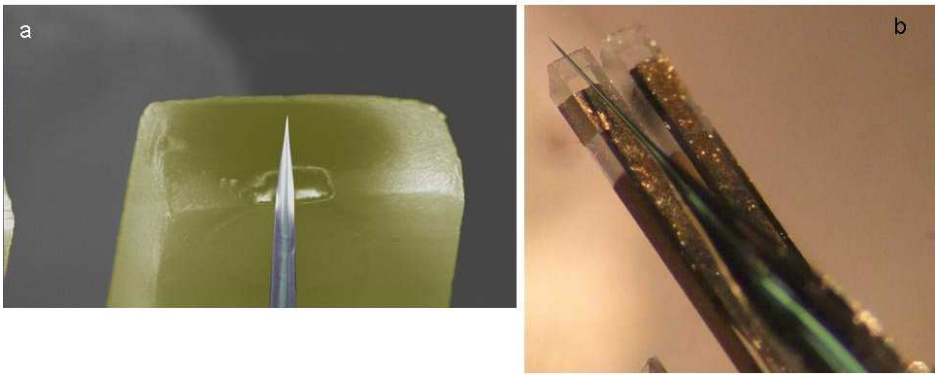

Figure 2.4: *False color SEM image (a) and optical picture (b) of a tip glued to a tuning fork.*

transferred to the TF. Practically, this means that the mounted probes should be either rigid or they should extend only slightly above the TF.

The TF-probe coupling is especially challenging in our case since the tip is much larger and heavier than the TF so it cannot be simply mounted on the TF. Furthermore, the tip's conical shape makes it very stiff far from the tip apex and very flexible close to it. This means that gluing the tip far from the apex will dampen the TF strongly while keeping the TF weakly coupled to the surface. Thus in order to couple our SOTs to a TF the two had to be supported separately by a tip holder that allows careful mutual alignment. The actual alignment and gluing have to be done under a microscope. Two examples of SOTs coupled to a TF are shown in Fig. 2.4 and the TF-SOT holders are shown in Fig. 2.6 and discussed further in Section 2.6.

Apart from the geometry, the TF resonance obviously depends on the environment, namely the external pressure and temperature. Its Q factor deteriorates when it is driven in atmospheric pressure rather than in vacuum, and it is even worse when in liquid. On the other hand, it is nearly an order of magnitude higher at cryogenic temperatures $T \lesssim 4K$ than at room temperature (as can be seen in Fig. 2.5a).

The shape of the resonance curve is also affected by the measurement setup. The typical way to measure the TF resonance is to use the TF readout electronics to drive it using voltage bias and reading the current through it using a current amplifier. This measurement is equivalent to measuring the admittance of the RLC circuit shown in the inset of Fig. 2.2a, and can be highly distorted due to the stray capacitance, C_0. As shown in Fig. 2.2b, even very small values of C_0, similar to what can be expected from stray capacitance of wiring, cause a significant distortion to the resonance curve. This effect,

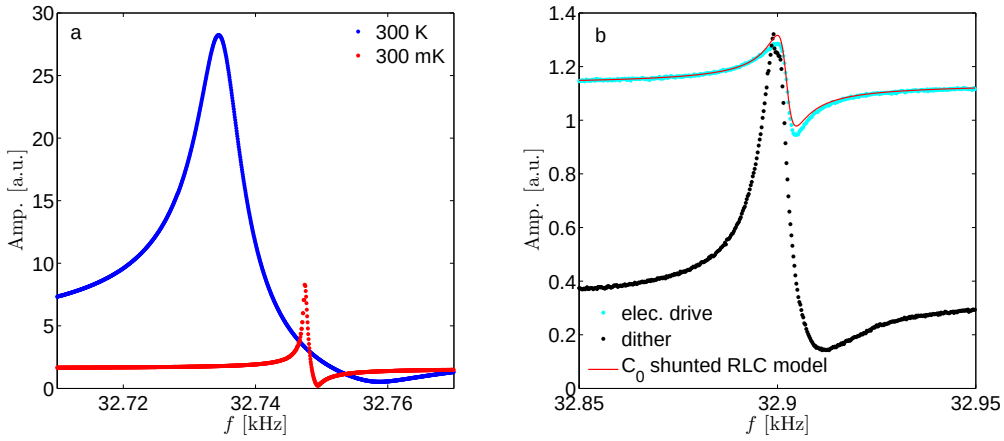

Figure 2.5: *(a) Comparison of the tuning fork resonances at room temperature and at 300 mK with a dither drive. (b) The resonance of the same tuning fork at 300 mK with a dither drive (black) and electrical drive (cyan). The red curve is the resonance of a series RLC circuit, shunted with a capacitor C_0, with $L = 1.8$ kH, $R = 53.2$ kΩ, $C = 13$ fF, $C_0 = 0.31$ nF and $Q = 7000$.*

which lowers the peak amplitude and increases the background, off-resonance, signal, thus lowers the resonance signal to background ratio and can dramatically reduce the sensitivity of the tuning fork. Even if the peak is high enough to be used for a stable feedback loop when the sensor is far from the sample, it will probably lose stability as the amplitude of the resonance will decrease due to the approach to the sample. The simplest way to avoid this effect is to use wiring schemes that minimize the leads' mutual capacitance, for example by driving the TF by *two* coaxial lines, and avoiding carrying its signal by a single coax or a single twisted pair. One can also use a tunable external capacitor, or a capacitance bridge, in the circuit shown in Ref. 88 to cancel this effect. But as Fig. 2.2b shows even at $C_0 = 1$ pF the signal is already distorted while the effect of bad wiring can be as high a few hundred pF (see e.g. Fig. 2.5b) and so this should be used either with a precise bridge that allows promille resolution or with a common single turn trimmer after the main effect was corrected by proper wiring.

Another way of avoiding the problem of stray capacitance is avoiding measuring the admittance of the TF and instead mechanically exciting the TF and measuring its voltage. In this case the TF is better viewed as a voltage source and the voltage across it should be independent on any parallel capacitance. In this measurement scheme the excitation signal from the TF electronics goes to a dither piezo and the wires going to the TF are used for the measurement of the voltage across it. As shown for example in Fig. 2.5b, the dithering driving scheme gives resonance curves that have a high signal to noise ratio and thus a high sensitivity to the surface.

2.2.2 Tuning Fork Electronics

Tuning forks can be driven either with Lock-in amplifiers or with designated electronics. In both cases, since the resonance can be narrower than 1 Hz the electronics should have at least a 0.1 Hz resolution at 33 kHz in order to measure it. When using a Lock-in amplifier the amplitude at a constant frequency is measured. This means that a Lock-in amplifier can be used only in the range where the frequency shift is smaller than roughly half the resonance width meaning that it can be used only in a limited sample-probe distance range or with TF's with low Q factor. Otherwise, if the amplifier frequency is set to the resonance frequency when the probe is far from the sample, when the probe gets to the distance where its frequency shifted by half the resonance width the amplifier will be measuring the flat off-resonance signal. As an example, we see that Lock-in amplifiers can be used in our system with the TF shown in Fig. 2.3 up to a range of about 10 nm from the sample surface, where the frequency shift is roughly equal to the FWHM.

Phase lock loops (PLLs) for microscopy are designated electronics units that get around this obstacle by continuously tracking the resonance frequency. This is achieved by employing a feedback loop that tends to keep the phase between the excitation signal and the detected signal constant by varying the excitation frequency. The PLL outputs the frequency shift relative to a reference frequency (say, the frequency when the tip is high above the surface), the amplitude of the resonance frequency and the dissipation, which relates to the ratio of the excitation and detected signals. It can also work in a mode of constant signal and then the excitation amplitude is returned rather than the resonance amplitude. Each one of these signals can be used as an error function for the height feedback loop.

2.2.3 SOT and TF Holders

As was explained above the tip and tuning fork holder had to be designed such that the two are supported independently, both have electrical contacts and their fine mutual alignment is possible. This is achieved by supporting the SOT between its two readout electrodes and mounting the TF on a small slider block on two rails that are fixed to one of the SOT electrodes. The control of the displacement of this block is done by turning two fine (1 mm) screws. As our experience with making SOTs increased we have understood that the SOT should be made in the same holder that they will be measured in, otherwise the SOT have a high probability to burn due to static discharge during the handling. While making Pb SOTs we have also learned that the SOTs need to be cooled by liquid nitrogen while being deposited on, so that the lead percolation threshold will be

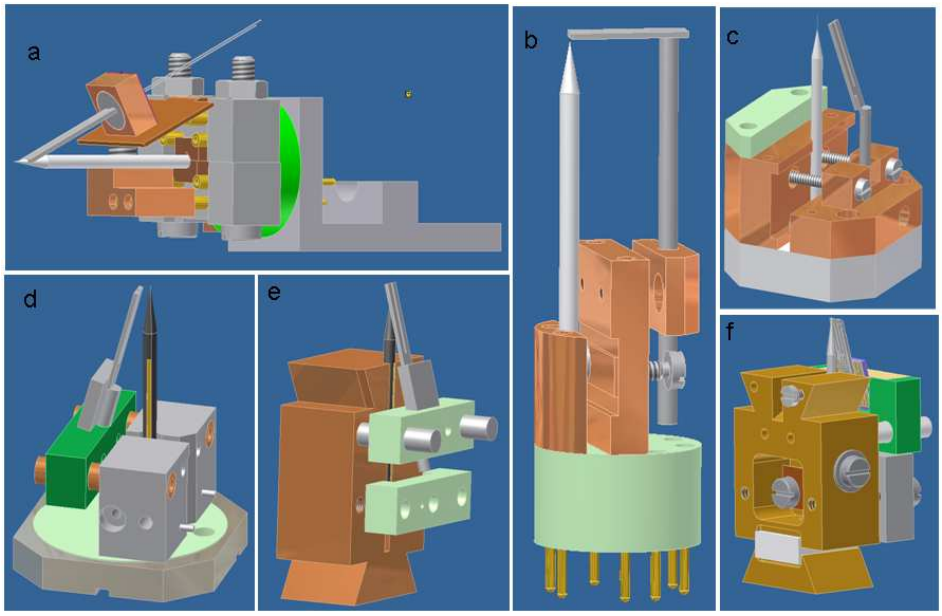

Figure 2.6: *Some of the versions of the SOT and TF holders we have designed and used. In all of them the tip (gray long cylinder in (a)–(c) and (f), black in (d) and (e)) is held by its readout electrodes and the TF is mounted on a slider that allows bringing the two together with high precision. The hour-glass shape of the electrode in (e) and (f) is a "dove-tail" fitting that allows simple and stable mounting of the holder in the microscope and deposition chamber while also allowing efficient heat exchange so the tip can be cooled or heated while being deposited on.*

lower than the desired thin film thickness. As a result our design had to be modified and remodified and now the holders allow the TF support and alignment, simple mounting in the microscope or deposition chamber and coupling to a cooling (or a heating) block. Some of the various versions of our tip holders are seen in Fig. 2.6.

2.2.4 Scanning Results

In order to experiment with the TF topography sensors we have modified an NSOM [90,91] so we could use our tips rather than optical fibers, and carried out ambient conditions experiments with it. With this first prototype we could acquire topographic images with a typical sensitivity of about 1 Å. An example of such an image is seen in Fig. 2.7a showing the topography of an optical phase grating we used as a calibration sample. The grating has a period of 5 μm with a modulation amplitude of 80 nm and its wide regular features make it ideal for this use.

Once we saw that the concept we have chosen for the microscope is feasible, we have turned to designing the aluminum-SOT microscope. Due to the low T_c of the Al SOTs this microscope is designed to fit into a ^{3}He cryostat — a commercial top loading Oxford

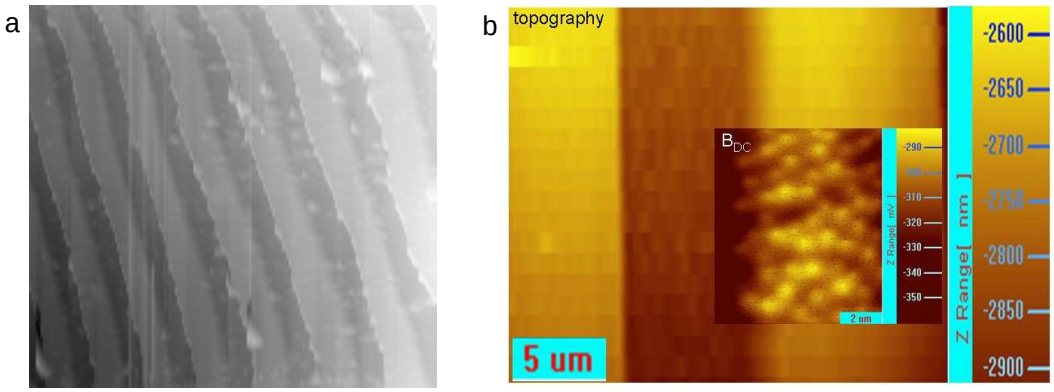

Figure 2.7: *(a) A topography image of an optical phase grating used as a calibration sample obtained by scanning an NSOM which was modified to have an SOT rather than an optical fiber coupled to its tuning fork [90, 91]. The grating period is* 5 μm *and the height modulation is* 80 *nm. (b) An image of the topography of our Nb meander shaped sample as and magnetic image (inset) as measured at 300 mK with our Al-SOT microscope. The magnetic image resolves single vortices.*

Heliox TL which we modified for this matter. For the fine and coarse sample-sensor motion we chose Attocube's ANSxyz100 scanner and ANPxy50 and ANPz101 coarse steppers (as is illustrated in Fig. 2.1). The control electronics, the main SPM controller, SPM-1000, and the PLL tuning fork controller, PLLPro, are both made by RHK. The SOT is read with a series-SQUID-array-amplifier, as described in 1.3.2, which has home built, battery operated, electronics [86].

With the aluminum SOTs working, and the correct recipe of how to couple an SOT to a tuning fork found, we could design and build the microscope and indeed in June 2010 we got our first combined topography and magnetic images. Fig. 2.7b shows an example of a topography scan of a meander shaped Nb thin film and overlayed on it is a magnetic scan image of one of the meander stripes showing vortices in the sample. Using a tuning fork has an added advantage— the SOT position is oscillating in a controlled manner at the tuning fork frequency. This adds an AC type measurement, which typically has a much better signal to noise ratio compared to the DC type magnetic signal.

2.3 Pb Based SOTs

There is one significant drawback to the SOTs described so far— that is the relatively low superconducting critical temperature of the aluminum film— approximately 1.2 K. Apart from the added experimental complexity, which the use of ^{3}He cryogenics introduces, the specimen temperature in such a setup has a very limited range and the maximal temperature might be too low for an effective study of vortex dynamics. For this reason

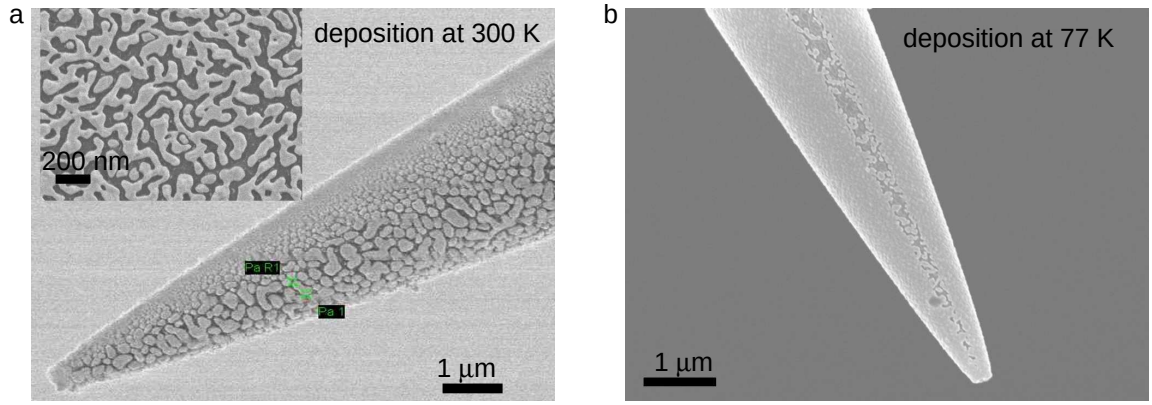

Figure 2.8: *A comparison of the quality of lead films deposited on quartz tip substrates at room temperature and at 77 K((a) and (b) respectively). The inset of (a) shows the a close up on a lead film deposited on a planar quartz substrate at 300 K.*

we made an effort to develop SOTs based on superconducting films of higher critical temperatures. Specifically we have tried lead, tin and niobium (with bulk T_c's of 7.2 K , 3.7 K and 9.2 K respectively). The study of lead based tips which was fruitful is described below. Compared with the Al tips, the lead tips we have made are not just characterized by a higher T_c but also about an order of magnitude higher sensitivity to magnetic flux.

The deposition of thin Pb films requires quite more than copying the Al SOT making recipe and replacing the aluminum with lead. The first difficulty we have met is due to the fact that thin Pb films tend to cluster making the film uneven with a percolation threshold of about 500–600 Å, more than twice the thickness of the superconducting film needed to make an SOT. In the literature we have found that either increasing the deposition rate or depositing a precursor layer of Ge will lower the Pb film percolation threshold but these methods only reduced the threshold to about 300 Å. We have finally overcome this obstacle by cooling the substrate with liquid nitrogen while depositing the lead.

Once we have efficiently cooled the substrate, decreasing the lead mobility on it, we could deposit continuous, 150 nm thick films, and have made a Pb-SOT. Then, however, we ran into a second significant difficulty— our lead nano-devices are prone to be burned due to static charges, much more than the Al tips. The vast majority of our tips burned until we have designed a tip holder that allows cooling the tip and measuring it. The fact that the holder can be mounted from the deposition chamber directly on the measurement rod minimized the tip handling and allowed shunting it at all times so the likelihood of static discharge is minimized.

The Pb SOTs characteristic V-I plots and their field dependence are similar to that of the Al SOTs (see Fig. 2.9). There is however, one significant difference between the

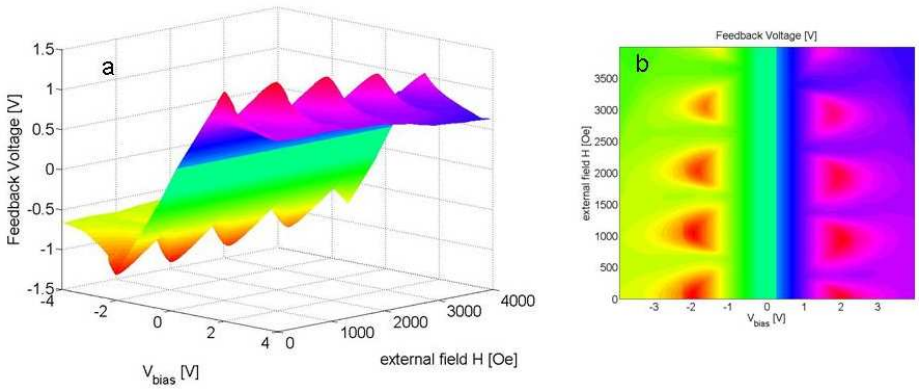

Figure 2.9: *Two views of the Pb SOT current as a function bias voltage and magnetic field. The interference pattern is similar to that of the Al SOT but the current is more than an order of magnitude larger. The z axis and color scale show the SSAA feedback voltage, which is proportional to the SOT current.*

two tip characteristics — the maximal critical current of the Pb SOTs is much higher due to its larger band gap (which manifests itself also in the higher T_c). While the critical currents of the Al SOTs are usually in the range of 1–15 μA the Pb SQUID critical current can be as high as 500 μA. As a result the signal from the Pb SOTs is much larger and the sensitivity of the Pb SOTs reaches 15 mV/G— more than an order of magnitude better! By reducing the electronics noise in the lead characterizing setup compared with the Al microscope setup by a factor of 2–3 we reached a spin sensitivity of 2 $\mu_B/\sqrt{\text{Hz}}$.

3. Magneto-optics Projects — Methods

3.1 Magneto-optics in Brief

Imaging single vortices with magneto-optics can be done only where the vortices do not overlap. Typically, this means that vortices can be resolved only at low fields and even then the task is challenging and requires customized microscopes (where the objective is cooled) [75, 92]. However, the Josephson vortex lattice due to in-plane magnetic fields in layered superconductors, is widely spaced even at relatively high in-plane fields and so the JVs can be imaged by conventional magneto-optical microscopy. In order to study this vortex system we have used the differential magneto-optics (DMO) microscopy system—a robust, well established measurement technique [93] that has been in use in our lab for about a decade [94–99]. This microscopy technique is briefly described below (see e.g. [96,99,100] for more details) with an emphasis on newly developed calibration routines and the way to optimize JV imaging capabilities.

3.1.1 Working Principle

At the heart of the magneto-optics method is the magneto-optical indicator (MOI) which rotates the polarization angle of linearly polarized light passing through it by an amount proportional to the local magnetic induction. Thus by placing a superconducting sample in a very close proximity to the MOI, in a microscope between two nearly crossed linear polarizers, we obtain an image whose intensity is a measure of the local magnetic induction in the sample.

The effect, which is called Faraday rotation, is weakly seen in many isotropic dialectic materials, such as water and glass. These materials become optically active due to the magnetic field and have different refractive index for right-handed and left-handed-circularly-polarized light. As a result, the polarization angle of linearly-polarized light, which is described as a combination of the two circular polarizations, rotates as it passes through the medium [101].

For small enough rotation angles, as in our case, the rotation angle is linear in the

magneto-optical medium thickness and the magnetic field and is usually parameterized as follows $\Theta_f(x,y) = 2dvB(x,y)$, where d is the indicator thickness, $B(x,y)$ is the local magnetic induction and v is called the Verdet constant. The Verdet constant is obviously material dependent but also depends on the temperature and the wavelength of the incident light. The intensity of light that passes through a linear polarizer, an MOI and then a second polarizer at an angle of $\pi/2 + \theta_0$ relative to the first is given by $I = \tilde{I}\sin^2(2dvB + \theta_0)$, with $\tilde{I}$ being the light intensity when the polarizers are parallel and the field is zero. Typically the Faraday rotation angle is about 2° for an applied field of 100 Oe, and θ_0 is also of order of a few degrees. Hence, to a very good approximation the magneto-optical image can be approximated as quadratic in B and re-parameterized as follows [102],

$$I = I_0 + L\left(B - B_0\right)^2. \tag{3.1}$$

Typically, due to uneven lighting, dirt and defects in the MOI each of the parameters in (3.1) is position dependent, so in order to measure $B(x,y)$ from an image the indicator should be pixelwise calibrated as described in more detail in Sec. 3.2. A typical MO image and calibration curve can be seen in Fig. 3.1a and Fig. 3.1d respectively.

Even once the image is calibrated the signal to noise ration (SNR) in MO images is pretty poor. Thus, in order to improve the SNR we use the *differential* MO technique in which pairs of images are taken, denoted by I_+ and I_-, both at the same external parameters except for one modulated parameter, which is slightly different in the two. Usually, we modulate the external magnetic field, temperature or the applied current. For the sake of the example, consider modulating the applied magnetic field so that images I_+ and I_- are taken at $H_\pm = H_0 \pm \delta H$. If the modulating signal is small then one can write $B(x,y;H_+) - B(x,y;H_-) = 2\Delta B(x,y)$, with $, \Delta B \ll B(H_0), B_0$. The image difference is

$$\Delta I \equiv I_+ - I_- = 4L\left[B(H_0) - B_0\right]\Delta B. \tag{3.2}$$

In case of a modulating magnetic field of amplitude $\Delta H = H_+ - H_-$, Eq. (3.2) can be written as

$$\Delta I = 4L\left[B(H_0) - B_0\right]\frac{dB}{dH}\Delta H. \tag{3.3}$$

The differential technique improves the SNR by about two orders of magnitude and has a sensitivity of about 30 mG [95].

3.1.2 Experimental Setup

The MOIs we use are Bi-doped yttrium-indium-garnet films with a typical thickness of about 5 μm, which are grown on gallium gadolinium garnets and coated with a thin mirror (1000 Å of aluminum) that were grown by V. Skidanov in Chernogolovka. These MOIs have a very large Verdet constant which is also approximately constant at the relevant temperature range (10–100 K). The Verdet constant is maximal for incident light of wavelength of about 500 nm. Thus, for illumination we use mercury lamps that have a strong spectral line at 546 nm (the rest of the spectrum is filtered).

The microscope that we use is a commercial Leica DMR microscope that is designed for polarized microcopy. The camera mounted on the microscope is a charged couple device (CCD) camera, either a Quantix Q57 or a Lumenera Infinity5, that are designed for acquiring dark images with high quantum efficiency (i.e. high detection probability for a single photon). The sample and MOI are placed in a custom built ^{4}He flow cryostat that allows stabilized temperature control in the range of 10–300 K. The magnet is also home built. It is water cooled, with three Helmholtz-coil pairs and can produce fields up to about 400 Oe in any spatial direction (the actual value depends on the power supply).

Typically, the optimal MO images are acquired when the two polarizers are almost crossed — $\theta_0 \approx 3^\circ$. Hence, the resulting images are relatively dark and long exposure times are needed in order to acquire decent images, typically about 5 seconds per image. A DMO image, which is the difference of two such images, is typically averaged n =5–10 times so one DMO image takes 5 sec $\times\, 2 \times n \gtrsim 1.5$ minutes to acquire.

3.1.3 MOI-Sample Mounting

The proximity of the MOI to the sample surface is a crucial limiting factor for the actual measurement sensitivity. If the MOI and sample are more than a couple of microns apart then magnetic signals from the sample will spread before they reach the MOI resulting in weaker measurable signals and blurred, defocused, magnetic images. Since the MOI indicators we use have significant edge artifacts they are usually cut so that they are about three times wider and longer than a typical sample. When they are mounted on the sample they tend to rest slanted on one of the sample edges and the substrate, causing a large sample-MOI displacement.

We have managed to overcome this problem by using the following procedure. We first align the sample substrate under a Zygo interferometer microscope, which is equipped with a fine 2 axes tilt stage and a Michelson-Morley interferometer-lens so that the sample plane is normal to the optical axis and the interference fringes are the widest. The MOI

is then mounted on the sample, which has four vacuum grease gluing pillars surrounding it so that its center of gravity is roughly above the sample's center. Finally, we correct the MOI angle using the interferometer lens so that it is parallel to the sample surface.

3.2 Calibration and Drift Correction Algorithm

In order to make quantitative measurements one has to calibrate the MOI response, polarizer angle and light intensity, i.e., find the three parameters L, B_0 and I_0 of Eq. (3.2). The way the MOIs are usually calibrated is by assuming the illumination and MOI response are constant in space. In this case one could use a region of the field of view that is outside (and far from) the sample to calibrate it. This can then be done at any temperature and the temperature dependence of the MOI can be accounted for. This is impossible using our mercury lamps because these have uneven illumination, which also fluctuates with a time scale of a few days. Hence, L, B_0 and I_0 depend on the spatial position and require re-calibrating every day or two. In order to calibrate the MOI response in the entire field of view B must be equal to H in the entire field of view, so the pixelwise calibration can be done only at $T > T_c$.

Fortunately, the MOI temperature dependence is weak. However, when changing the temperature the sample drifts causing misalignment of the image and calibration matrices. This means the image should be shifted before being inverted,

$$B(x,y) = \sqrt{\left| \frac{I(x+dx, y+dy) - I_0(x,y)}{L(x,y)} \right|} + B_0(x,y). \tag{3.4}$$

In order to find the optimal shift, (dx, dy), we iteratively look for the shift that minimizes the variance of $B(x,y)$ in a region of interest that has a pronounced defect [103]. This is demonstrated in Fig. 3.1, which shows a raw MO intensity image (a), a calibrated image with no drift correction (b) and a calibrated and drift corrected image (c). Fig. 3.1d shows, as an example, the response of a random pixel to the applied field at $T = 87K > T_c$. In the raw intensity image we note that the sample has on average lower intensity than the background but otherwise it is hard to distinguish for example, if the sample center has high intensity because of uneven light intensity or high magnetic induction. The short bright lines on the sample sides are interference fringes due to the fact that the mirror on the back of the MOI is thin and has non-zero transmission. In Fig. 3.1b the light seems even but the image is corrupted by the effect of the drift, which amplifies defects. The calibrated and drift corrected image clearly shows the sample induction profile—high and even at the sample bulk, very high outside the edges and approaching zero just

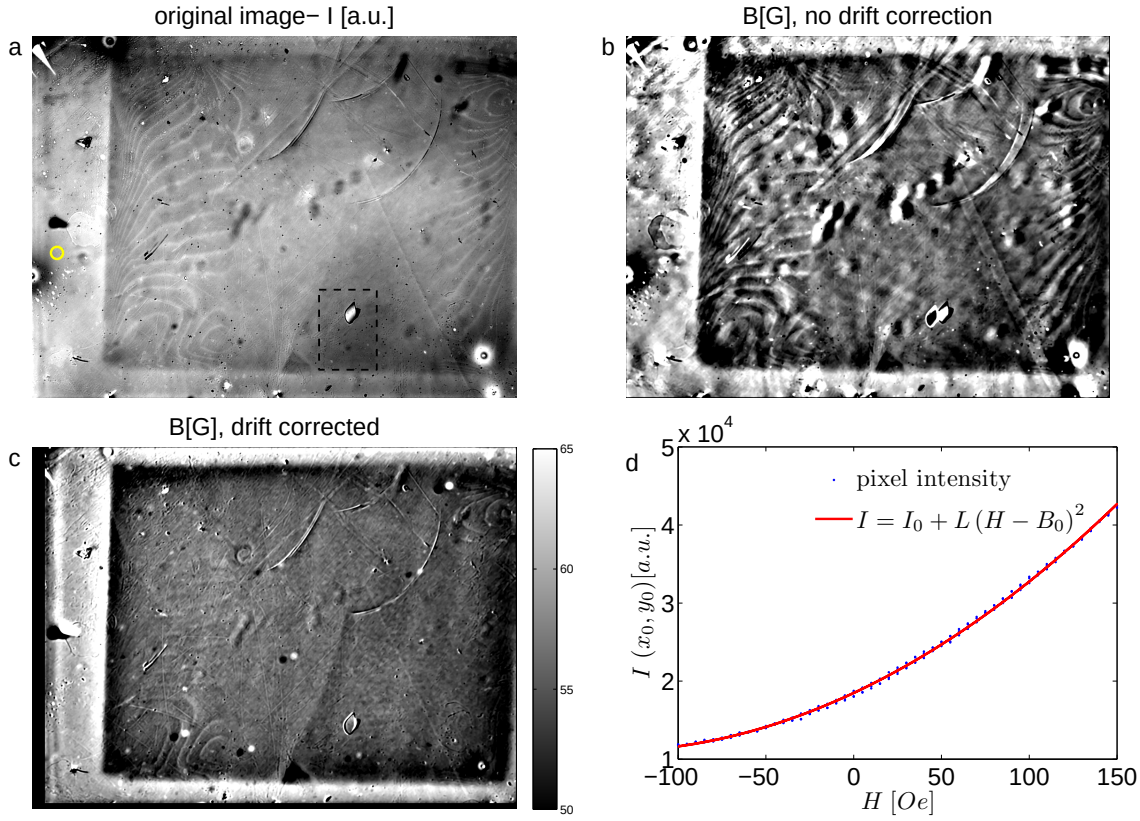

Figure 3.1: *(a) An example of an untreated MO image of an underdoped BSCCO sample at $T = 42$ K, and $H_z = 59$ Oe. The overlayed rectangle is the region of interest used for drift correction and the pixel at the center of the yellow circle is the one whose response is shown in sub-figure d. The short bright lines on the sample sides are interference fringes caused by the fact that the mirror on the back of the MOI has non-zero transmission. (b) The induction image corresponding to the intensity image in sub-figure a without drift correction. The image has the same gray level as sub-figure c. (c) The induction image with the drift corrected. The black and white circles are due to defects that are not on the sample plane and so have a different drift than the sample. (d) The response of the pixel circled in sub-figure a to the applied field at $T = 87$ K $> T_c$. This type of calibration is done for every pixel in the image.*

inside the edges. Also seen are vertical arc-like defects of higher induction— these are crystal growth defects. After the pixelwise calibration is made one can account for the temperature dependence of the MOI (or any other *global* change in light intensity) by rescaling the induction signal so that far outside the sample $B = B_{\text{applied}}$. Using Eq. (3.4) one has

$$B(x,y) \to \frac{B_{\text{applied}} - \langle B_0 \rangle_{\text{ROI}}}{\langle B \rangle_{\text{ROI}} - \langle B_0 \rangle_{\text{ROI}}} \left(B(x,y) - B_0\right) + B_0, \tag{3.5}$$

where $\langle \ldots \rangle_{\text{ROI}}$ means spatial average over a region of interest outside the sample.

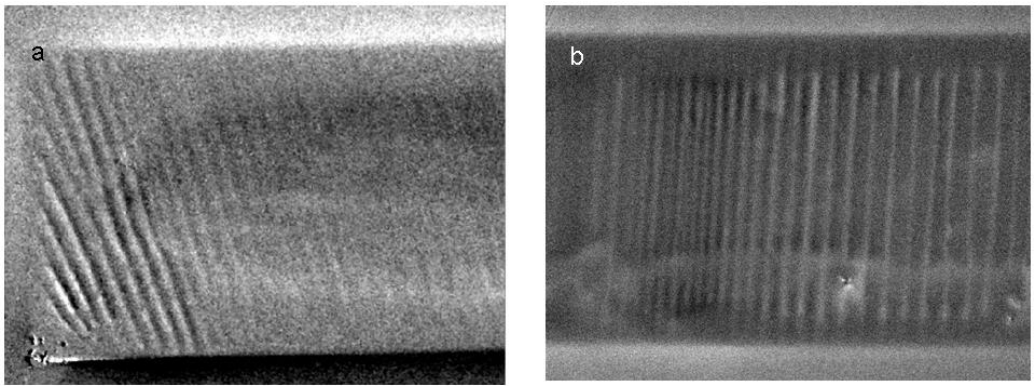

Figure 3.2: *JVs in a current modulated (a) and a field modulated (b) DMO image. The JVs in (a) are almost vertical lines (top left to bottom right), which have a bright/dark contrast on the current pads where the modulating current has an out-of-plane component (left part of the image). Where the JVs modulate the edge geometrical barrier they appear as long modulations to the contrast at the edge (right side of (a)). In (b), the JVs appear as vertical bright lines, which are characteristic of a field modulated image of a SC in the chain state.*

3.3 The Study of JVs with Magneto-optics

As was described in Sec. 1.2 Josephson vortices attract pancake vortices. As a result they can be indirectly imaged by (for example) MO microscopy, which, in general, is sensitive to perpendicular magnetic field. The JVs that are imaged indirectly, are referred to as pancake-decorated-Josephson vortices. Obviously, adequate field and spatial sensitivity are needed. In the DMO technique the PV decorated JVs can show up in different ways depending on the modulation scheme and the external parameters. In the simplest case the difference of two images, I_+ at $H_z = H_0 + dH$ and I_- at $H_z = H_0 - dH$ is taken. If the sample is in the chain state and most PVs are found on the JVs, then the magnetic induction, B, will be higher on the JVs in the I_+ image than in I_-, whereas in the inter-JV areas there will hardly be any change. In this case the JVs will appear bright in the differential image (see Fig. 3.2b). In contrast, if the JV positions are different in the two images and the PV density on them is larger than between them then the JV will show up as lines having dark/bright contrast (see left part of Fig. 3.2a). This can be achieved by current modulation, if the current has some out-of-plane, z, component, so that the Lorentz force it exerts on the JVs has an in-plane component (that is also normal to the JVs). This is achieved in our setup since the current contact pads are at the top of the sample and the transport current from pad to pad has some z component near the pads.

The sample edge barriers also allow imaging the JVs. In this case the edge barriers

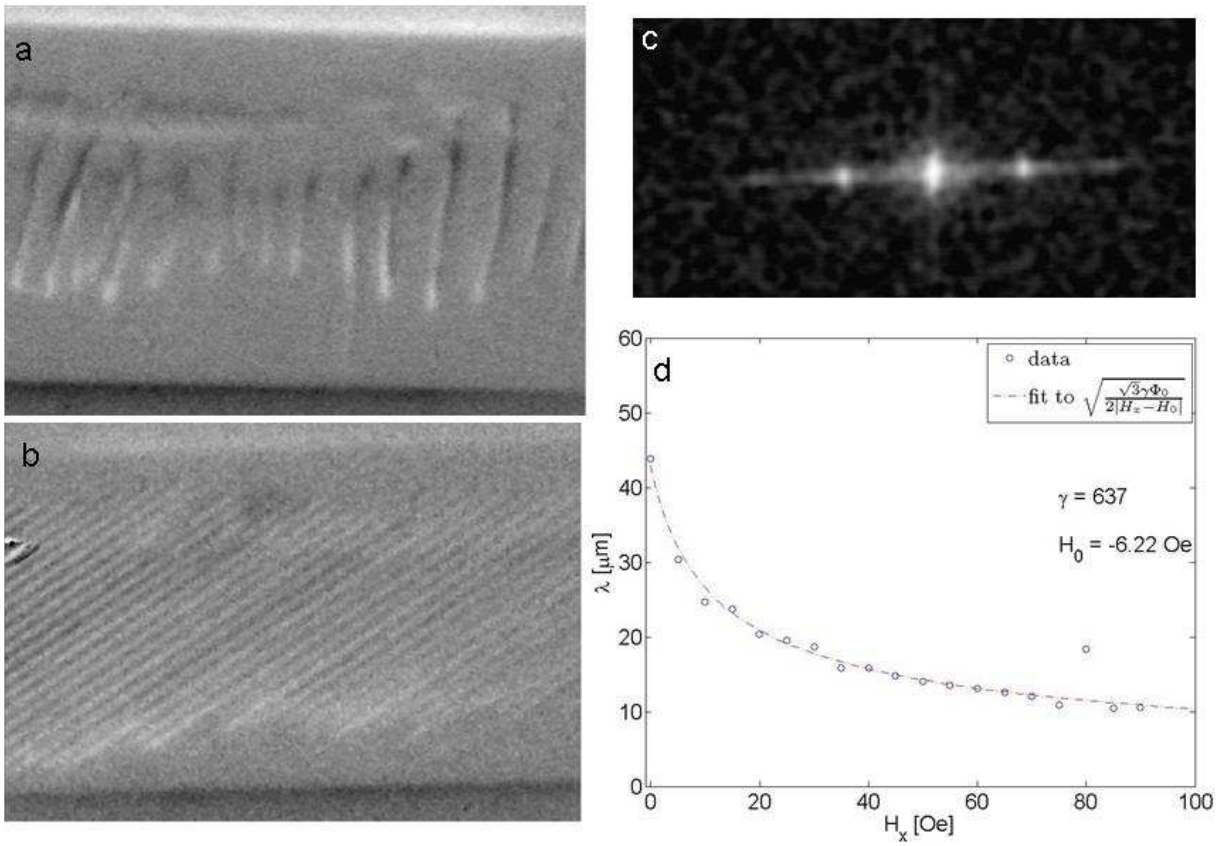

Figure 3.3: *(a) and (b) Current modulated DMO images of JVs with* $H_{\mathrm{in-plane}} = 10$ Oe, $0°$ *and* $H_{\mathrm{in-plane}} = 30$ Oe, $45°$ *respectively (*$0°$ *is arbitrarily chosen to point along the sample width— the image vertical direction). Image (a) is taken at* $H_z = 1.5$ *Oe and* $T = 82$ *K, and image (b) at* $H_z = 1.5$ *Oe, and* $T = 84$ *K. The modulation current is* $2dI = 20$ *mA and* $2dI = 8$ *mA, respectively. (c) 2D Fourier transform of a typical JV DMO image, which is taken at* $T = 74$ *K and* $H_z = 2$ *oe. (d) The JV stack mean distance as a function of the in-plane field (circles) magnitude showing the typical* $1/\sqrt{|B_x|}$ *dependence. The dashed line is a fit to* $\sqrt{\sqrt{3}\Phi_0/2|H_x - H_0|}$. *All the images and data relate to the overdoped BSCCO sample (*$\mathrm{T_c}$ *=87 K) which is described as Sample A in Sec. 4.1.*

cause a non-trivial B profile in the sample, which is wider where there are JVs that reduce the barrier as we discuss in detail in the Sec. 4.1. A differential image sensitive to the B profile boundary, whatever the modulating signal is, may show the boundary wider where there are JVs, but the JV contrast will look the same as in the rest of sample (right side of Fig. 3.2a).

In order to verify that what we are imaging are JVs we have taken a series of images at different in-plane field angles and magnitudes and fit the period which we retrieved from

the two dimensional Fourier transform of the images to the theoretical dependence [51],

$$a_{JV} = \sqrt{\frac{\sqrt{3}\gamma\Phi_0}{2B_x}}. \tag{3.6}$$

Typical images from such series as well as the Fourier spectrum and a fit to Eq. (3.6) are shown in Fig. 3.3. The images taken at low in-plane fields show that sample inhomogeneities can result in an irregular JV spacing and sometimes also bent JVs (see e.g. Fig. 3.3a). The interactions of sample inhomogeneities with the JVs are mediated by PVs and in general they tend to significantly broaden the Fourier peaks and thus broaden the error bar on the fit to Eq. (3.6). The JVs are pinned to sample defects because the PVs which bind to them are pinned and inhomogeneities that have currents flowing around them apply a Lorentz force on the PVs and thus also on the JVs.

In order to achieve good contrast to JVs obviously one has to ensure that the sample-MOI distance is minimal. The modulation scheme and the magnitude of the modulating field also have to be tuned in order to achieve optimal JV images. This however, is not enough since it turns out that following (out-of-plane) field ramps there is a typical relaxation time during which the JV position drifts. The typical relaxation times we observed were as high as a few minutes during which the JV stack position could travel a few tens of microns as shown in Fig. 3.4. Since a typical exposure time in DMO measurements is of the same order of magnitude, the JV signal can be washed out completely unless the image is grabbed after a proper wait time.

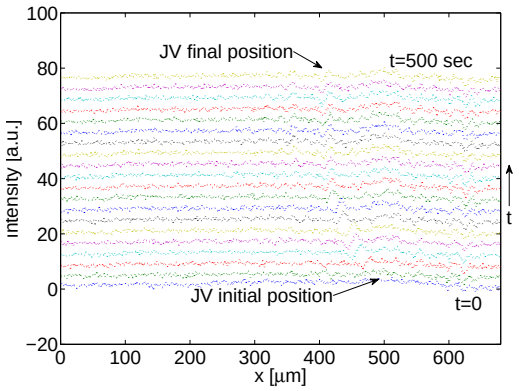

Figure 3.4: *Line cross-sections of DMO images at different times from $t = 0$ to $t =$ 500 sec. The JV position in the line-cut appear as peak/valley pattern modulating the average DC value. It is clear that for a time of about 300 seconds, following a step in H_z, there is a significant drift in the JV position.*

A nice example of the quality of our images can be seen in Fig. 3.5a. In the figure our sample is imaged at zero in-plane field, and H_z— a little above the penetration field, which is the field where vortices first penetrate the bulk of a zero-field-cooled superconductor. In this case, vortices are expected to enter the sample from the edges, bending considerably [104], as seen in Fig. 3.5b. However, since our specimen is anisotropic, the

vortices buckle, and form segments of JVs extending from the edge to the sample center as is seen in Fig. 3.5a. These JVs, that from a top view look radial, are seen better in the image where there is a z component to the modulating current, as discussed above, but they can be traced all along the sample.

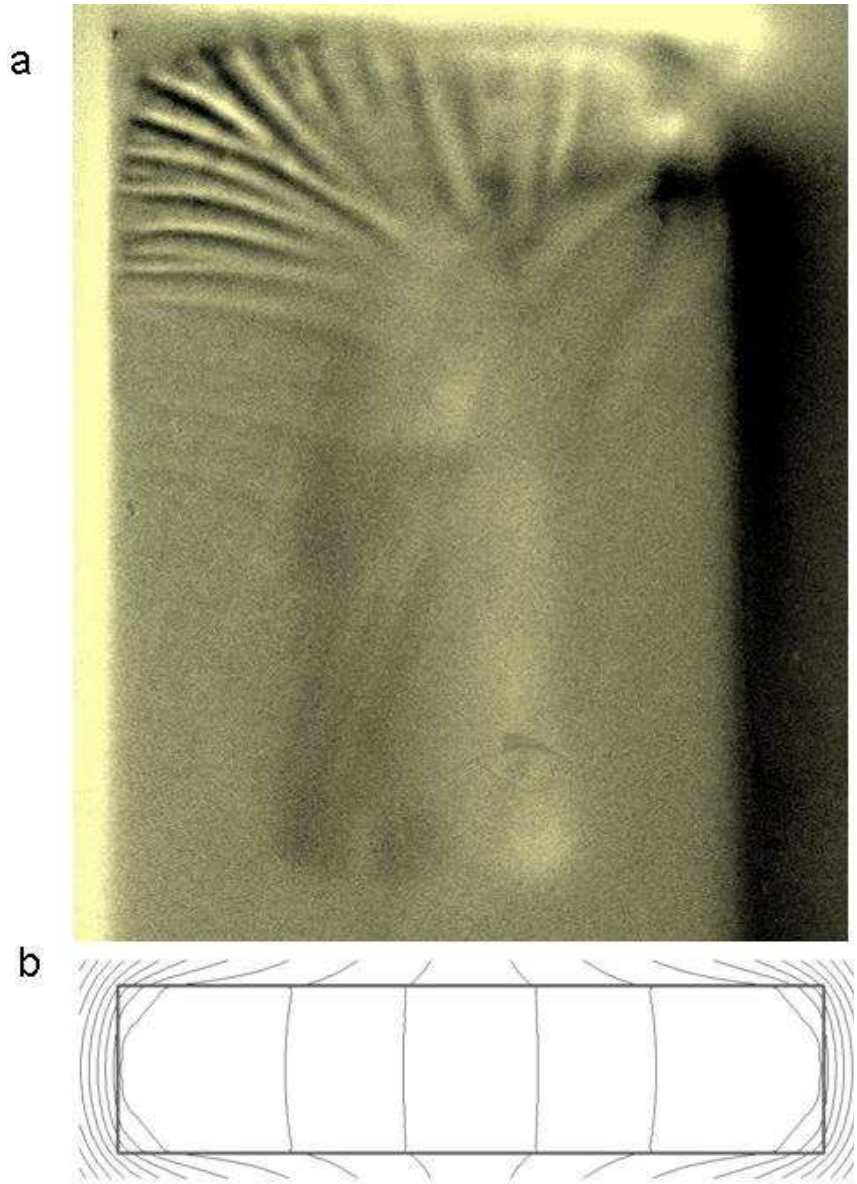

Figure 3.5: *(a) Current modulated image of BSCCO with H_z a little above the penetration field and no in-plane field. The fanning at the edges are presumed to be the edge vortices that bend in order to enter but buckle due to the anisotropic nature of the crystal. (b) A simulation, by E. H. Brandt. [104], of the magnetic field at the cross-section of a long, isotropic, superconductor showing vortices penetrating from the edges.*

4. Magneto-optics Projects — Results

We have used DMO in three different projects. In the first two, we studied the local effects of the JV lattice on the PV lattice properties, in the range where the former can be directly imaged as described above. In both cases the bulk effect of the in-plane (IP) field was known, namely that an IP field reduces the geometrical barrier (GB) hysteresis and reduces the melting temperature. Using our ability to image the JV stacks, however, we could show that the reduction of the GB and melting is local. We have actually simulated the effect of a single JV stack, with regard to the GB hysteresis, by making an artificial narrow and shallow groove, and showed that it has a similar effect as the JV stacks.

In the third DMO project we have used the two-dimensional induction images in order to correlate phase transitions in BSCCO with a contrast pattern that is unique to them and results from the fact that the transitions are affected by different defects and have different length scales. These data can be used to characterize the phases, distinguish the phase transitions when two occur simultaneously, and find a transition when the contrast is poor according to its characteristic dynamics.

4.1 Suppression of Geometrical Barrier in $Bi_2Sr_2CaCu_2O_{8+\delta}$ Crystals by Josephson Vortex Stacks

The paper attached below was submitted to Physical Review B. The measurements that it describes and their analysis were done by the author of this work.

4.1 Suppression of Geometrical Barrier in $Bi_2Sr_2CaCu_2O_{8+\delta}$ Crystals by Josephson Vortex Stacks

Suppression of geometrical barrier in $Bi_2Sr_2CaCu_2O_{8+\delta}$ crystals by Josephson vortex stacks

Y. Segev,[1,*] I. Gutman,[1] S. Goldberg,[2] Y. Myasoedov,[1] E. Zeldov,[1]
E. H. Brandt,[3] G. P. Mikitik,[4,3] T. Katagiri,[5] and T. Sasagawa[5]

[1] *Department of Condensed Matter Physics, Weizmann Institute of Science, Rehovot 76100, Israel*
[2] *Physics Department, Duke University, Durham, NC 27708, USA*
[3] *Max-Planck-Institut für Metallforschung, D-70506 Stuttgart, Germany*
[4] *B. Verkin Institute for Low Temperature Physics & Engineering, National Ukrainian Academy of Sciences, Kharkov 61103, Ukraine*
[5] *Materials and Structures Laboratory, Tokyo Institute of Technology, Kanagawa 226-8503, Japan*

Differential magneto-optics are used to study the effect of dc in-plane magnetic field on hysteretic behavior due to geometrical barriers in $Bi_2Sr_2CaCu_2O_{8+\delta}$ crystals. In absence of in-plane field a vortex dome is visualized in the sample center surrounded by barrier-dominated flux-free regions. With in-plane field, stacks of Josephson vortices form vortex chains which are surprisingly found to protrude out of the dome into the vortex-free regions. The chains are imaged to extend up to the sample edges, thus providing easy channels for vortex entry and for drain of the dome through geometrical barrier, suppressing the magnetic hysteresis. Reduction of the vortex energy due to crossing with Josephson vortices is evaluated to be about two orders of magnitude too small to account for the formation of the protruding chains. We present a model and numerical calculations that qualitatively describe the observed phenomena by taking into account the demagnetization effects in which flux expulsion from the pristine regions results in vortex focusing and in the chain protrusion. Comparative measurements on a sample with narrow etched grooves provide further support to the proposed model.

PACS numbers: 74.25.Ha, 74.25.Op, 74.25.Uv, 74.25.Wx

I. INTRODUCTION

One of the most prominent characteristics of type II superconductors is the large magnetic hysteresis that arises from the existence of potential barriers that impede vortex motion[1]. There are several sources of potential barriers: pinning due to quenched material disorder in the bulk of the sample, surface pinning produced by the roughness of the sample surface[2], Bean-Livingston surface barrier arising from the force between a vortex parallel to a surface and its image[3], and geometrical barrier (GB) that arises from the force due to Meissner currents in thin slab-shaped superconducting samples in perpendicular field[4–10].

Strong vortex pinning and the associated magnetic hysteresis are vital elements in superconductor applications that are based on high critical currents. The magnetic hysteresis, however, masks the equilibrium magnetization properties, the study of which is essential for comprehension of the thermodynamic structure of the vortex matter. In order to overcome this limitation, vortex shaking has been employed in recent years, which was shown to suppress the magnetic hysteresis very effectively at not too low temperatures[11–13]. In this method an ac in-plane field H_x is applied in addition to the main dc H_z which causes local shaking and equilibration of the vortices. dc in-plane fields were also shown to reduce the magnetic hysteresis[14–18].

Vortex shaking was found to suppress the hysteresis that arises either from bulk pinning that is usually the dominant source of hysteresis at lower temperatures, surface barriers that often dominate vortex dynamics at elevated temperatures and fields[19–23], and GB's that commonly govern the hysteresis at high temperatures and low fields[4,5,19,23,24]. Detailed theoretical studies explained the suppression of bulk pinning hysteresis by vortex shaking in terms of the Bean model in a turning magnetic field[25–27]. This description may similarly apply to the case of surface pinning. Also the suppression of the Bean-Livingston surface barrier hysteresis could possibly be understood in terms of easier vortex loop nucleation at the sample corners for tilted vortices[28]. In the above mechanisms the potential barriers are microscopic and hence local ac displacement or tilting of a vortex segment in presence of an average dc driving force can enhance vortex activation and relaxation. In contrast, the GB in a platelet sample gives rise to a vortex dome in the center of the sample surrounded by a vortex-free region[4–8]. This vortex-free region constitutes a large barrier that has a macroscopic energy scale of the order of the vortex line tension times the sample thickness and a macroscopic length scale of the order of sample's width. As a result, this barrier cannot be overcome by any local vortex perturbation or tilting. Hence the experimental observation that the vortex shaking by in-plane field suppresses the hysteresis due to GB was highly surprising and has remained unresolved so far.

In this paper we describe a possible resolution of this question in the case of layered superconductors by investigating the GB behavior in the presence of a dc in-plane field. In highly anisotropic layered materials like $Bi_2Sr_2CaCu_2O_{8+\delta}$ (BSCCO) the in-plane field H_x re-

sults in the formation of stacks of Josephson vortices (JV's)[29–31]. Addition of H_z causes formation of crossing lattices in which stacks of pancake vortices (PV's) form chains along the Josephson vortices[31–37]. Surprisingly, we find that these chains exist also outside the vortex dome, protruding like vortex whiskers into regions that are vortex free in absence of H_x. As a result, easy channels are apparently formed that allow vortex penetration through the macroscopic GB suppressing the hysteresis. This observation appears to be inconsistent with theoretical expectations since the reduction in the energy of the pancake stack by the Josephson vortices should be much smaller than the height of the geometrical barrier[4,31]. Therefore, the regions outside the vortex dome should have remained vortex free even in the presence of H_x and no significant suppression of the barrier should occur. We propose an explanation to this phenomenon in terms of interaction between JV's and PV's that is enhanced by the demagnetization effects in platelet geometry. We demonstrate this scenario by studying vortex behavior in a sample with a shallow and narrow groove etched into its surface using a focused ion beam (FIB).

II. GEOMETRICAL BARRIER

The GB is a macroscopic potential barrier that vortices have to overcome in order to enter or leave the sample and is the main source of magnetic hysteresis in thin slab-shaped samples with weak pinning. The barrier is formed by the interplay between the vortex line tension and the Lorentz force that is induced by the circulating Meissner currents[4–10]. In a sample with elliptical cross section, for example, the energy of a test vortex has two contributions: the positive vortex line energy increases gradually from zero at the edge of the sample to a value of $\epsilon_0 d$ in the center (ϵ_0 is the vortex line energy per unit length and d is the sample thickness). The Meissner currents that flow over the entire surface exert inward forces on the vortex that gradually lower its energy as it moves towards the center. In a sample with elliptical cross section the two contributions cancel out rendering a constant vortex energy and a corresponding position independent and reversible induction $B(x,H)$. In a platelet sample of rectangular cross section, in contrast, by cutting through the sharp rims, the vortex attains its full line energy $\epsilon_0 d$ within a distance of the order of $d/2$ from the edge[4], while the Meissner currents remain distributed as in elliptical sample[38]. As a result, a geometry related barrier of height of the order of $\epsilon_0 d$ is formed that extends over a width of the order of the half width of the sample, w [4–10,24]. Consequently, when the field H_z is increased above the penetration field $H_p \approx H_{c1}\sqrt{d/w}$ vortices entering through the edges are swept by the Meissner currents towards the center where they accumulate giving rise to a dome shaped induction profile of width $2b$, see Fig. 1(c). The vortex-filled dome is current free while the surrounding vortex-free region carries the Meissner currents. The induction profile, with a central dome surrounded by an area of zero B is very distinctive and is the hallmark of the GB model. The vortices in the dome cannot leave the sample since they are trapped by the barriers due to the Meissner currents in the surrounding flux-free regions. Thus, when the field is decreased the dome expands, while keeping the total flux in it constant, giving rise to hysteretic magnetization. Only when the dome reaches the edges the barriers vanish allowing vortices to leave the sample.

III. EXPERIMENTAL DETAILS

Several over-doped and optimally-doped BSCCO samples were studied. We present here data of two over-doped samples, with a critical temperature of $T_c = 87$K, cleaved from one thick crystal, sample A and sample B, with platelet shapes of length $2L = 1500\mu m$, width $2w = 420\mu m$ and thicknesses d of $8\mu m$ and $20\mu m$ respectively. Similar results were obtained from optimally doped crystals[18]. The differential magneto-optical (DMO) technique[39] was used to study the induction profiles and the magnetization behavior of the samples. By minimizing the magneto-optical indicator — sample distance and utilizing differential imaging we achieved high visibility of the vortex chains and studied their effect on hysteretic magnetization. The total exposure time of a differential image was typically 2 to 3 minutes. We found that following a field ramp the JV's often show slow relaxation for about two minutes, during which their position within the sample changed. Thus quality images of the chains could be achieved by waiting 2 to 3 minutes between the end of a field ramp and the beginning of image exposure. In order to simulate the effect of JV's, we also studied the magnetic behavior of crystal A after two fine grooves, 80 and 160 nm deep and 350 nm wide, were etched on the surface using an FEI Helios Focused Ion Beam system.

IV. RESULTS

In order to visualize the vortex dome structure with enhanced sensitivity, we carried out DMO with either field modulation or current modulation. In the former case, $B(x,y)$ images taken at $H_z = H_0 - dH$ are subtracted from images taken at $H_z = H_0 + dH$ and few tens of such differential images are averaged resulting in the differential image $\delta B(x,y)$[39]. When the field is modulated by $2dH$ the vortex dome expands and shrinks periodically, keeping the total flux in the dome constant, see Fig. 1(c). As a result, when the field is raised to $H_z = H_0 + dH$ the induction in the center of the dome is increased giving rise to a positive δB signal, while the induction near the dome edges is decreased resulting in a negative δB there[24,40], see Fig. 1(d). This effect is clearly visible in the DMO data in Figs. 1 (a) and (b), in which the edges

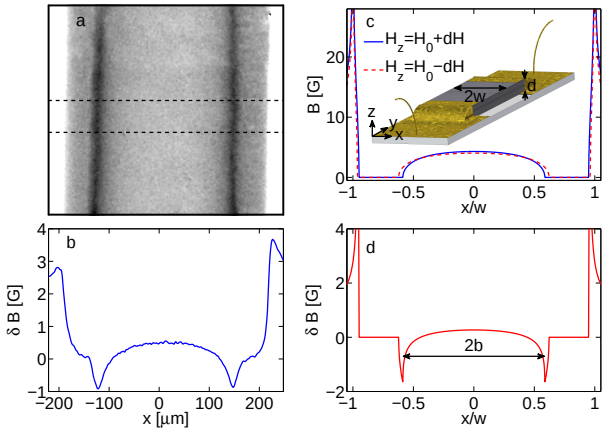

Figure 1. (color online) (a) Field modulated DMO image of sample B displaying the GB dome along the central part of the sample ($H_z = 6.7$ Oe, $dH = 0.4$ Oe, $H_x = 0$, and $T = 75$ K). The dark (white) vertical stripes indicate the dome (sample) edges. (b) The differential field profile $\delta B(x)$ across the width of the sample averaged over the strip marked by the dashed lines in (a). The two minima with negative δB indicate the dome edges, and the two maxima – the sample edges. (c) The theoretical field profiles of a thin and infinitely long sample $B(x, z = 0)$, at two values of $H_z = H_0 \pm dH$ ($H_0 = 6.7$ Oe, $dH = 0.4$ Oe, $H_{c1} = 33.1$ Oe, $d/w = 0.1$). Inset: The experimental schematics showing a BSCCO crystal with gold contacts glued onto a substrate. (d) The difference $\delta B(x)$ of the two $B(x)$ profiles plotted in (c) corresponding to the experimentally measured differential signal. The dome width $2b$ is marked.

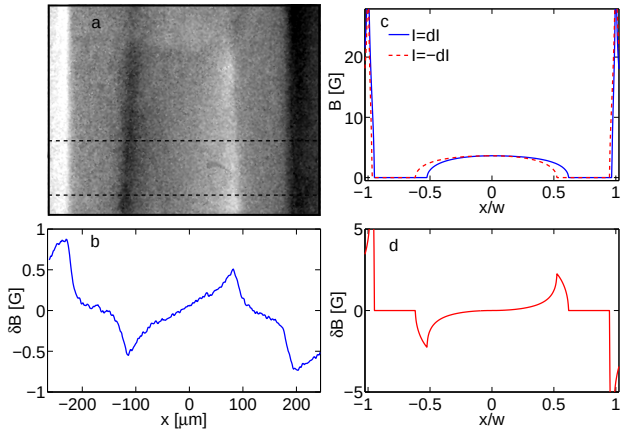

Figure 2. (color online) (a) DMO image with current modulation of sample B displaying the GB dome along the sample center at $H_z = 6.8$ Oe, $H_x = 0$, $T = 75$ K, and $dI = 10$ mA. The current modulation causes the right (left) edge of the dome to appear bright (dark) and the right (left) edge of the sample to appear dark (bright). (b) The differential field profile across the width of the sample averaged over the strip marked by the dashed lines in (a). (c) Theoretical field profiles across an infinitely long and thin sample in presence of positive and negative applied transport current showing the shift of the dome. (d) The difference of the two profiles in (c) corresponding to the experimentally measured differential signal.

of the dome appear as dark regions of negative values.

In DMO with current modulation, images taken in the presence of transport current $I = -dI$ are subtracted from images taken at $I = dI$ and averaged[41]. Since the Meissner currents flow in the opposite directions on the two sides of the dome, the applied transport current increases the total current flowing on one side of the dome and reduces the current on the other side. As a result, the dome is shifted away from the center as shown in Fig. 2(c). Therefore, in the current modulated DMO images one edge of the dome will appear as a bright strip with a positive signal and the other as a dark strip with a negative signal as shown theoretically in Fig. 2(d) and experimentally in Figs. 2 (a) and (b). Note also that the self-induced magnetic field of the transport current has an opposite sign at the two edges of the sample. As a result in DMO image with current modulation one edge of the sample is dark while the other is bright, Fig. 2(a), in contrast to DMO with field modulation in which both edges appear bright, Fig. 1(a).

We now analyze the behavior of the dome width, $2b$, along the magnetization loop. Figure 3(a) shows the calculated behavior of b using the GB formalism of[4,24,42]. Initially the sample is in the Meissner state ($b = 0$) which is retained until $H_z = H_p \simeq (2H_{c1}/\pi)\sqrt{d/w}$, above which flux starts entering the sample causing b to increase rapidly. As H_z is further increased, b asymptotically approaches its maximum value $b_{max} = w - d/2$, corresponding to the dome width at which the potential barrier vanishes. If the field is decreased from an intermediate value, b first expands to b_{max} while the total flux in the dome remains constant (open circles in Fig. 3(a)). When the field is further reduced, b remains at its maximal value allowing the vortices to exit through the edges. The corresponding calculated local magnetization loop is shown in Fig. 4(a).

It can be readily shown[4] that both the ascending and descending magnetization branches are energetically metastable. Compared to the equilibrium conditions, at which the vortices in the dome have the same energy as the vacuum $E = 0$, on increasing (decreasing) field the vortex energy is negative (positive), the dome is narrower (wider), there is a deficiency (excess) of vortices in the sample and the magnetization is lower (higher) than at equilibrium. The dashed lines in Figs. 3(a) and 4(a) show the corresponding equilibrium behavior of the dome width $b^0(H_z)$ and of the local magnetization.

Figure 3(b) shows the experimentally measured dome width along the magnetization loop in sample B. In absence of an in-plane field ($H_x = 0$) the behavior is qualitatively very similar to the theoretical GB curve shown in Fig. 3(a). On increasing H_z the sample is initially in the Meissner state ($b = 0$) until $H_z > H_p = 4.5$ Oe where

b starts increasing rapidly. On decreasing H_z from its maximum value (10 Oe), b continues to increase initially until it reaches a maximum value, which is then roughly retained upon further field decrease[43]. This hysteretic behavior of the GB is markedly altered by the presence of even a small in-plane field. For $H_x = 5$ Oe the penetration field H_p is slightly reduced to 4.1 Oe and the ascending field branch is similar to the $H_x = 0$ case. However, on the descending branch, b is significantly below its maximum value and decreases rapidly, reaching zero at finite H_z. The shrinkage of the dome width upon decreasing field is in sharp contrast with GB model according to which vortices are trapped in the dome as long as the surrounding vortex-free region is present ($b < d - w/2$), and can leave the sample only when dome reaches the sample edges ($b = d - w/2$). This indicates that in the presence of in-plane field the vortices can surprisingly exit the sample by permeating through the vortex-free region that is impenetrable within the GB model. At a higher in-plane field $H_x = 30$ Oe the dome is formed already at $H_z = 2$ Oe, it shrinks back to zero with decreasing field for $H_z < 2$ Oe, and the dome width b behaves essentially reversibly following the equilibrium curve (dashed) of Fig. 3(a). This shows that the vortices in the dome are effectively in equilibrium with the vacuum and unexpectedly can now readily move in and out of the dome through the vortex-free region as H_z is varied.

The DMO imaging allows a very sensitive measurement of the dome width, but cannot provide a measure of the dc magnetization. In order to analyze the sample magnetization we have carried out a dc MO study in sample A. Due to the lower sensitivity the resulting data in Fig. 4(b) are nosier and less accurate, but qualitatively consistent. Figure 4(a) shows the calculated local magnetization loop $B - H$ in the center of the sample (solid lines) along with the equilibrium magnetization (dashed line). The large hysteresis is the result of the GB that gives rise to wide flux free regions on ascending field and essentially no flux-free regions on descending field. The experimentally measured local magnetization loop using MO imaging without modulation is shown in Fig. 4(b). In absence of in-plane field ($H_x = 0$) the behavior is consistent with the GB model. Application of H_x, however, significantly reduces the hysteresis on the ascending and descending branches showing that H_x facilitates both vortex entry and exit.

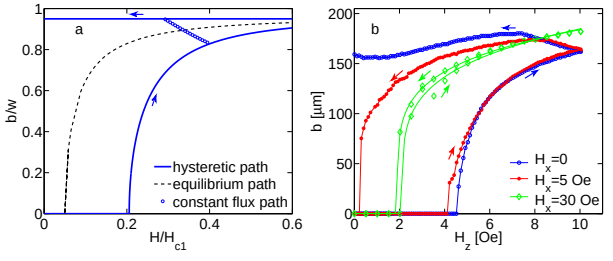

Figure 3. (color online) (a) The calculated half-width of the vortex dome b as H_z is increased from zero to $H_z \gtrsim H_{c1}$ and decreased to zero again (solid line) within the GB model for an infinitely long strip with $d/w = 0.1$. When H_z decreases from an intermediate value, the dome widens following a constant flux path (open circles) until it reaches the maximum value of $b = w - d/2$ at which the flux can exit the sample. The equilibrium dome width (dashed line) is shown for comparison describing the conditions of zero vortex energy in the dome. (b) The dome width measured in sample B at $T = 75$ K while ramping H_z from zero to 10 Oe and back in the presence of zero and non zero H_x showing that the in-plane field equilibrates the GB hysteresis.

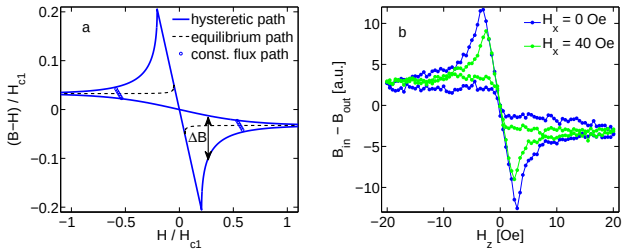

Figure 4. (color online) (a) The calculated local magnetization loop $B-H$ in the sample center within the GB model for the same parameters as in Fig. 3(a) (solid line) as compared to equilibrium behavior (dashed). ΔB is the width of the hysteresis. (b) The measured $B - H$ in the center of sample A (before FIB etching) at $H_x = 0$, 40 Oe and $T = 79$ K.

In order to quantify the reduction of the magnetic hysteresis we plot in Fig. 5 the measured hysteresis width, $|\Delta B|$ (see Fig. 4(a)), as a function of H_z and H_x. The figure shows that as $|H_x|$ is increased the hysteresis is suppressed significantly, however, the loop does not close completely and some hysteresis is seen around the penetration field even at the highest in-plane field we measured, 140 Oe.

The evidence shown so far points to the fact that the JV's introduced by the in-plane field significantly reduce the effectiveness of the geometrical barriers for some reason. In order to comprehend the microscopic origin of this phenomenon we have optimized our DMO imaging technique to resolve the PV chains along the JV's. The stacks of PV's that decorate the stacks of JV's were previously observed by Bitter decoration[35,44], scanning Hall probes[32,45] and MO imaging[34,36,37]. We find that by adjusting the modulation parameters the visibility of the chains can be greatly enhanced using either field or current modulation. This is demonstrated in Fig. 6, where the vortex chains are clearly visible as bright slightly tilted horizontal lines that are aligned along the direction of the in-plane field H_x. We verified that these lines are indeed vortex chains decorating the stacks of JV's by rotating the in-plane field and by varying H_x. We find that the lines are always aligned along the direction of H_x and their separation follows $\sqrt{2\gamma\Phi_0/\sqrt{3}|H_x|}$ with $\gamma = 480 \pm 70$, where $\Phi_0 = 20.7$ Gμm^2 is the flux quan-

tum and γ is the anisotropy parameter. In Fig. 6 the vortex dome is visible as a half-oval envelope that has a bright contrast on the right-hand-side and dark on the left-hand-side due to the current modulated DMO. We expect PV's to be present only inside the dome, residing on the JV stacks and between them depending on field strength[31], while in the vortex-free regions outside the dome the PV's should be absent due to the large Meissner currents and correspondingly high vortex potential[4–8]. The striking observation in Fig. 6 is that the vortex chains are visible both inside the dome as well as outside the dome forming whisker-like protrusions that extend all the way to the sample edges. This means that in presence of an in-plane field PV's can reside in the regions outside the dome that are vortex free in absence of H_x. A similar situation was observed by decoration experiments on BSCCO crystals in[14]. In Fig. 6 the vortex chains inside the dome have a stronger contrast as compared to the chains outside the dome. We find that this is not always the case and the whiskers may have stronger contrast than the chains in the dome depending on the field and modulation parameters.

We now present the hysteretic behavior of the dome with and without H_x. Figure 7(a) shows a DMO image using current modulation at $H_z = 3$ Oe in absence of in-plane field. At this field the sample is in the Meissner state on the ascending branch and vortex dome is absent, since $H_z < H_p$. On descending branch, however, the sample is in the mixed state and the dome is maximal as shown in Fig. 7(b). This highly hysteretic behavior of the dome is the result of flux trapping due to GB. In contrast, in presence of $H_x = 30$ Oe the dome has the same width on ascending and descending fields showing that the vortices are in equilibrium state. Figure 8 shows similar DMO images using field modulation at $H_z = 5$ Oe. In absence of in-plane field Fig. 8(a) shows a narrow dome just above the penetration on ascending field, while Fig. 8(b) shows a very wide dome on descending H_z branch. When $H_x = 30$ Oe is applied, the domes on ascending and descending branches become essentially identical. A movie showing the complete magnetization loop from which the Fig. 8 is extracted is available in Ref. 46.

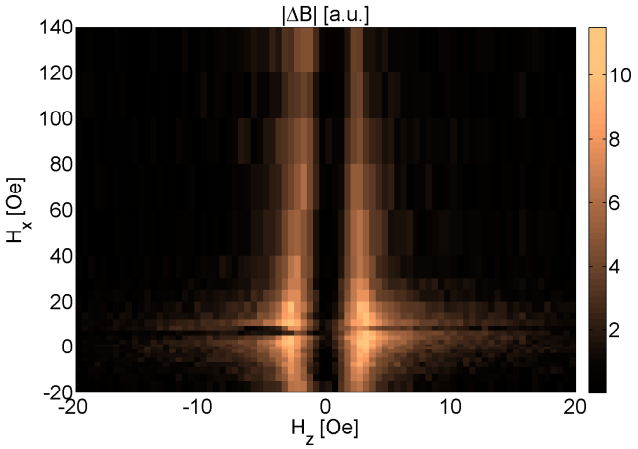

Figure 5. (color online) The width of the magnetization loop, $|\Delta B|$ (see Fig. 4), measured by sweeping H_z at various values of H_x. The discontinuities about $H_x \approx 0$ are an artifact due to the MO indicator.

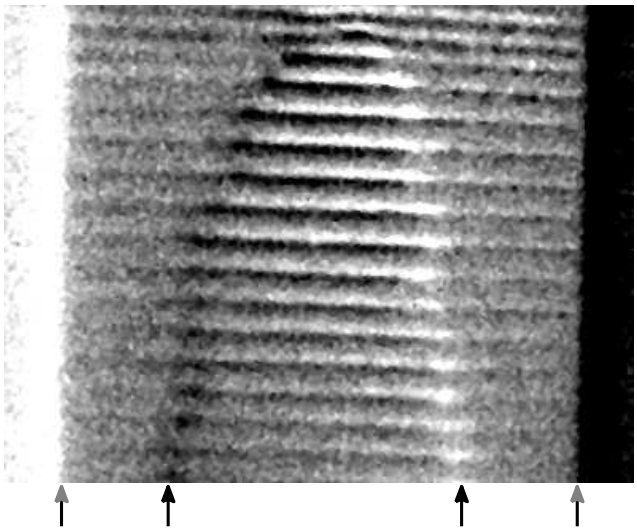

Figure 6. A current modulated DMO image of the decorated JV's (slightly tilted horizontal lines) inside and outside the dome in sample B. The two side edges of the sample are marked by gray arrows and the dome edges by black arrows. The center of the sample coincides approximately with the image bottom while the top edge of the sample is slightly above the top of the image. As a result, the visible dome has the shape of half an ellipse. The decorated JV's display a large contrast inside the dome while their whisker-like protrusions outside the dome display a lower contrast. The image was taken at $T = 77$ K, $H_z = 3.6$ Oe, $dI = 6$ mA and the gray scale corresponds to about 0.5 G. The image width is 0.4 mm.

The energy of the PV's that reside on JV's is lower due to their attractive interaction. Since the JV's transverse the entire sample, one could argue that the energy of the PV's could be lowered sufficiently by the JV stacks to extend into the GB in the vortex free region. The GB energy scale is $E_{gb} = \epsilon_0 d$, where $\epsilon_0 = H_{c1}\Phi_0/4\pi$, with the barrier being highest near the sample edges and gradually decreasing towards the dome[4]. The JV-PV interaction strength is given by crossing energy[31]

$$E_\times \approx \sqrt{\frac{\sqrt{3}\gamma B_x}{2\Phi_0}}\frac{2.1\Phi_0^2}{4\pi^2\gamma^2 s\ln(3.5\gamma s/\lambda)}, \qquad (1)$$

where $\gamma = 480$ as described above, $s = 15$Å is the layer spacing, and λ is the London penetration depth such that $\lambda = \lambda(0)/\sqrt{1-(T/T_c)^2}$ with $\lambda(0) = 2000$Å. In the case of our experimental conditions $E_\times \sim 10^{-2}E_{gb}$. Therefore, the degree of the spacial extension of the PV

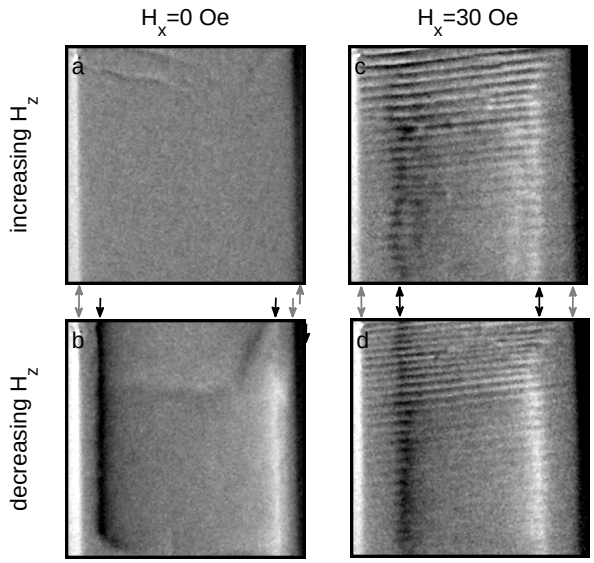

Figure 7. Current modulated DMO images at $H_z = 3$ Oe ($dI = 10$ mA, $T = 75$ K) of sample B taken along the magnetization loops shown in Fig 3(b) for $H_x = 0$ (left column) and $H_x = 30$ Oe (right column) on ascending (top row) and descending (bottom row) H_z branches. The left edge of the dome is dark and the right is bright (marked by black arrows), while the left edge of the sample is bright and the right is dark (marked by gray arrows). The slightly tilted horizontal stripes in (c) and (d) are PV chains. The gray scale is about 2.5 G in (a) and (b) and 1.5 G in (c) and (d). The images are 0.4 mm wide.

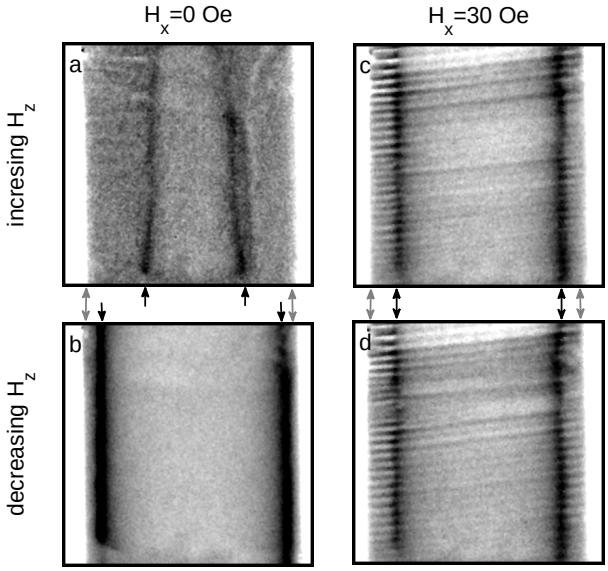

Figure 8. Field modulated DMO images at $H_z = 5$ Oe ($dH = 0.4$ Oe, $T = 75$ K) of sample B taken along magnetization loops in presence of $H_x = 0$ (left column) and $H_x = 30$ Oe (right column) on ascending (top row) and descending (bottom row) H_z branches. The dome edges are dark (marked by black arrows) and sample edges are bright (marked by gray arrows). The slightly tilted horizontal stripes in (c) and (d) are PV chains. The gray scale is about 1.25 G, 2.5 G, 1.8 G and 1.9 G in (a) to (d) respectively. The images are 0.5 mm wide. A movie showing the complete magnetization loops is available in Ref. 46.

whiskers into the vortex-free region should be extremely small, $\mathcal{O}(10^{-2})$ of the width of the flux-free region, and hence should be hardy observable. Nevertheless, our images clearly show that PV chains extend through the entire vortex-free region in sharp contrast to the above estimates.

It was recently shown that small local inhomogeneities in H_{c1} could lead to very large variations in the equilibrium local induction, a phenomenon attributed to demagnetization effects[47]. In order to see whether demagnetization can explain the phenomenon at hand we studied the GB mechanism in sample A after two shallow grooves were etched on its surface across the width of the sample as described above. We found that the grooves have a surprisingly large effect: a 160 nm deep groove, just 2% of the sample thickness, reduces the GB hysteresis comparable to the suppression by the in-plane field of about 10 Oe, and vortex whiskers are formed along the groove. The current modulated DMO image in Fig. 9 shows that on ascending field the whiskers along the groove (marked by arrows) have a contrast that is comparable to the dome in the pristine region but their extent is about 60% wider than the pristine dome. On the descending H_z branch the vortex dome in the pristine region closes gradually while the whiskers along the groove extend up to the sample edges similar to the behavior of the whiskers along the JV's.

V. DISCUSSION

The reduction of the GB by JV stacks has four main manifestations in our data: (*i*) suppression of the magnetic hysteresis, (*ii*) reduction of the penetration field with increasing $|H_x|$, (*iii*) presence of PV chains outside the bulk vortex dome, and (*iv*) on the descending H_z branch of the magnetization loop – the reduction of the bulk dome width to zero at some finite $H_z = H_0$, with H_0 increasing with increasing $|H_x|$.

We first evaluate the expected reduction of the GB due to a groove across the width of the sample, which can be formed either by FIB etching or effectively by the JV stacks caused by the energy reduction due to JV-PV interaction. Note that in addition to increasing the density of JV stacks, also the density of JV's in each stack increases with H_x, causing the effective groove depth to depend on B_x according to Eq. (1). As a result, one may expect a stronger suppression of GB with increasing H_x as observed experimentally.

Let us consider a sample of width $2w$ and thickness d

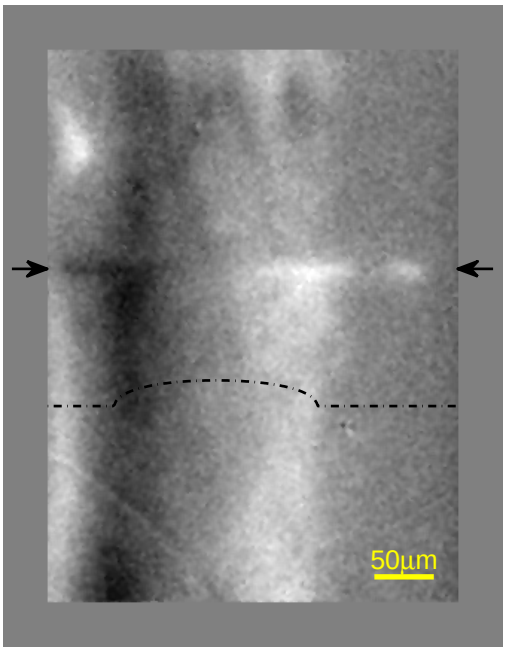

Figure 9. (color online) A zoomed-in view of the vortex dome in the central part of sample A after a groove 160 nm deep and 350 nm wide was etched across the width of the sample using FIB (marked by arrows). The image was obtained using current modulated DMO on ascending $H_z = 4$ Oe at $T = 82$ K and $dI = 10$ mA. The dome left (right) edge is dark (bright) and its schematic induction profile is shown by the dot-dashed line. Vortex whiskers protruding outside the dome are visible along the groove.

$(-d/2 \le z \le d/2)$ having a groove of depth δ extending from $x = -w$ to $x = w$. Since the vortex energy in the groove is lower, we expect that the vortex dome along the groove will be wider than in the bulk forming whisker-like protrusions of vortices into the flux free region. If the groove width, denoted by $2l$, is large enough, i.e. $l \gtrsim w$ then it can be described by the GB formulation following for example Ref. 42. Figure 10 shows for example the resulting vortex potential $U(x)$ and field $B(x)$ profiles in the bulk and along the groove of depth $\delta = 0.13d$ at $H_z = 0.065H_{c1}$ under equilibrium conditions, $U(x = 0) = 0$. Here the dome width in the bulk is $b = 0.4w$ while dome in the groove has $\tilde{b} = 0.5w$ resulting in whiskers that extend out of the bulk dome by 25%. Experimentally, in contrast, both the FIB etched groove and the effective grooves along the JV stacks have a much stronger effect: the FIB groove in Fig. 9 shows similar extent of the whiskers for groove depth of just $\delta = 0.02d$, while the JV stacks result in whiskers that commonly extend all the way to the sample edges with effective groove depth of the order of just $\delta = 0.01d$.

The above calculation, however, does not take into account the current I_x that flows along the groove-bulk interface, see Fig. 11, which may significantly enhance the described effect. This current plays a similar role to that of the edge current in the GB model and may significantly enhance the magnetic induction in the groove. Vortices can penetrate from the groove into the bulk only if the difference in their line energy $\epsilon_0\delta$ is canceled by the Lorentz potential due to that part of I_x which flows in a region of width $\sim \delta$ near the groove,

$$\frac{\Phi_0}{c}\int_l^{l+\delta} J_x(y)dy = \epsilon_0\delta, \qquad (2)$$

where $J_x(y)$ is the appropriate sheet current. $J_x(y)$ always keeps the induction in the groove higher than in the bulk, thus enhancing the effect of the groove and increasing the extent of the vortex whiskers. In the Meissner state $J_x(y) = 0$ and no current flows along the groove edges. At low fields, when the vortices are present only in the groove, $J_x(y)$ extends over the entire bulk. With increasing field, dome is formed in the bulk, decreasing the $J_x(y)$. When the field is high enough so that J_x flows only in the region of width $\sim \delta$ at the interface, the *total* interface current I_x reaches its minimum value $I_x^0 = c\epsilon_0\delta/\Phi_0 = cH_{c1}\delta/4\pi$ given by Eq. (2). The difference in the inductions at the groove center and bulk ΔB_{gr} which is proportional to I_x, depends on the geometry of the groove. For example, if the whole current I_x flows near the groove, one has $\Delta B_{gr} = (4\pi/c)I_x/d$ for the narrow groove, $l \ll d$, and $\Delta B_{gr} = (4/c)I_x/l$ in the opposite limiting case, $l \gg d$. Note that the enhancement of the field in the groove is essentially a demagnetization effect due to partial expulsion of the flux from the bulk. It is clear that for very wide grooves the effect is negligible and the result of Fig. 10 holds.

The sheet current $\mathbf{J}(x, y)$ and magnetic induction $B_z(x, y)$ can be calculated numerically for a finite size, two-dimensional film using the method described in Ref. 48. This method can be applied to the problem at hand in the limit of $d \ll l \ll w$. Here we demonstrate

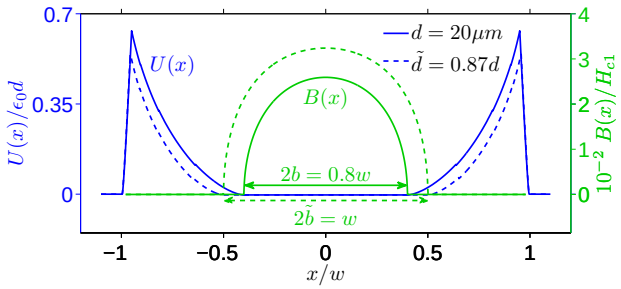

Figure 10. (color online) The equilibrium potential curves (black), $U(x = 0) = 0$, and induction profiles (gray) for two regions of a superconductor having different thicknesses, d (continuous line) and $\tilde{d}$ (dashed line), assuming both regions can be described by the GB mechanism. The difference in the edge barrier height in the two regions which is proportional to $\delta/d = (d - \tilde{d})/d$, is of the same order of magnitude as the normalized dome width difference $(\tilde{b} - b)/b$.

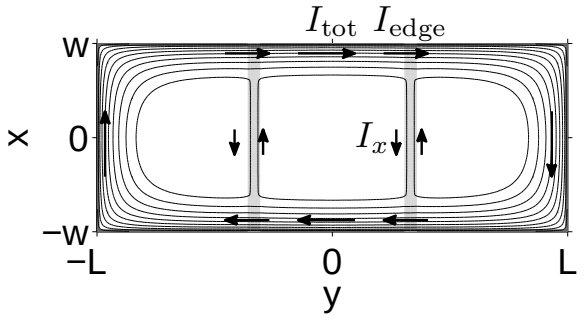

Figure 11. A numerical solution for the sheet current stream lines of a two-dimensional rectangular film of half-length L and half-width W ($W/L = 0.4$) with two grooves (shaded regions), each $2l = 0.06L$ wide, at $H_z/H_{c1} = 0.44$. The arrows indicate schematically the current flow directions. It is assumed that the penetration of the vortices into the groove begins when the sheet Meissner current at a distance $d/2$ from the platelet edge reaches $cH_{c1}/2\pi$. Here we took d=0.05L.

by this calculation that the dome in the groove can be noticeably wider than the dome in the bulk. To carry out the calculation, we rewrite condition (2) using the known solution for the sheet current and magnetic induction in the case when there is a magnetic flux in a narrow slit of the width $2l$ between two wide infinitely long strips in the Meissner state[49]. This solution can be used only if J_x flows in the region essentially wider than d, i.e., if $(4\pi/c)I_x \gg H_{c1}\delta$. Then, Eq. (2) can be rewritten as

$$B_z(x = 0, y = 0) = AH_{c1}, \qquad (3)$$

where A is a factor which depends on the distribution of the current density in the layer of the thickness δ near the groove. Strictly speaking, this distribution is essentially three-dimensional and cannot be found from the solution of Ref.[49]. We estimate that the factor A lies in the interval from $\sqrt{\delta/l}$ to $\sqrt{d/l}$. Since the calculation is done for a strictly 2D film, δ enters the calculation only through A which we take as $A = 0.5$ in the figures shown next. Figures 11 and 12 show the current stream lines and magnetic induction of a 2D superconductor having two grooves of width $2l = 0.06L$ at $H_z/H_{c1} = 0.44$. The interface current I_x as well as the flux focusing into the slits is clearly seen. Figure 12 shows that the dome in the grooves is wider than the bulk dome forming whiskers protruding into the flux free region. The induction in the grooves is much higher than in the bulk and interestingly, it is even higher than the applied field. The paramagnetic response of the grooves, $B_z > H_z$, is similar to the situation described in Ref. 47, where such phenomenon was described in terms of demagnetization effect.

Our numerical calculations also provide a qualitative understanding of the behavior on the descending field as follows. When the applied field is decreased, the bulk dome and the whiskers along the grooves expand until the whiskers reach the sample edges. Since the bulk and groove vortices remain in equilibrium, upon further decrease of H_z the vortices are drained out from the bulk through the groove. This process results in reduction of the width of the hysteresis loop and in magnetization value that is closer to the equilibrium magnetization on the descending branch. The inductions at both the groove and bulk centers decrease with decreasing H_z, but their difference, $\Delta B_{gr} \propto I_x^0 = cH_{c1}\delta/4\pi$ remains constant. Thus as H_z is reduced to zero the bulk dome contracts until all its vortices are drained out at a field $H_0 = H_{b=0}$ such that the induction at the groove center equals $\sim \Delta B_{gr}$. In order to estimate H_0, we note that at this field $B_z = 0$ in the bulk and the sample is in the Meissner state everywhere except in the grooves. In the Meissner state the total screening current circulating in a strip is $I_{tot} = cH_0 w/2\pi$[50,51]. Near the grooves this current splits into two paths: I_x^0 flows parallel to the groove and I_{edge} flows across the groove edge (see Fig. 11). Thus, we obtain $H_0 \approx H_{c1}\delta/2w + 2\pi I_{edge}/cw$. We can thus evaluate H_0 by noting that the edge current lies in the interval $0 \le I_{edge} \lesssim cH_{c1}d/4\pi^4$. This estimate for the range of H_0 is in reasonable agreement with the experimental values of H_0 seen on the descending branches of $b(H_z)$ in Fig. 3b.

The above description provides a qualitative explanation of the creation of vortex whiskers, suppression of hysteresis, and shrinkage of the bulk vortex dome on descending field. Quantitatively, however, the groove depths that are required in order to describe the experimental data are still about an order of magnitude larger than the ones obtained from Eq. (1). Our numerical calculations are applicable only for not too narrow grooves $d \ll l \ll w$, while the JV stacks create effective grooves with $l \ll d$. In this case we expect further enhancement of the demagnetization effects that could perhaps resolve

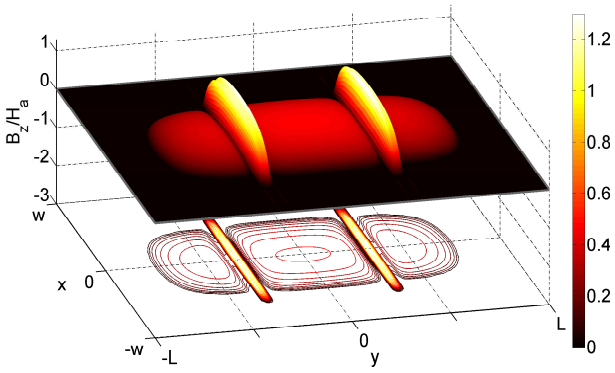

Figure 12. (color online) A numerical solution for magnetic induction B_z corresponding to the conditions of Fig. 11. The field in the two grooves is higher than the applied field similar to the situation described in Ref 47.

the discrepancy. Interestingly, the JV-PV crossing energy $E_\times$ was evaluated experimentally to be about seven times larger than the theoretical value by comparing $E_\times$ with the vortex line energy in wide grooves[37]. The origin of this discrepancy could be related to the same observation that the effective grooves due to JV's are much narrower, thus having a large field enhancement due to demagnetization effects in the thin samples in perpendicular field.

The presented model, however, does not explain why the penetration field decreases significantly with increasing H_x. In the full Meissner state $I_x = 0$ and therefore H_p cannot be affected by it. Since in GB model $H_p \approx H_{c1}\sqrt{d/w}$, the bare reduction of the thickness along the JV effective grooves should lower H_p in our case by only less than 1%, in sharp contrast to more than 50% reduction in H_p in Fig. 3(b). This essential reduction of H_p may be due to a more intriguing mechanism in the vicinity of the edges in which an inhomogeneous penetration of the vortices into the edge region leads to a concentration of the magnetic field in the groove edges. As a result, an enhanced penetration of the vortices along the groove develops that noticeably decreases the observed penetration field.

VI. SUMMARY

We used the DMO technique to image the field distribution and the local magnetization of thin BSCCO crystals at elevated temperatures at which the magnetic hysteresis is governed by the geometrical barrier mechanism. In this regime a vortex dome is present in the central part of the sample surrounded by a vortex-free potential barrier region. We found that stacks of Josephson vortices caused by an in-plane magnetic field significantly reduce the GB and allow formation of pancake vortex chains or whiskers in regions that should otherwise be vortex-free. These whiskers extend from the dome up to the sample edges, thus forming easy channels for vortex flow through the potential barrier. As a result the magnetic hysteresis is reduced and the magnetization loops become reversible at elevated in-plane fields. We also found that a FIB etched narrow and shallow groove has a similar effect on the GB.

Our analysis shows that the bare reduction of the vortex energy due to the JV-PV crossing energy along the JV stacks or due to reduced thickness along the etched grooves is one to two orders of magnitude lower than the height of the GB, and therefore cannot account for the observed phenomena. We present a model in which the effect of the grooves is significantly enhanced due to the demagnetization factor in the platelet geometry in perpendicular field. The flux that is partially expelled from the pristine regions is focused into the grooves, thus enhancing the local induction in the grooves and suppressing the barrier. The presented numerical calculations demonstrate qualitatively this demagnetization enhancement, and provide an important insight into the long-standing puzzle of suppression of the macroscopic GB by in-plane field. Our numerical method can only treat grooves that are wide on the scale of sample thickness, which are much wider than in experimental situation. A proper calculation of narrower grooves is therefore required, which is expected to provide a better quantitative agreement with the data. One important experimental observation, the suppression of the penetration field by the JV stacks, however, remains unexplained within the model. This feature is apparently a result of microscopic inhomogeneities in the sample edge regions introduced by the JV's that facilitate vortex penetration into the sample. Such inhomogeneities cannot be treated within our current numerical studies and will be the subject of future investigations.

ACKNOWLEDGMENTS

We wish to thank the Electron Microscopy Unit in the Weizmann Institute of Science for providing us access to the FEI Helios Focused Ion Beam system. This research was supported by the German-Israeli Foundation for Scientific Research and Development (GIF) and by the US-Israel Binational Science Foundation (BSF). EZ acknowledges the support of EU-FP7-ERC-AdG.

* yehonathan.segev@gmail.com;
http://www.weizmann.ac.il/condmat/superc/

[1] G. Blatter, M. V. Feigelman, V. B. Geshkenbein, A. I. Larkin, and V. M. Vinokur, Reviews Of Modern Physics **66**, 1125 (1994).
[2] A. Pautrat, J. Scola, C. Goupil, C. Simon, C. Villard, B. Domengès, Y. Simon, C. Guilpin, and L. Méchin, Phys. Rev. B **69**, 224504 (2004).
[3] C. P. Bean and J. D. Livingston, Phys. Rev. Lett. **12**, 14 (1964).
[4] E. Zeldov, A. I. Larkin, V. B. Geshkenbein, M. Konczykowski, D. Majer, B. Khaykovich, V. M. Vinokur, and H. Shtrikman, Phys. Rev. Lett. **73**, 1428 (1994).
[5] M. Indenbom, H. Kronmüller, T. Li, P. Kes, and A. Menovsky, Physica C: Superconductivity **222**, 203 (1994).
[6] M. Benkraouda and J. R. Clem, Phys. Rev. B **53**, 5716 (1996).
[7] E. H. Brandt, Phys. Rev. B **60**, 11939 (1999).
[8] E. H. Brandt, Phys. Rev. B **59**, 3369 (1999).
[9] T. Schuster, M. V. Indenbom, H. Kuhn, E. H. Brandt, and M. Konczykowski, Phys. Rev. Lett. **73**, 1424 (1994).
[10] J. Clem, Journal of Superconductivity and Novel Magnetism **21**, 343 (2008).
[11] M. Willemin, A. Schilling, H. Keller, C. Rossel, J. Hofer,

U. Welp, W. K. Kwok, R. J. Olsson, and G. W. Crabtree, Phys. Rev. Lett. **81**, 4236 (1998).
[12] N. Avraham, B. Khaykovich, Y. Myasoedov, M. Rappaport, H. Shtrikman, D. E. Feldman, T. Tamegai, P. H. Kes, M. Li, M. Konczykowski, K. van der Beek, and E. Zeldov, Nature **411**, 451 (2001).
[13] H. Beidenkopf, N. Avraham, Y. Myasoedov, H. Shtrikman, E. Zeldov, B. Rosenstein, E. H. Brandt, and T. Tamegai, Phys. Rev. Lett. **95**, 257004 (2005).
[14] T. Tamegai, M. Matsui, M. Yasugaki, N. Kamada, Y. Tokunaga, and M. Tokunaga, Superconductor Science and Technology **17**, S88 (2004).
[15] S. J. Bending, A. N. Grigorenko, I. A. Crisan, D. Cole, A. E. Koshelev, J. R. Clem, T. Tamegai, and S. Ooi, *Proceedings of the 16th International Symposium on Superconductivity (ISS 2003). Advances in Superconductivity XVI. Part I*, Physica C: Superconductivity **412-414**, 372 (2004).
[16] S. Kasahara, Y. Tokunaga, N. Kameda, M. Tokunaga, and T. Tamegai, Phys. Rev. B **71**, 224505 (2005).
[17] M. Konczykowski, C. J. van der Beek, A. E. Koshelev, V. Mosser, M. Dodgson, and P. H. Kes, Phys. Rev. Lett. **97**, 237005 (2006).
[18] I. Gutman, S. Goldberg, Y. Segev, Y. Myasoedov, E. Zeldov, and T. Tamegai, Physica C: Superconductivity **470**, S239 (2010), proceedings of the 9th International Conference on Materials and Mechanisms of Superconductivity.
[19] D. Majer, E. Zeldov, and M. Konczykowski, Phys. Rev. Lett. **75**, 1166 (1995).
[20] C. J. Van der Beek, M. V. Indenbom, G. D'Anna, and W. Benoit, Physica C: Superconductivity **258**, 105 (1996).
[21] D. T. Fuchs, E. Zeldov, M. Rappaport, T. Tamegai, S. Ooi, and H. Shtrikman, Nature **391**, 373 (1998).
[22] H. Beidenkopf, Y. Myasoedov, E. Zeldov, E. H. Brandt, G. P. Mikitik, T. Tamegai, T. Sasagawa, and C. J. van der Beek, Phys. Rev. B **80**, 224526 (2009).
[23] A. Boehmer, M. Konczykowski, and C. van der Beek, arxiv **arXiv:1004.5309** (2010).
[24] N. Morozov, E. Zeldov, M. Konczykowski, and R. A. Doyle, Physica C: Superconductivity **291**, 113 (1997).
[25] E. H. Brandt and G. P. Mikitik, Phys. Rev. Lett. **89**, 027002 (2002).
[26] G. P. Mikitik and E. H. Brandt, Phys. Rev. B **67**, 104511 (2003).
[27] G. P. Mikitik and E. H. Brandt, Phys. Rev. B **69**, 134521 (2004).
[28] L. Burlachkov, V. B. Geshkenbein, A. E. Koshelev, A. I. Larkin, and V. M. Vinokur, Phys. Rev. B **50**, 16770 (1994).
[29] J. R. Clem, Phys. Rev. B **43**, 7837 (1991).
[30] L. N. Bulaevskii, M. Ledvij, and V. G. Kogan, Phys. Rev. B **46**, 366 (1992).
[31] A. E. Koshelev, Phys. Rev. Lett. **83**, 187 (1999).
[32] A. Grigorenko, S. Bending, T. Tamegai, S. Ooi, and M. Henini, Nature **414**, 728 (2001).
[33] S. J. Bending and M. J. W. Dodgson, Journal of Physics: Condensed Matter **17**, R955 (2005).
[34] M. Tokunaga, T. Tamegai, Y. Fasano, and F. de la Cruz, Phys. Rev. B **67**, 134501 (2003).
[35] C. A. Bolle, P. L. Gammel, D. G. Grier, C. A. Murray, D. J. Bishop, D. B. Mitzi, and A. Kapitulnik, Phys. Rev. Lett. **66**, 112 (1991).
[36] V. K. Vlasko-Vlasov, A. Koshelev, U. Welp, G. W. Crabtree, and K. Kadowaki, Phys. Rev. B **66**, 014523 (2002).
[37] T. Tamegai, M. Matsui, and M. Tokunaga, *Proceedings of the 16th International Symposium on Superconductivity (ISS 2003). Advances in Superconductivity XVI. Part I*, Physica C: Superconductivity **412-414**, 391 (2004).
[38] E. Zeldov, J. R. Clem, M. McElfresh, and M. Darwin, Phys. Rev. B **49**, 9802 (1994).
[39] A. Soibel, E. Zeldov, M. Rappaport, Y. Myasoedov, T. Tamegai, S. Ooi, M. Konczykowski, and V. B. Geshkenbein, Nature **406**, 282 (2000).
[40] N. Morozov, E. Zeldov, D. Majer, and B. Khaykovich, Phys. Rev. Lett. **76**, 138 (1996).
[41] S. S. Banerjee, S. Goldberg, A. Soibel, Y. Myasoedov, M. Rappaport, E. Zeldov, F. de la Cruz, C. J. van der Beek, M. Konczykowski, T. Tamegai, and V. M. Vinokur, Phys. Rev. Lett. **93**, 097002 (2004).
[42] E. Zeldov, A. I. Larkin, M. Konczykowski, B. Khaykovich, D. Majer, V. B. Geshkenbein, and V. M. Vinokur, Physica C: Superconductivity **235-240**, 2761 (1994).
[43] The slight decrease in the value of b on decreasing field can be readily attributed to small remnant in-plane field considering the dramatic effect of non-zero H_x, and to the finite dH field modulation used in DMO imaging.
[44] I. V. Grigorieva, J. W. Steeds, G. Balakrishnan, and D. M. Paul, Phys. Rev. B **51**, 3765 (1995).
[45] A. N. Grigorenko, S. J. Bending, A. E. Koshelev, J. R. Clem, T. Tamegai, and S. Ooi, Phys. Rev. Lett. **89**, 217003 (2002).
[46] See EPAPS Document No. [number will be inserted by publisher] for a complete movie of the magnetization loop from which Fig. 8 is extracted.
[47] N. Avraham, E. H. Brandt, G. P. Mikitik, Y. Myasoedov, M. Rappaport, E. Zeldov, C. J. van der Beek, M. Konczykowski, and T. Tamegai, Phys. Rev. B **77**, 214525 (2008).
[48] E. H. Brandt, Phys. Rev. B **72**, 024529 (2005).
[49] A. A. B. Brojeny, Y. Mawatari, M. Bekraouda, and J. R. Clem, Superconductor Science and Technology **15**, 1454 (2002).
[50] A. Larkin and Y. Ovchinnikov, Zhurnal Eksperimental'noi i Teoreticheskoi Fiziki **61**, 1221 (1971).
[51] R. P. Huebener, R. T. Kampwirth, and J. R. Clem, Journal of Low Temperature Physics **6**, 275 (1972), 10.1007/BF00628313.

4.2 The Effect of JVs on the Melting Transition

4.2.1 Introduction

A considerable part of the studies regarding the vortex lattice phase diagram were done in BSCCO, usually at zero in-plane field where the Josephson vortex lattice can be disregarded. Since the JVs and PVs interact, the PV lattice melting in the presence of JVs should obviously be very different from what is expected of an isotropic superconductor in tilted magnetic fields. The effect of an in-plane magnetic field on the melting line in BSCCO, a highly anisotropic superconductor was studied experimentally in Refs.105,106. It was found that over a wide range of in-plane fields, roughly 0–1000 Oe, the melting field at a given temperature decreases linearly with increasing in-plane field. This result was explained theoretically in Ref. 51 for the range of fields relevant to the reported experiments — at relatively high PV densities. Some modification to the melting landscape due to high in-plane fields was reported in Ref. 107, who reported some elongation of the melting puddles in the direction of the in-plane field. This effect was attributed in the report to the magnetization of the sample in oblique magnetic fields, which causes the magnetic induction to be higher in the sample regions that are facing the in-plane field and was not related to the existence of the JV lattice.

The effect of JVs on the lattice melting at low PV densities was considered neither theoretically nor experimentally. Although it might be natural to think that the melting of a slightly deformed lattice should nucleate on the JV stacks i.e.— on the lattice deformations, it is by no means trivial that this is the case for the chain-and-lattice state. One can argue to the contrary that in this state the PVs are trapped in the caging potential caused by the JVs and that bound vortices make stiffer lattices that melt at higher temperatures and fields as was seen, for example, in samples with heavy ion induced columnar defects [96].

In this work we performed an experimental study of the effect of JVs on the lattice melting. We found that at low melting fields (i.e. close enough to T_c) the PV lattice melting landscape is altered by the presence of the Josephson lattice and that the PV chains melt first. Furthermore we found that the difference of the melting fields, on the chains and between them, is about an order of magnitude higher than the reduction of the melting field seen at high fields.

4.2.2 Experimental Details

The data presented below are taken from two optimally doped $Bi_2Sr_2CaCu_2O_{8+\delta}$ single crystals, SarFIB1C and Y1B, grown by T. Tamegai of the University of Tokyo, which we will refer to, in this section, as Sample A and B, with a critical temperature of $T_c \approx 92$ K and anisotropy of $\gamma \approx 500$. The latter was measured by the technique described in Section 3.3. The measurements were done using the differential magneto-optics technique, with either field or current modulation to visualize the vortex chains, and temperature or field modulation to visualize the melting transition.

4.2.3 Results

The melting transition is accompanied with a discontinuous jump in the magnetic induction. Thus, regions in the superconductor that are driven through the transition by the modulation, show up as regions of high intensity in DMO images. Regions that are kept in a single phase, ordered or disordered, during the modulation, remain relatively dark. An example of a typical DMO image of a BSCCO sample around the melting transition is shown in Fig. 4.1a, which shows a field modulated image of Sample A. The shape of the melting front, the bright, long (horizontal) lines or arcs, is characteristic of melting in BSCCO and results from growth defects. These defects, which result from small variability of the crystal growing conditions during the crystal growth, cause an inhomogeneity in the crystal doping, and thus a small inhomogeneity in T_c and the dependence of the melting field, B_m, on the temperature [95]. As we show below this landscape is dramatically altered due to the crossing lattice state.

First, we repeat the experiment of Refs 51, 105, 106, which report a decrease in bulk melting field with the application of IP fields. We perform H_z scans around the melting transition at various fixed IP fields at $T = 87$ K, and for each scan find the average melting field in some region on interest (ROI). For each scan, the local melting field, $H_z = H_m(T, H_{IP}; x, y)$, is defined as the lowest field at which a pixel in a field modulated image series passes some threshold intensity. The spatially averaged melting field $H_z = \langle H_m(T, H_{IP})\rangle_{ROI}$ is the field where the maximum number of pixels have gone through the transition within the ROI marked by the rectangle in Fig. 4.1a[1]. The dependence of this averaged melting field on the IP field is shown in Fig. 4.1b. Qualitatively, the decrease in the melting field is reasonably consistent with the reported linear dependence. Although the theoretical slope given by Ref. 51 is about four times greater, discrepancies of a similar

1 If the maximum is multiply valued, $\langle H_m\rangle_{ROI}$ is the maximum corresponding to the lowest field.

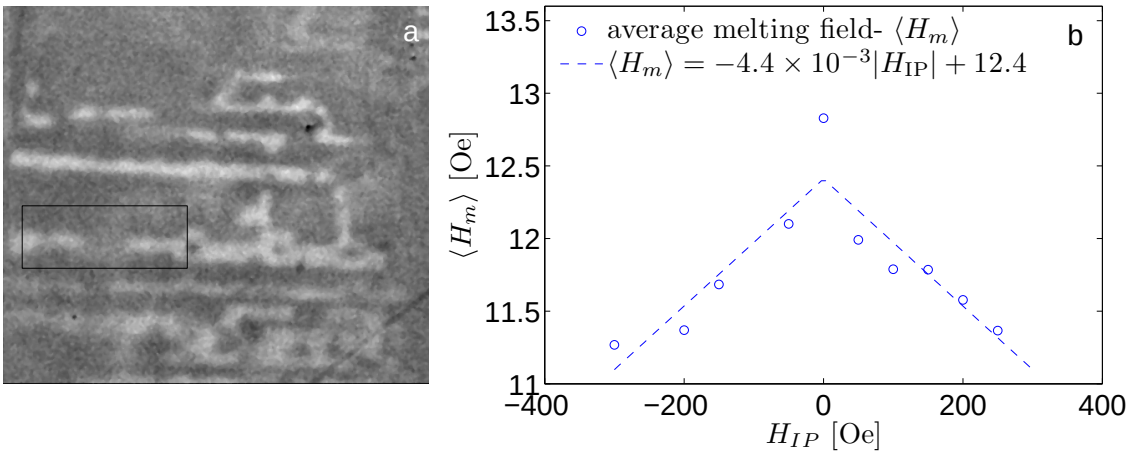

Figure 4.1: *(a) A field modulated MO image (dH = 0.5 Oe) of sample A at T = 84 K, $H_z = 23$ Oe and $H_{\rm IP} = 0$. (b) The melting field $H_z = H_m$ in the region of interest shown by the rectangle in (a) as a function of in-plane field at T = 87 K.*

order between the experiment and the theory were reported in this report. One can also note that similar to the data shown in Ref. 51 the decrease in $\langle H_m \rangle$ around $H_x = 0$ is sharper than at higher $H_{\rm IP}$ values.

We next turn to study the local effect of the JVs on the melting landscape. Figures 4.2a and 4.2b show the melting transition in Sample A for $H_{\rm IP} = 30$ Oe applied at an in-plane angle of 60° and 120° respectively. The regions that go through the melting transition show up in these images as bright areas tending to white. For comparison, figures 4.2c and 4.2d show images taken under the same condition as figures 4.2a and 4.2b respectively, but at lower perpendicular field, $H_z < H_m$, which allows the distinction of the PV chains that show up as slanted diagonal lines crossing the sample. The comparison of the melting and chain images clearly demonstrates that the JV lattice structure competes with the crystal defects over dominance of the melting landscape. Although the melting areas still show the effect of the horizontal growth defects, regions that showed homogenous melting at $H_{\rm IP} = 0$, show melted segments that are parallel to the JV stacks and have the same spacing.

The inhomogeneity of the melting transition across the sample makes the melting width — the typical range of fields (or temperatures) in which the entire sample melts — be much larger than the local reduction of the melting field due to the JVs. As a result our images capture the melting transition on a portion of the chains in each frame. Thus, the effect of the chains is better visualized in a sequence of images that shows the entire melting transition. Movies of such sequences are available at [109]. Fig. 4.3 shows several images from such a sequence showing a temperature sweep through the

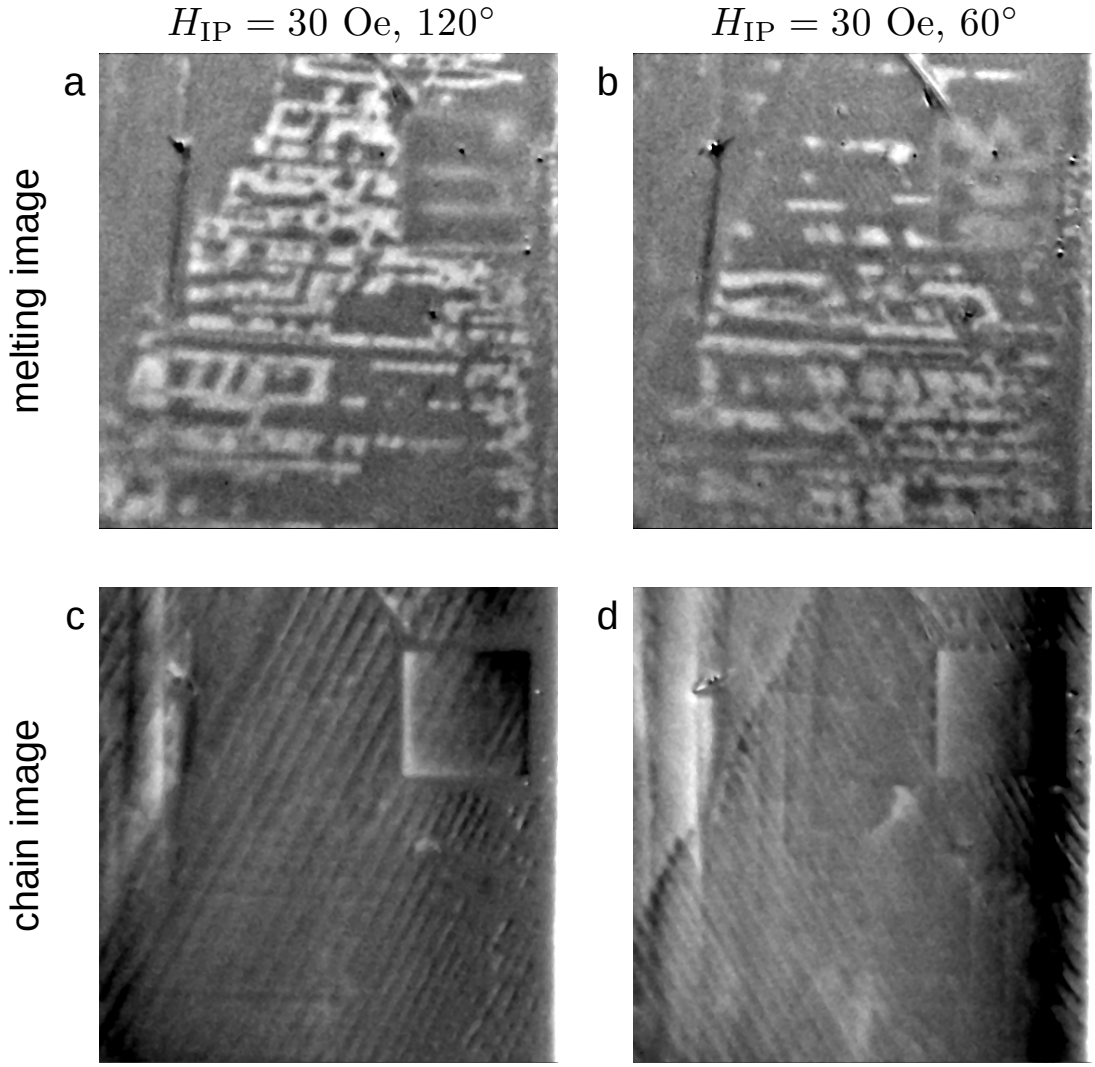

Figure 4.2: *(a) A field modulated MO image of the melting transition with $H_{IP} = 30$ Oe applied at 60° with zero degrees chosen arbitrarily to point right, along the horizontal image direction (also, $H_z = 20$ Oe, $T = 85$ K and $dH = 0.5$ Oe). (b) The melting transition at an IP angle of 120° and $H_z = 20.5$ Oe. The rest of parameters are the same as in (a). (c) and (d) field modulated images showing the PV chains. The images were taken at the same conditions as (a) and (b) apart from the perpendicular magnetic field $H_z = 3$ Oe and $H_z = 7$ Oe, respectively. The images are 0.6 mm wide and the square in the top right of the image is an area of focused ion beam (FIB) made defects intended for a different experiment [108].*

melting transition in Sample A with an IP field the same as in Fig. 4.2a and Fig. 4.2c. The sequence demonstrates that the modulation of the local melting field (temperature) is typically smaller than the melting width, which is governed by the growth defects. However, within areas of relative homogenous melting JV creates a secondary melting

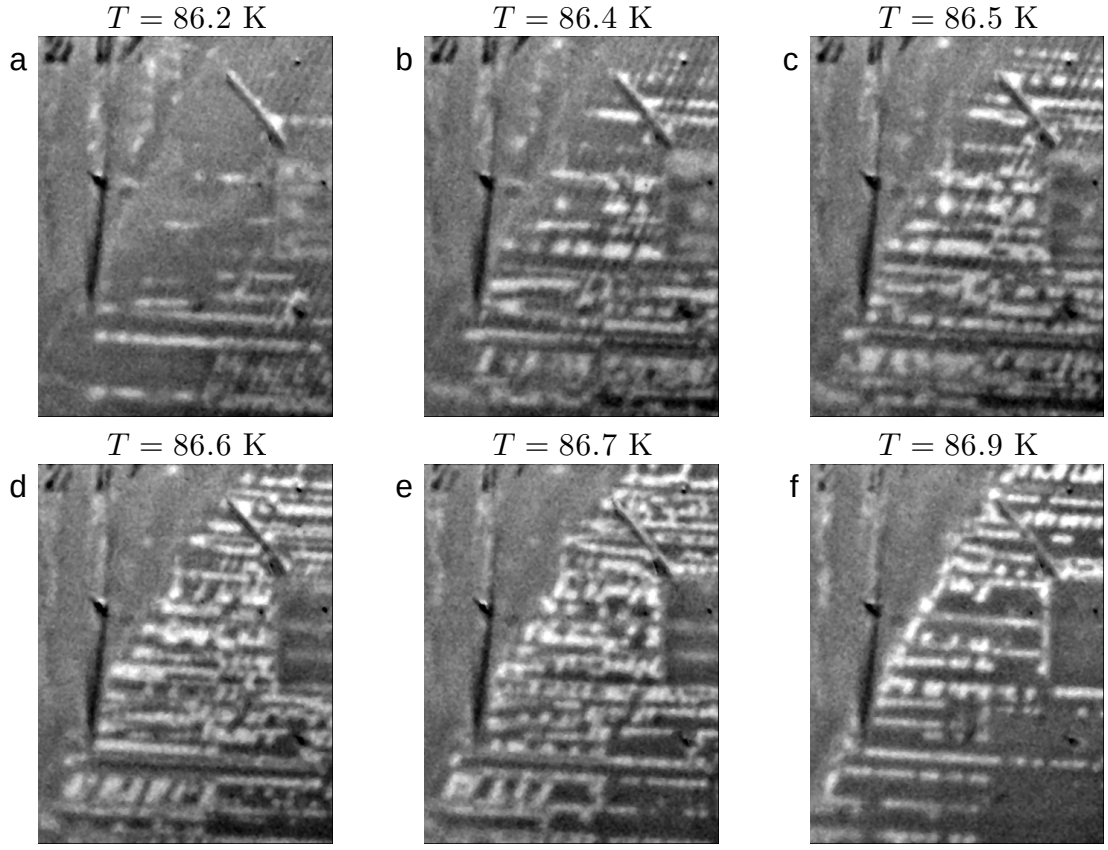

Figure 4.3: *A sequence of field modulated DMO images ($dH = 1$ Oe) showing the progression of the melting transition in Sample A in the presence of JVs. The melting front (white regions) appears to follow the sample growth defects (horizontal lines) and the JVs (diagonal lines). The sample is held at a constant field (apart of the modulation field), $H_z = 15$ Oe, $H_{\mathrm{IP}} = 30$ Oe, $120°$ as the temperature is increased. The images are 0.5 mm wide. A movie showing the full image sequence at the transition is available at [109].*

landscape.

Sample B shows the same qualitative phenomena but the melting transition is slightly more homogenous in it, so typical melting images show wider melting areas for a given modulation strength. This is demonstrated in Figure 4.4 which shows the melting and the PV chains for different IP field magnitudes and directions. Each melting image is taken at the same temperature and IP field as the image below it, which shows the PV chains. Since the melting width in this sample is much narrower than in Sample A, smaller modulating signals had to be used in order to measure the transition landscape. The qualitative effect of the IP field is similar to the one seen above, where the melting regions seem to follow the PV chains. This is most clearly seen in the left side of Fig. 4.4c

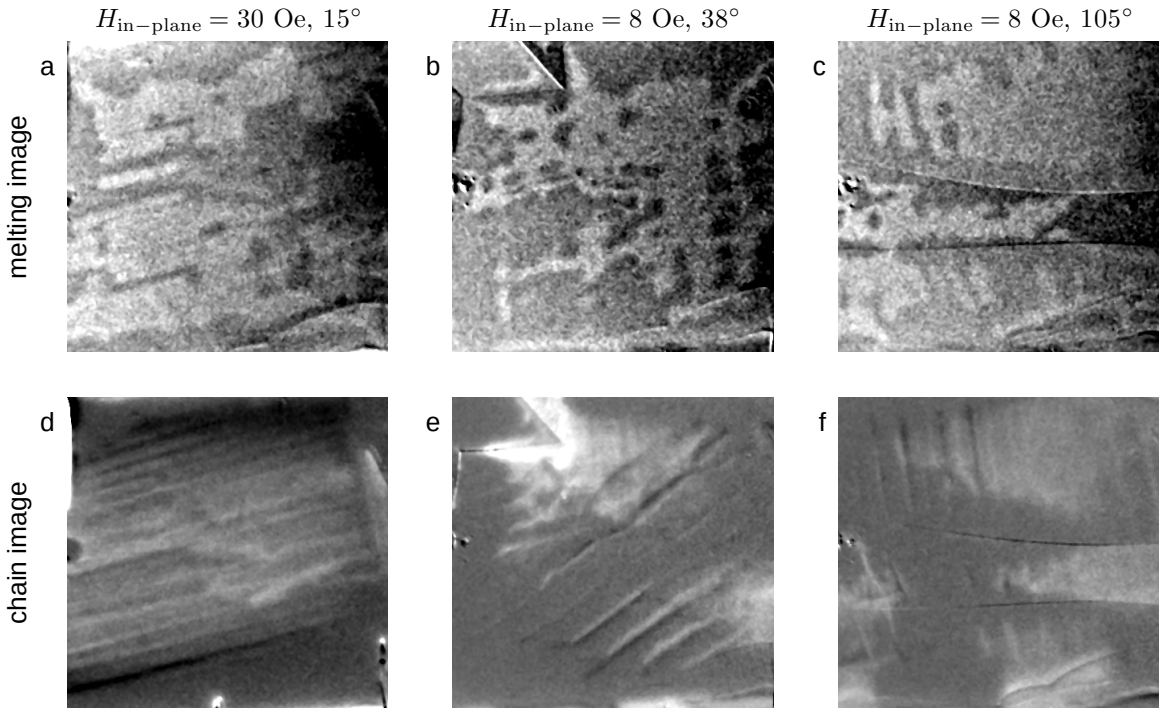

Figure 4.4: *(a)–(c) Melting images in Sample B taken at (a) $H_{\mathrm{IP}} = 30$ Oe, 15°, (b) $H_{\mathrm{IP}} = 8$ Oe, 38° and (c) $H_{\mathrm{IP}} = 8$ Oe, 105°. (d)–(f) PV images taken under the same IP field and temperature as figures (a)–(c) respectively. The triangular defect in the top left of images (b) and (d) and the two horizontal arcs in the center of images (c) and (f) are features due to the magneto-optical indicator and are characteristic of low field measurements.*
***Other physical parameters**, (a) $T = 85$ K, $H_z = 23$ Oe, field modulation $dH = 1$ Oe, (b) $T = 87$ K, $H_z = 13.2$ Oe, temperature modulation $dT = 0.2$ K, (c) $T = 87$ K, $H_z = 13.5$ Oe, temperature modulation $dT = 0.2$ K, (d) $T = 85$ K, $H_z = 2$ Oe, field modulation $dH = 1$ Oe, (e) $T = 87$ K, $H_z = 0.2$ Oe, field modulation $dH = 0.25$ Oe, and (f) $T = 87$ K, $H_z = 0.8$ Oe, field modulation $dH = 0.25$ Oe. All images are 0.5 mm wide.*

where long vertical arc-like puddles are seen where Fig. 4.4f shows PV chains.

Figure 4.5 displays several field modulated images taken along a field sweep through the melting transition in Sample B under the same IP field and temperature as in Fig. 4.4c. The sequence shows that the melting nucleates on JVs at the top of the sample and as the transition progresses the melting regions become longer and wider, covering a longer portion along the JV, and covering larger areas between the chains. When the melting regions on two adjacent JVs reach one another, the melting puddle starts losing its shape and surface tension starts to play a role, leading to rounder melting regions. Note that similar to what can be seen in the sequence shown in Fig. 4.3, the melting nucleates in narrows stripes, which are significantly narrower than the JV spacing. This leads us to conclude that the *JV lattice lowers* H_m and T_m, and that the melting nucleates on the

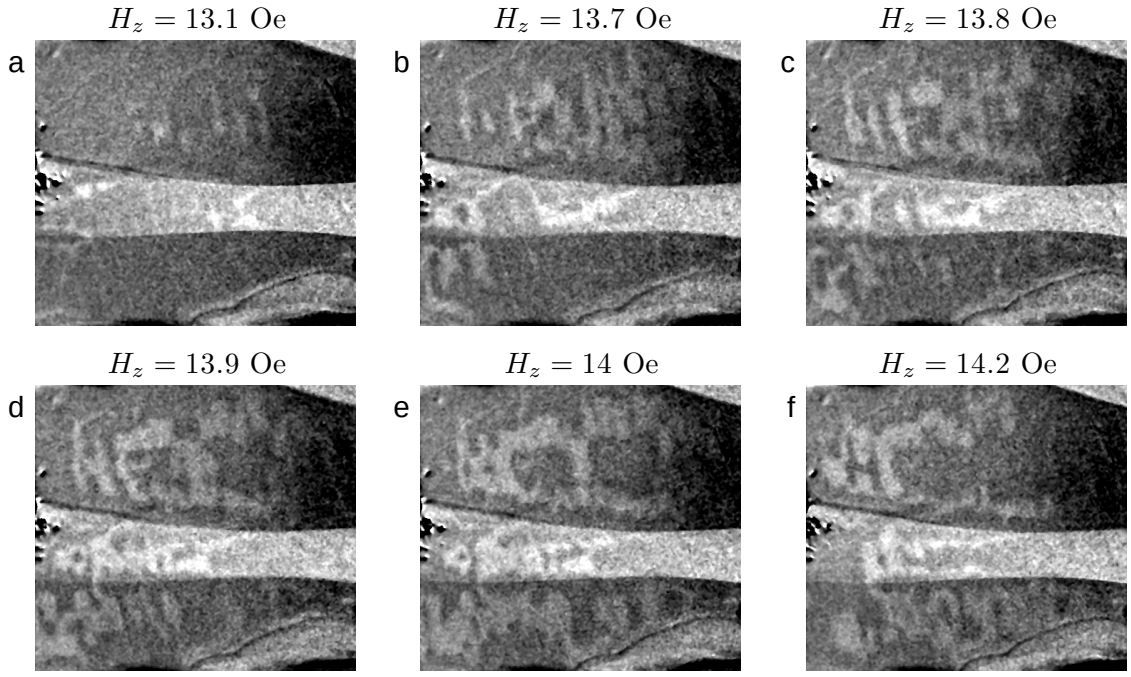

Figure 4.5: *A sequence of images showing the progression of the melting transition in Sample B in the presence of JVs. The images are part of a sequence of field modulated images, $dH = 0.25$ Oe, taken at $T = 87$ K, $H_{\rm IP} = 8$ Oe$, 105°$, while the field was ramped up from $H_z = 12$ Oe to $H_z = 16$ Oe. The lighter horizontal stripe in the middle of the images and the top right corner is a feature due to the magneto-optical indicator. The images are 0.6 mm wide.*

JVs rather than between them.

In order visualize with greater clarity the interplay of the sample intrinsic growth defects, the JV lattice and liquid surface tension we show in Fig. 4.6 a zoomed in view of a region of interest in Sample A (marked by the rectangle at Fig. 4.7a) as it goes through the melting transition. The sequence shows temperature modulated images, $dT = 0.4$ K, of the melting transition at $T = 87$ K and $H_{\rm IP} = 5$ Oe$, 120°$. In order to keep track of the melting front propagation, there are dashed lines overlayed on the images, in the same position in all images. These lines are parallel to the PV chains as visualized in Fig. 4.7a and have the approximately the same spacing. The figure shows that melting nucleates on the crossings of the JVs with the horizontal growth defects (a), and then the melting front progresses on the defects between the chains (b). In Fig. 4.6c one sees that melting nucleates on the JVs between the defects and as the melting proceeds the melting front becomes wider (d), until the melting regions on the JVs reach each other ((e) and (f)). Note also that as the melting regions which nucleated on the JVs widen, their direction

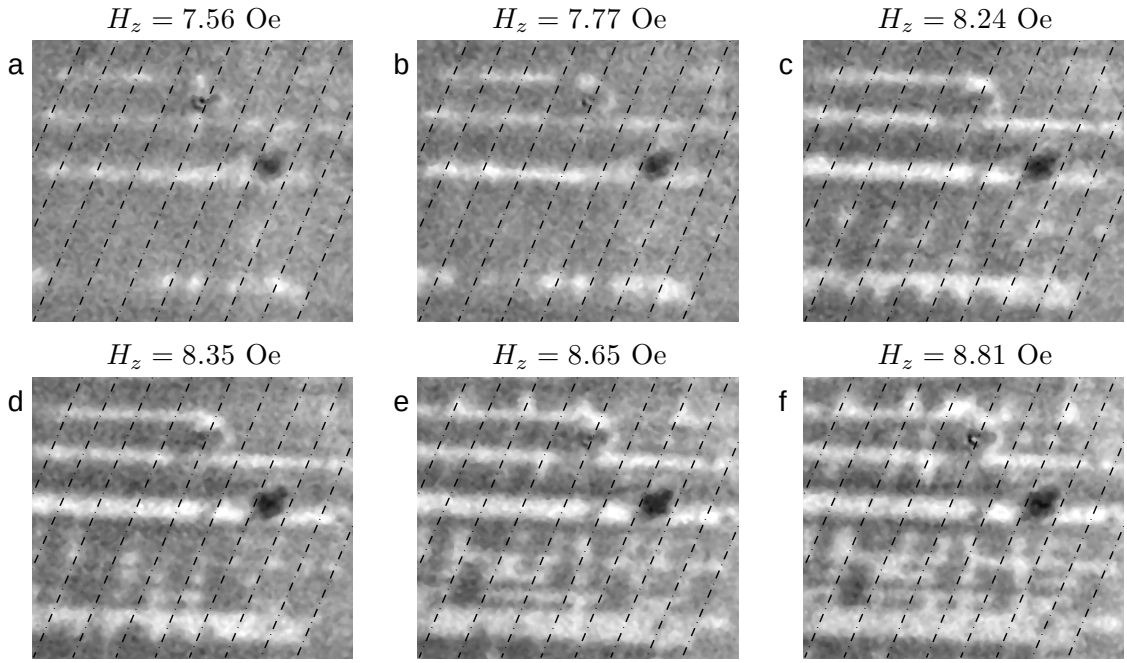

Figure 4.6: *The progression of the melting transition in Sample A at $T = 87$ K and $H_{\mathrm{IP}} = 5$ Oe, $120°$. The overlayed dashed lines are guide to the eye and are the same in all images. The lines are directed along the PV chains as visualized in Fig. 4.7a and approximately have the same spacing. The images are temperature modulated images with $dT = 0.4$ K and are 270 μm wide.*

changes due to the surface tension and they become perpendicular to the growth defects (compare lower half of (c) to (e) and (f)).

In order to quantify the effect of the PV lattice on the melting, we measure the melting field at each pixel, in the field scan which is partially shown in Fig. 4.6, where the JVs are widely spaced. We then find the melting field for each pixel, $H_m = H_m(T, H_{\mathrm{IP}};\ x, y)$ by finding the lowest field where the pixel reaches some threshold value. The result is shown in Fig. 4.7b, which shows the deviation of H_m from the spatial mean melting field $\langle H_m \rangle$. The latter was extracted from H_m by correlating H_m with a 40 by 70 averaging kernel (corresponding to 40×70 $\mu\mathrm{m}^2$). For comparison, Fig. 4.7a shows a field modulated image of PV chains, in external conditions which are close to the transition analyzed in (b). Overlayed on Fig. 4.7b are equally spaced lines parallel to the PV chains in (a) and with approximately the same spacing.

The figure shows that the melting landscape is modulated by the JV lattice with a modulation amplitude of 0.5 ± 0.2 Oe. A similar analysis was performed on the transition

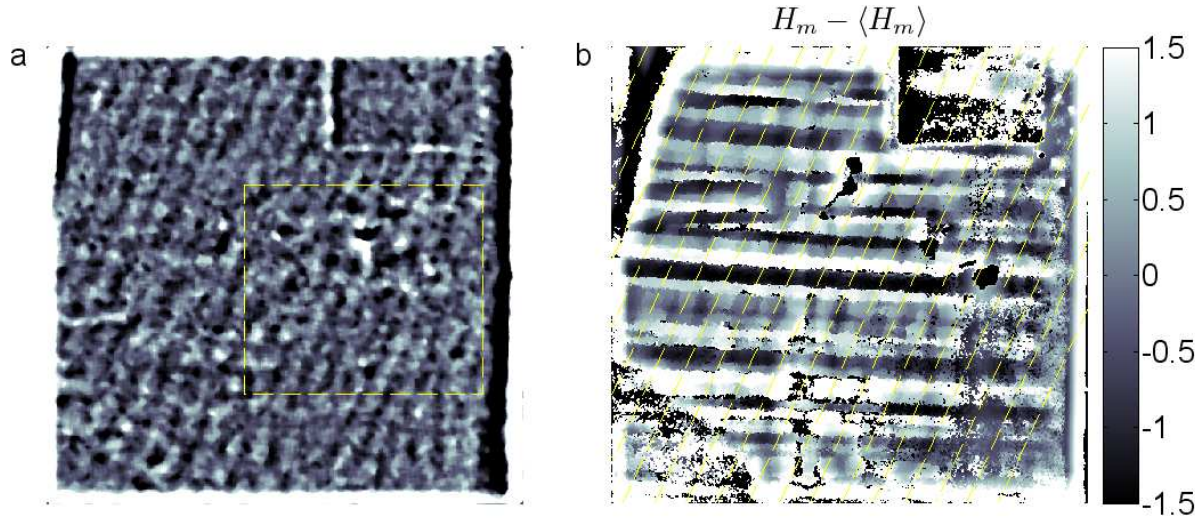

Figure 4.7: *(a) A field modulated image, $dH = 1$ Oe, of the PV chains, $H_z = 6.5$ Oe, $T = 87$ K and $H_{\rm IP} = 5$ Oe, 120°, similar to the conditions of (b) and Fig. 4.6. In order to increase the contrast of the chains, the spatial average of the same image was subtracted from it, where the spatial average was found by correlating the image with a 30 by 30 averaging kernel. The yellow dashed rectangle is the ROI shown in Fig. 4.6. (b) The variation of the melting field from the average melting field, $H_m - \langle H_m \rangle$, at $T = 87$ K and $H_{\rm IP} = 5$ Oe, 120°. The melting field at each pixel, H_m, is deduced from a field scan at constant $H_{\rm IP}$ and T, and is the minimal H_z where the pixel reaches some threshold intensity. The spatially averaged melting field, $\langle H_m \rangle$ is the result of correlating $H_m(x, y)$ with a 40 by 70 averaging kernel (corresponding to 40×70 μm^2). The yellow dashed, equally spaced, lines, are directed along the the PV chains in (a), and have approximately the same spacing. The images are 0.5 mm wide.*

in the temperature scan shown in Fig. 4.3, where it was found that the JV lattice induces a modulation of the melting *temperature* of about 0.1 K. The two results are consistent with the slope of the melting line[2] close to T_c, $\partial H_m / \partial T_m \approx 5$ Oe/K.

4.2.4 Discussion

To summarize, we have seen that the effect of the JVs on the melting landscape is the following. (i) In regions that are homogenous with regard to melting, i.e., should melt at the same T_m and H_m in the absence of $H_{\rm IP}$, the JVs cause a secondary melting corrugation—causing uneven melting. Crossing thin linear defects this has the appearance of droplets that are spaced the same as the JV lattice crossing the defect. However, if the homogenous region is wide enough, segments of melted chains appear, in the direction and periodicity of the JV lattice. (ii) The melting nucleates on the JV stacks rather than between them. (iii) Not only the position of the nucleation centers within every region are aligned with

2 The slope pf the melting field $H_m(T)$, depends on the doping (see e.g. [7]). A slope of $\partial H_m / \partial T_m \approx 5$ Oe/K, is characteristic of optimally doped BSCCO.

the JV lattice but also the nucleation centers in different defects. (iv) The difference in the melting field, at a constant temperature, is about 0.5 Oe. (v) As the melting transition progresses and the melted regions are wide enough, then the effect of the JVs is reduced and the droplet surface tension starts playing a role.

One immediate consequence of our observations is that the JV lattice is not destroyed by the PV lattice (partial-) melting. Otherwise, there is no apparent reason for the PV melting to nucleate along a single JV stack. This result is surprising since there are theoretical studies [51, 110] and strong experimental evidence [12] suggesting that the first-order melting is accompanied by the loss of c-axis correlation. One could argue against our conclusion that perhaps the JV lattice has melted, but the increased PV density on the JV stacks takes a long time to decay and serves as nucleation spots. This can not be the case here, though, since in a typical DMO measurement each image is an average of a large number of images so that the melting images are actually an average of repeated melting and freezing. This effect is also *not* a surface effect, such that the melting observed is only at the top of the sample while the bulk is still solid, since the large signal of the melting we see is due to the fact that the whole thickness of the crystal melts. Our experience shows that if the thickness of the melted regions are less than about 10μm (as in thin samples) then the vortex melting can hardly be discerned with our experimental setup. The large signal from the PV melting indicates that the melting is truly throughout the sample bulk.

A possible solution to this puzzle might be due to pinning. We have seen that when we were ramping the in-plane field up and down the JV lattice would be created, destroyed and then recreated in the same position. This suggests the JV lattice has a stable potential minimum fixing it in one position. This strong fixing potential might also keep the parts of the JV lattice that have not melted in place. It is interesting to note that in some samples (for example the one we have used for the report in Section 4.1), we could not see any trace of the JV lattice melting. In the same (exceptionally clean-) sample we have also observed a pronounced drift of the JV lattice (see e.g. Fig. 3.4) and perhaps the two phenomena are indeed linked.

It is important to note that our measurements were done in the range where each JV core occupies a single row of PVs. The data are taken at low perpendicular fields, where the PV spacing $a_0 = \sqrt{\sqrt{3}\Phi_0/2B_z}$, is larger than JV core, $\lambda_{J0} = \gamma s \approx 500 \times 15$ Å $= 0.75$ μm (the matching field corresponding to λ_{J0}, is $B_{J0} = 2\Phi_0/\sqrt{3\lambda_{J0}^2} = 42.5$ G). As is pointed out in Ref.51 the fact that there is a single row of PVs on each JV stack does not necessarily mean that the vortices are in the chain-and-lattice state. The transition between the chain-and-lattice state and the distorted lattice state takes place when the PV-PV repulsion, in

a lattice, roughly equals to the JV stack binding strength. In the parameter range relevant to our experiment the transition is at roughly 10–20 G. At lower fields we expect the chain and chain-and-lattice states and at higher fields the modulated triangular lattice. The measurements described above were made in the region of this expected crossover and above it.

The fact that the PV melted on the JVs first and that each JV contains a single PV row might lead us to conclude that at the melting transition 1+1 dimensional channels of liquid are formed on the JV lattice. However, the melted liquid has a (very small but-) non zero surface tension [94] so the existence of one dimensional liquid channels that are a single PV-row wide is unlikely.

As we have stated above, there is no clear reason why melting should nucleate on the JV stacks. The PV stacks on the JVs are bound to them and as such should have a stiffer lattice and so should melt at higher temperatures and fields similar to what is observed with PV stacks in the presence of columnar defects [96]. However, this argument does not apply to the PV rows next to the one that is bound to the JV core. The PV lattice right next to the JV stacks suffers from high distortion and is not bound to any caging potential to compensate for that. Thus, it is possible that the lattice mismatch at the two sides of the JVs and the liquid surface tension cause the melting to nucleate in channels that are centered about the JV chains and are a few rows wide.

Another possible explanation is due to the fact that for a given applied field the vortex density is higher on the PV stacks than off them. As we saw with regard to the supersession of the geometrical barrier, this relative density difference can be quite significant, especially at low perpendicular fields (see Sec. 4.1). This approach can be consistent with our results only if the field on the JV stacks is higher then off them by about 0.5 G. However, the melting fields we have studied are of the order of H_{c1} (about 3–5 times the penetration field) and such a large density variation is not plausible. Also, such large field variations are within our magnetic sensitivity (even in DC images) and were not observed.

It is natural to compare the magnitude of the reduction of H_m on the JVs, which is of order $\Delta H_m/|H_{\rm IP}| \approx 0.1$, to the high IP field behavior as shown in Fig.4.1b or in Refs 51, 105, 106, which is more than an order of magnitude smaller. The difference, is consistent with the sharp drop in H_m around low $H_{\rm IP}$ seen in Fig. 4.1b and in Fig. 2 of Ref. 51. One possible explanation for these findings is that there are different vortex states for different field tilt angles [51,56]. Specifically, at very low tilt angles, i.e., at $H_z \gg H_{\rm IP}$, the vortex lattice is in the tilted lattice state whereas above some critical, nonzero but small, tilt angle, the JV lattice is formed. Therefore, if the JV lattice free energy has a

contribution, which is independent of $H_{\rm IP}$, so it does not go to zero at low $H_{\rm IP}$, a sharp change in the melting field should be observed when the JV lattice is formed.

Our results above raise a few theoretical open questions. The main ones are—(a) what is the microscopic nature of the liquid channels and why does melting nucleate on the JVs? (b) What is the nature of the JV lattice after the PV lattice has (partially -) melted? On the experimental side there is also some more work that needs to be done. First, this work should be expanded to check if the effect is observed at higher melting fields (higher than B_{J0}). Second, the effect of the JV has been seen clearly in the two optimally doped sample reported here and some effect was also observed in two other optimally doped samples, where the growth defects were too abundant for a clear JV melting measurement. In two extremely clean and homogenous over-doped samples, the effect was not seen at all. The role of the anisotropy, which depends on doping, and that of defects also needs to be clarified. Finally, one could try and accompany this experiment with a measurement that is sensitive to the JV lattice order, perhaps c-axis transport measurement [12], to try and gain a deeper understanding on the nature of the JV lattice after melting.

4.3 Imaging and Mapping the Phase Diagram of Underdoped BSCCO

4.3.1 Introduction

The interplay of vortex lattice elasticity, inter-layer coupling, quenched disorder and temperature results in the rich phase diagram of $Bi_2Sr_2CaCu_2O_{8+\delta}$, a layered high T_c superconductor, that shows much more than an ordered state at low fields and temperatures and a disordered state otherwise. Using Hall sensor arrays, the discontinuous jump in the vortex density, that is associated with first-order vortex lattice melting, was measured [111]. By employing an AC in-plane field to assist vortex relaxation, the first-order, quenched disorder-induced, order-disorder transition was subsequently measured [14]. The same experimental technique was used some years later to unveil the second-order glass transition that bisects the phase diagram to a low temperature pinned states on one side and depinned states on the high temperature side of the phase diagram [7,18]. Hall bars were also used as sensitive sensors to study supercurrent flow profiles and identify the role of surface barriers in transport and the subsequent characteristics flow regimes [11, 17, 112–114].

Although it has been more than 20 years since the discovery of high-T_c superconductors has boosted the interest in vortex phases, there are still some open puzzles regarding the nature of the vortex phases and phase transitions. Most obscure is the nature of the glass phase transition. This transition is believed to be a transition from a thermally activated amorphous vortex state with Ohmic resistance, to a collectively pinned vortex glass state that is characterized by zero resistance at the limit $j \to 0$. However, a consistent theoretical model that describes the low temperature glass phase and the glass transition is still missing (see e.g. [20, 21, 26, 115]). The experimental results of H. Beidenkopf [7, 18, 19] also lead to some open questions. In [19] the distinction between the glass transition and depinning was made by the simultaneous study of the sample induction $B(H,T)$ and the self field response to transport current $B_{SF}(j(\omega); H, T)$. It was found that the depinning line is frequency dependent and approaches the glass line only at the limit $\omega \to 0$. The thermodynamic glass transition was seen as a kink in the magnetic induction $B(H,T)$, a discontinuous decrease in dB/dT, as the temperature is raised through the transition. However, due to the temperature dependance of the Hall sensors themselves it was not clear what the actual values of dB/dT were, and only the discontinuity was asserted. The origin of the kink and the dependencies of the induction on the temperature at the different phases, as well as the distinction between the transition at the high field disordered phases and the transition at the low field, phases are still

a puzzle.

In order to obtain a more complete picture of the low temperature phases and phase transitions, we study them below using magneto-optics. Although it is somewhat less sensitive, differential magneto-optics has an important advantage compared to Hall sensor arrays— it provides spatial information on disorder and correlations. This information can be used to identify the length scales and defects that are important in the phase transitions. Apart from adding information about the nature of the phase transition, the pattern of highlighted defects and its propagation across the sample can be used to identify the transition and phases, where the signal to noise ratio is poor. Using this experimental setup, spectacular movies of the propagation of melting in BSCCO were taken [94], and the typical defects were identified and characterized [95]. It was found that the disordered liquid has a very low surface tension, which allows for nucleation of small liquid droplets and long and narrow liquid channels. The subsequent melting landscape is thus governed by growth defects that induce variability of material content and doping resulting in local variability of T_c and of the slope of the melting line in the $B-T$ diagram.

In this work we study the phase diagram of underdoped BSCCO (ud-BSCCO) using the DMO setup. ud-BSCCO samples are characterized by relatively low maximal melting fields, which are accessible to our DMO setup. Subsequently, we could image for the first time the inverse melting and the second-order glass transition. We have found that the typical length scales and characteristic defects of these transitions are very different from those that govern the melting transition. We were also able to methodically map the magnetic induction, B, within the H-T phase diagram and have found that while $B(T)$ does not change appreciably at the first-order transitions, the change at the glass transition is dramatic and is the main feature that governs the phase diagram.

4.3.2 Experimental Details

In a typical DMO measurement we modulate the field or temperature for $N = 10$ times and acquire simultaneously the "DC" $B_z(x, y)$ and the differential $\Delta B(x, y)$ upon sweeping H or T. The inversion of the intensity to induction is done according to the calibration procedure described in Section 3.1. In order to probe the equilibrium magnetization we employ the shaking method in which an additional AC in-plane field H_x is applied in order to suppress the hysteresis and equilibrate the lattice at low temperatures [14]. The shaking is effective at relatively low frequencies, 8–15 Hz, and at amplitudes and durations that need to be increased with decreasing temperature. In order to equilibrate the sample at $T \lesssim 20$ K we shake at an amplitude of 500 Oe (the maximal amplitude reachable with

our 3 axis magnet and power supplies[3]) for about 50 periods (e.g. 5 seconds at 10 Hz). Since the image exposure time and shaking period are comparable, shaking is turned off prior to image grabs and then turned on again after the modulated field (or temperature) is changed. In this way, a single field modulated DMO image takes about 5 minutes to acquire, and temperature modulated images take 10 minutes to acquire.

We have studied three ud-BSCCO samples, grown by T. Sasagawa of the Tokyo Institute of Technology, sample TKUD70 of dimensions 1 mm × 1 mm × 30 μm that has $T_c \approx 70$ K, sample TKUD73 with $T_c \approx 73$ K and dimensions 1.1 mm × 0.9 mm × 45 μm and sample SagH76, which has $T_c \approx 76$ K, dimensions 1 mm × 1.5 mm and has a terrace of width 0.5 mm by 40 μm with a lower mesa, which is also about 0.5 mm wide but has half the thickness. Some of the features we have measured varied from sample to sample and this variation can be in-part attributed to a strong stray in-plane field due to wrong execution of the shaking procedure. The data described below are either common to all three samples or common to the data shown in Refs 7, 18 and are taken from TKUD70 unless otherwise specified.

4.3.3 Results

Fig. 4.8 shows $B(T)$ averaged over the region of interest (ROI) marked by a red rectangle in Fig. 4.11 at three values of H_z. The three curves in Fig. 4.8 correspond to $H_z > \max(H_m)$, $H_z \lesssim \max(H_m)$, and $H_z < \max(H_m)$, where $\max(H_m) \approx 115$ Oe is the maximal melting field in this sample (see Fig. 4.10). In all three subfigures we observe a rise in $B(T)$ at low temperatures and the change in slope (cusp) at the maximum (marked by cyan triangles in the figure), indicating a second order transition. The shape of this cusp and its position in the $B-T$ phase diagram are very similar to the glass line reported in Refs 7, 18 and

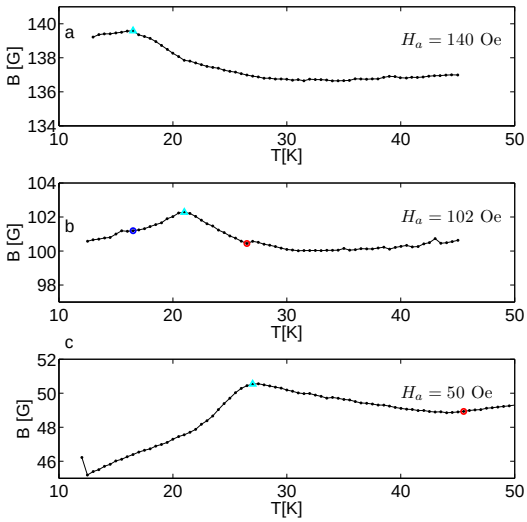

Figure 4.8: *Three typical $B(T)$ at fixed applied fields. The cusp at the glass line is marked by a cyan triangle and the circles mark the position of first-order transitions seen in Fig. 4.9.*

3 We shake at an amplitude that is higher than the maximum field per axis by shaking at both IP directions simultaneously.

so we refer to it as such hereafter. In Fig. 4.8b, we also observe the inverse melting first order transition (FOT), which is marked by a blue circle and the melting FOT (red circle) at a higher T. In Fig. 4.8c, taken at $H_z < \max(Hm)$, the FOT melting is only vaguely seen.

The glass line and FOT's are more apparent in the $\Delta B(H, T, x, y)$ curves, Fig. 4.9, obtained from the differential images. In DMO with T modulation FOT's should appear as positive (melting) or negative (inverse melting) peaks and a second-order transition should appear as a step. In Fig. 4.9 the glass line is seen as a step where ΔB changes sign and whose center is roughly marked by the cyan triangles, which are the locations of the cusps in Fig. 4.8. At low fields (Fig. 4.8b and c) the second-order transition is preceded by a sharp rise, which as we show below is not discontinuous, and whose origin we do not know. The peaks corresponding to the FOT's are marked by circles. The melting transition is seen as a high peak (red circle in Fig. 4.8b and c) and the inverse melting transition seen in Fig. 4.8b as a relatively sharp minimum (blue marker). Identifying the transitions in this way is difficult due to the poor signal to noise ratio. The full images however, greatly assist in doing so as we show below. One notes that the first-order transition markers that are derived from the differential data fit discontinuities in the "DC" B signal and similarly the kink extracted from the B curves fits a node in the differential curves. These two measurements have different characteristic time constants— the differential images are exposed for roughly 5 seconds after an in-plane vortex shake of about 10 seconds leading to a time constant of about 15 seconds. The DC signal is integrated along the several such periods (usually 10) and it has a charac-

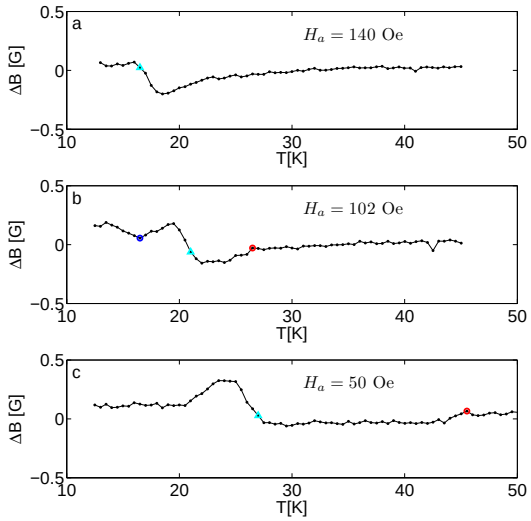

Figure 4.9: *Three typical $\Delta B(T)$ at fixed applied fields ($2dT = 0.5$ K). (a) At $H_z > \max(H_m) \approx 115$ K, there is no first-order phase transition line crossed. (b) At $H_z \lesssim \max(H_m)$, both the inverse melting and melting lines are crossed (blue and red circles respectively), and at $H_z < \max(H_m)$ only the melting line is crossed. The cyan triangle corresponds to the position of the cusp in Fig. 4.8 and roughly agrees with a node in the $\Delta B(T)$ curves. In all three plots the signal that is plotted is the difference of the average differential signals in a ROI inside and outside (and far from) the sample.*

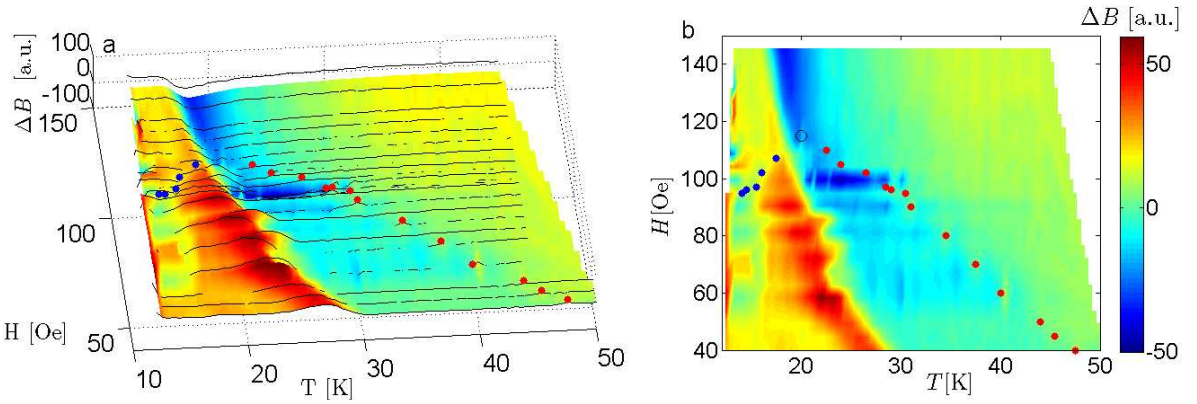

Figure 4.10: *(a) A phase map for the studied superconductor constructed from about twenty $\Delta B(T)$ curves at fixed applied fields like the ones shown in Fig. 4.9. Overlayed are the melting transition (red) and inverse melting transition (blue) within the ROI shown in Fig. 4.11) while the black circle is an estimate for the maximum melting field based on other measurements. (b) A diffrent view of the same data.*

teristic time constant of 5-10 minutes. The fact that the two data sources are consistent strengthens our conviction that the system is indeed in equilibrium.

Figure 4.10 shows a collection of such differential curves put together in a 3D plot. Overlayed on top of the data, are markers pointing to the melting and inverse melting transition points, as extracted from the full DMO images, as seen for example in Fig. 4.11. It is clear that the glass transition and the peak preceding it are the dominant features in this phase diagram. The fact that the diagram, which was taken by putting together increasing and decreasing temperature scans, each about twelve hours long, is continuous and shows almost no hysteretic effects, indicates that the system is in equilibrium.

The DMO technique allows us to visualize where on the sample phase transitions occur. As can be seen in Fig. 4.11, each one of the three transitions has a very distinctive shape which results from the fact that the different transitions are affected by different kinds of disorder in the superconductor and that the phase transitions are of a different order. Full movies at similar conditions comparing the temperature scans at different applied fields can be found on our webpage [109]. The top row shows three characteristic, temperature-modulated, differential images ($2dT = 0.5$ K) of the melting transition. The melting front is seen as bright areas against the dark background of the sample bulk, due to the discontinuous jump in vortex density at the transition. As can be seen in these images, the melting nucleates on growth defects (long, vertical, arc shaped defects), that have slightly different material content and hence different T_c and $B_m(T)$ dependence [95]. The low surface tension of the disordered phase allows for a nucleation of very small droplets and long and narrow melting puddles on the defects. The disorder-induced

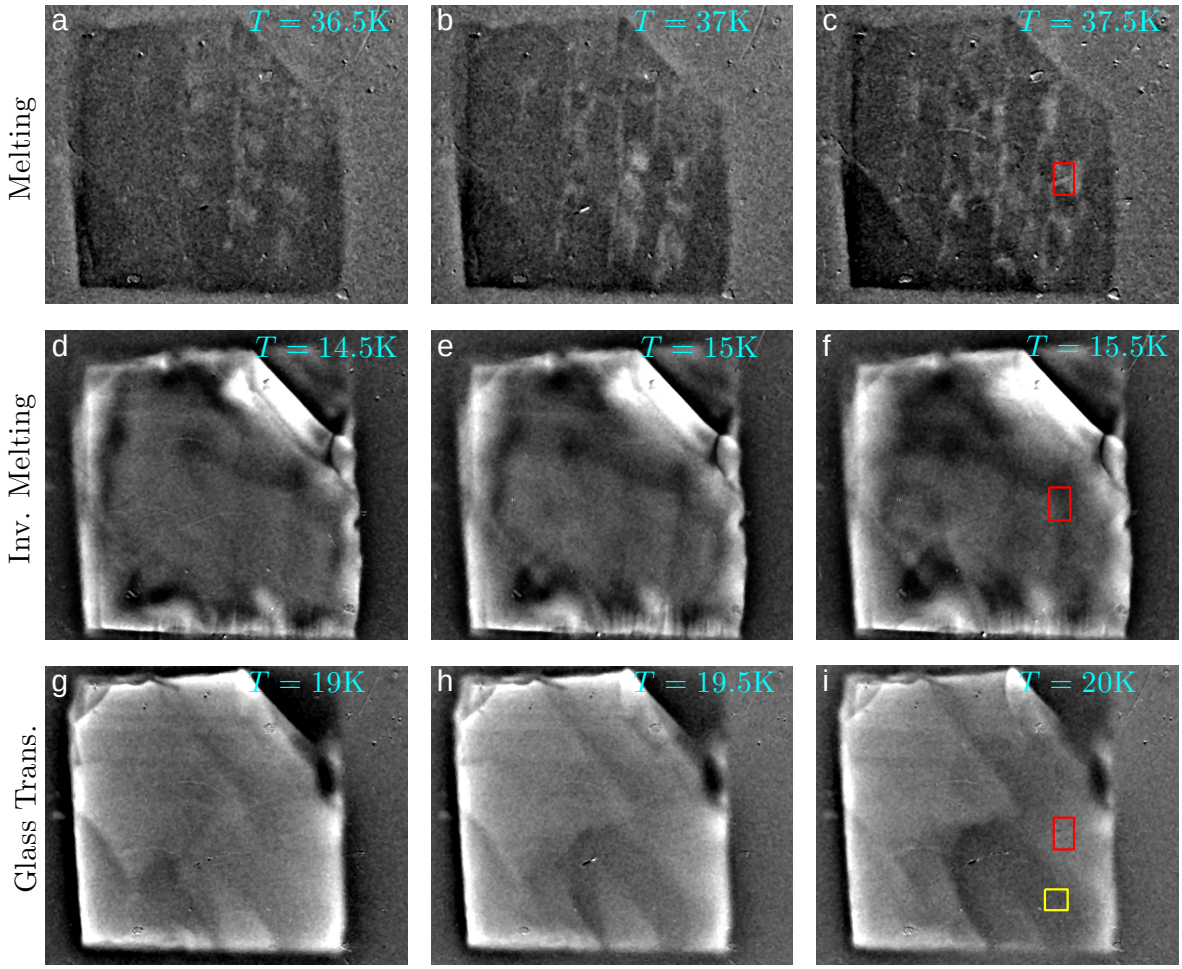

Figure 4.11: *Three characteristic images of each of the three phase transitions. Images a–c show the melting transition where the melting front is seen bright against the dark background of the sample bulk. Images d–f show the inverse melting transition whose transition front is dark and roughly follows the sample perimeter and images g–i show the glass transition where front propagation is not seen at all. All images are temperature modulated differential images with* $2dT = 0.5$ K. *Images a–c were taken at* $H = 70$ Oe, *images d–f at* $H = 106$ Oe, *and images g–i at* $H = 96$ Oe. *The sample is square shaped and partially cleaved at its top right corner. The red rectangle in images c,f and i is the ROI used for figures 4.8 and 4.9, while the yellow rectangle in image i is the ROI used for Fig. 4.12. Full movies of temperature scans at different applied fields can be found on our webpage [109].*

transition, the 'inverse melting' (middle row), is markedly different. Its transition front is dark (the denser phase is the low temperature phase) and approximately follows the sample perimeter. As the temperature is increased it contracts until it closes roughly around the sample center.

At the glass transition (bottom row of Fig. 4.11), we do not see the transition front propagation whatsoever. As seen for example in the bottom right area of figures 4.11g–i,

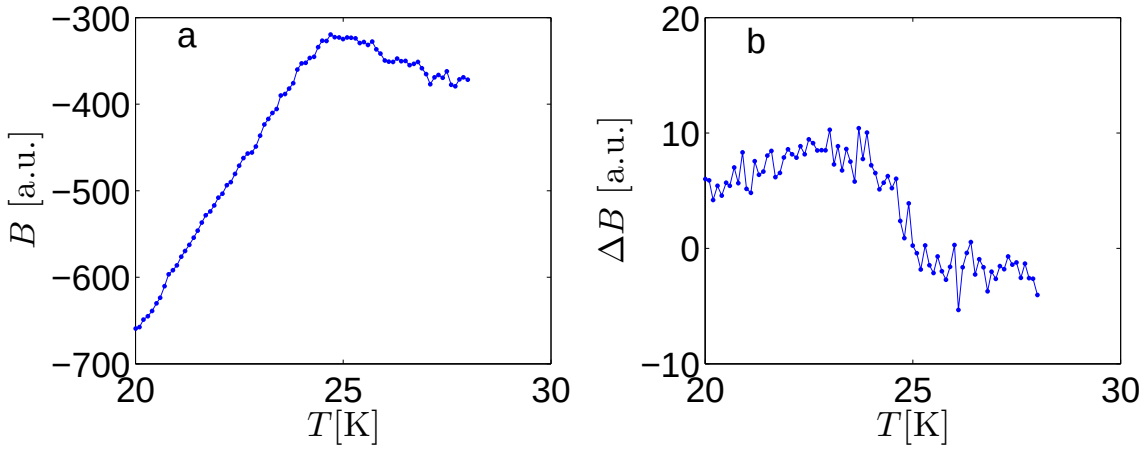

Figure 4.12: *The intensity (a) and differential signal (b) in the yellow rectangle in Fig. 4.11i about the glass transition. The data points are taken at 0.1K intervals, the temperature modulation is* $2dT = 0.1$K*, and the applied field is* $H = 62$ Oe.

instead we see large areas in the crystal which change contrast as a whole (going from positive dB/dT to negative as the temperature increases). The straight perimeter of these areas suggests that these are probably homogenous crystallites which compose the large superconductor. Since second-order transitions have zero latent heat the coexistence of two phases is not possible. Thus the fact that there is no coexistence of the two phases within one crystallite supports the evidence that this transition is of second-order. Further evidence for this claim can be seen in Fig. 4.12, which shows B and ΔB as averaged in a small ROI (yellow rectangle in Fig. 4.11) about the T_g line. The figure shows a clear cusp in the B signal and a discontinuity in the ΔB signal. Unlike the data shown in Fig. 4.9, where the glass transition looks like a peak in ΔB, implying perhaps a first-order transition, here we take considerably smaller T steps (0.1K) and a small modulation amplitude ($2dT = 0.1$K) and see only the second-order type non-analyticity.

The propagation of the inverse melting transition can also be seen in Fig. 4.13, which shows field modulated DMO images of a field sweep. The image sequence shows the inverse melting as it nucleates in a wide bright ring (Fig. 4.13a) that expands until it almost reaches the sample perimeter at Fig. 4.13f. Note that in the field modulated images, the inverse melting front is bright similar to the regular melting front (in both cases the denser phase is the high field disordered phase). The image sequence in Fig. 4.13 is taken at $T \lesssim T^\star$, where $H_m(T^\star) = \max(H_m)$, i.e. at a temperature slightly lower than the temperature where the melting field is maximal. In this sequence, one can study the crossover from melting to the inverse melting in light of the different patterns characteristic of them (see inset of Fig. 4.13f). We find that as the field is increased,

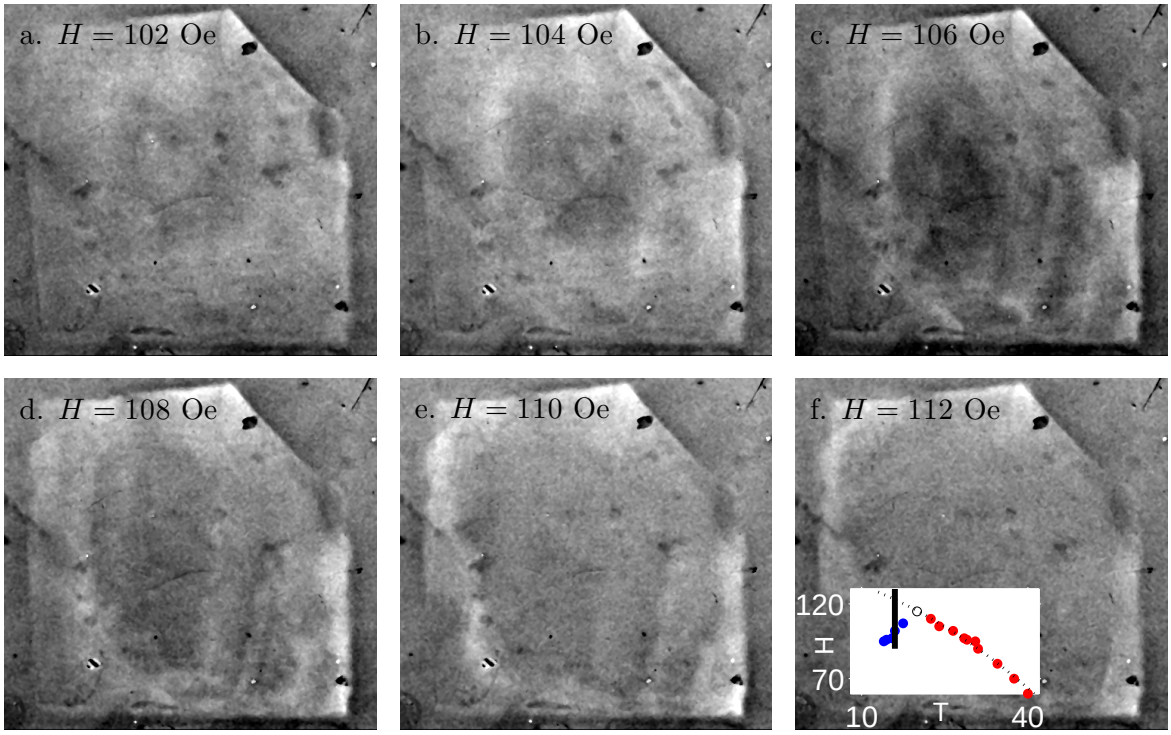

Figure 4.13: *Field modulated, calibrated, differential images ($dH = 2$ Oe) of the melting front propagation at field sweep at $T = 18$ K. The melting front is the blurred bright ring in (a) that becomes sharper as it expands towards the edges as the field is swept up. Inset: The schematic description of the parameter range for this data. The same phase diagram as shown in Fig.4.10. A field sweep slightly below the crossover temperature (black thick line), can cross the 'inverse melting' line and the extrapolated continuation of the melting line.*

the inverse melting front first nucleates at the sample center and expands from there towards the edges (bright ring that expands from Fig. 4.13a to Fig. 4.13f). Inside the expanding ring we see bright patterns that appear to have the same characteristic arcs as the regular melting. Although it is unclear from the experimental data, it seems that perhaps these arcs go through inverse melting and then through melting at higher fields. This finding suggests that perhaps the melting line continues to higher fields past $\max(H_m)$ (black open circle in the inset of Fig. 4.13f) and that the 'inverse melting' line meets it in a tricritical point. Although this suggestion is a-priori plausible (this is the situation, for example, in YBCO [116]), it is in contrast with previous experimental results [14, 15]. A more consistent explanation would be that the growth defects have a different crossover temperature creating islands in the sample that melt to liquid while most of the sample experiences inverse melting. When comparing several such field scans

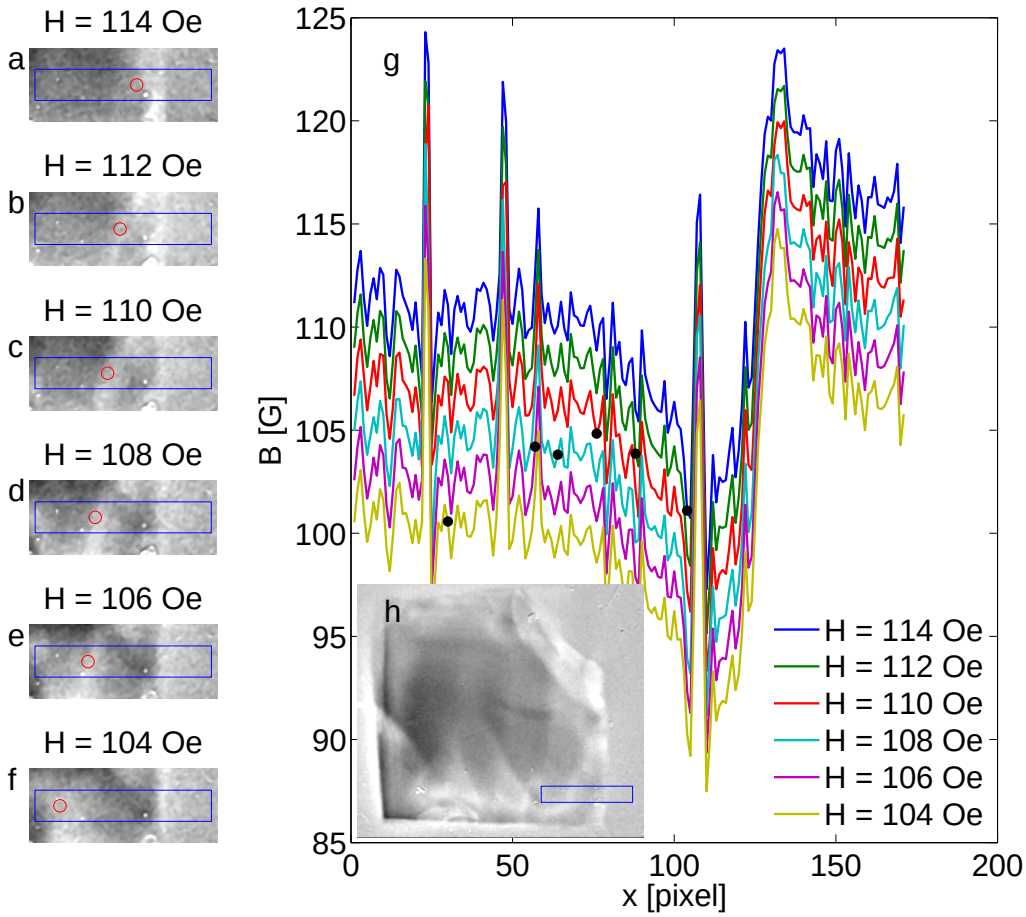

Figure 4.14: *Field modulated, calibrated, differential images ($dH = 2$ Oe) of the melting front propagation for a field sweep at $T = 16$ K. Figures (a)–(f) show a zoomed in view of the ROI shown in (h). The melting front, which is bright and marked by a red circle is clearly moving away from the edge (bright vertical line) towards the center as the field is swept down from $H = 114$ Oe to $H = 104$ Oe. (g) The magnetic induction profiles $B(x; T, H)$ in the blue ROI corresponding to differential images (a)–(f). The induction is averaged along the narrow edge of the ROI. The black full circles mark the same x positions that show the melting front at (a)–(f) (red circles). All markers have the same B, $B = 104 \pm 2$ G, except the $H = 104$ Oe curve which does not cross this value and indeed shows no clear melting front within the ROI. (h) The full differential image and ROI at $H = 108$ Oe.*

at different temperatures around the crossover region (not shown) we see that the melting signal gets dimmer as the temperature is reduced and only the arc defects remain relatively bright. In parallel the expanding ring signal of the inverse melting gets stronger until at low enough temperatures it is the only first-order signal we see.

The propagation of the transition seen in Fig. 4.13 or in the second row of Fig. 4.11, inwards and roughly in parallel with the sample perimeter, can be explained by considering the dome shaped induction profile of the sample. Alternatively, a signal similar to this might be due to a mechanism similar to the Bean model for pinning where the sample

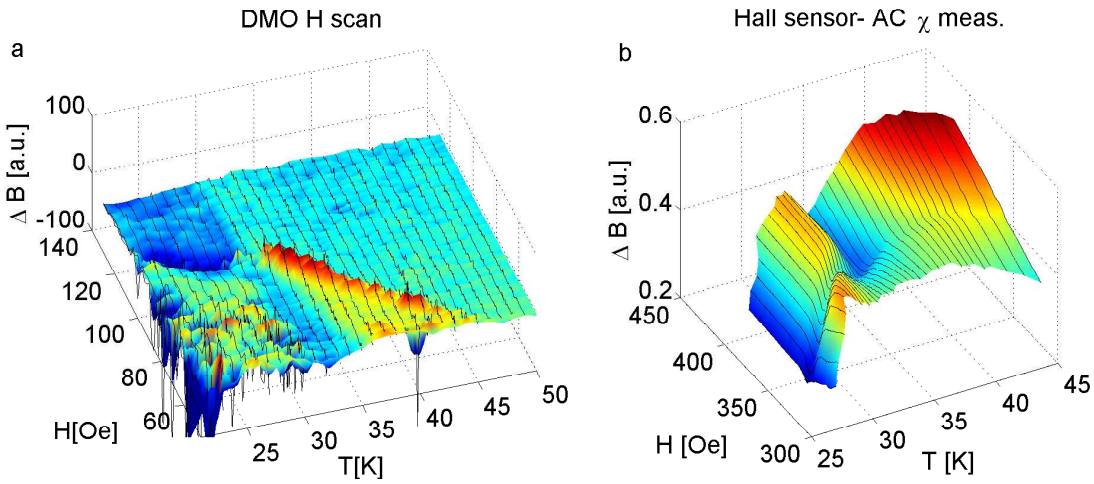

Figure 4.15: *(a) An H scan of TKUD73. Melting is seen as red peaks at low fields and high temperatures, whereas the glass transition is seen as the valley at low fields around $T = 32$ K. At temperatures below the latter transition, melting is accompanied with a pronounced minimum, although the melting peaks are seen there as well (green and light blue peaks going into the dark blue valley).(b) An AC susceptibility Hall measurement of optimally doped BSCCO reconstructed by the data gathered by H. Beidenkopf [19].*

center is in a meta-stable pinned state and temperature and field modulation effect only regions of some width around the sample bulk that are in equilibrium [66, 117, 118]. In order to verify that indeed we are seeing an equilibrium transition that propagates due to the $B(x, y)$ profile we have followed the transition at a constant temperature, sweeping the applied field and have verified that the induction $B(x, y)$ at the melting front is the same for all applied fields. This is shown in Fig. 4.14. The figure shows zoomed in views of some small region in a DMO image of the sample at various applied fields around the inverse melting transition (the whole sample is shown in Fig. 4.14h). The circle overlayed on the images marks the melting front, which is bright since these are field modulated images. Fig. 4.14g shows the DC induction profiles, $B(x)$, at the corresponding applied fields (averaged along the width of the narrow ROI). The noise in these curves is typical to DC MO images and is about two orders of magnitude higher than the noise in the differential images. The full black circles in (g), mark the positions of the melting front, which were take from the differential images. It is seen that all black circles but the $H = 104$ Oe circle are within $B = 104 \pm 2$ G. The lowermost curve is completely below the transition and does not show a clear melting front. This also explains why the inverse melting front gets narrower and better defined close to the edges— at the center B is almost constant resulting in a wide and undefined melting front.

Another feature that is interesting in Fig. 4.13 is that inside the inverse melting ring the sample appears dark implying a low permeability, dB/dH (see Fig. 4.13c). We

note that this behavior is quite repetitive and a minimum of the permeability is seen in these ud-BSCCO sample as well as in the data taken from optimally doped BSCCO by H. Beidenkopf [19]. This is shown in Fig. 4.15, which shows $\Delta B = (dB/dH)\Delta H$, acquired from field modulated DMO imaging of TKUD73 (a) and the AC susceptibility of an optimally doped BSCCO sample measured by Hall sensors (b). In (a) the melting appears as bright peaks and the glass line as a vertical line at $T \approx 32$ K, where the permeability changes sharply— changes from blue to green at high fields and from yellow to blue at low fields. In Fig. 4.15b, the melting appears as step-like increase in ΔB_{ac}, while the glass line appears as a narrow dip at $T \approx 35$ K. In both figures the melting at temperatures lower than the glass transition in accompanied by a valley in the ΔB signal. In (a) one can identify the melting peaks within this minimum (green and light blue peaks in the dark blue background). It is possible that this valley is a dynamic manifestation of the second magnetization peak. If the strong shaking field has a substantial out-of-plane component (due to sample-magnet misalignment) then the sample is not in equilibrium. Out of equilibrium, the inverse melting is accompanied by a sharp peak in magnetization (a pronounced minimum in dB/dH for increasing fields, and a maximum for decreasing field) due to enhanced pinning, which is known as second magnetization peak [15,32,119], and can explain this result.

4.3.4 Discussion

Our results above raise a few questions whose answers may provide some insight into the nature of the BSCCO equilibrium phases. The first and most surprising result we have found is the dependence of B on the temperature at a constant applied field. We find that as the temperature is increased ,the induction increases, reaches a maximum, drops sharply and then starts curving upward slowly. Furthermore, in the Bragg Glass, low field phase, the maximum is preceded by a sharp rise in B at $T/T_c \approx 0.3$ independent of the applied field. Naively, in the absence of pinning, B is expected to slightly increase with temperature due to the decreased vortex interaction (increase in the penetration length $\lambda(T)$), and this is indeed what we see at high temperatures. The vortex density also increases if the inter-vortex repulsion becomes small compared to the pinning to disorder. In this case, the energetic cost of having vortices in the SC is reduced since vortex mean energy is reduced by pinning to disorder. This is the case at low temperatures. Thus, in the region of thermally assisted depinning, one expects a decrease of B as the temperature increases. This can, perhaps, explain the decrease in B on the high temperature side of the glass transition. However, the increase in the induction on the low temperature side

of the transition and the subsequent maximum at the transition are a puzzle.

The extreme visual difference between the three transitions naturally raises the question of the source of this difference. The thermally and disorder-induced transitions are both first-order transitions. Yet, the thermally-induced melting is very susceptible to local stoichiometric defects and the disordered liquid phase shows vanishingly small surface tension while the inverse melting shows one large melted puddle suggesting that the vortex glass is characterized by a very large surface tension. The inverse melting front also follows the surface currents and is indifferent to the sample growth defects. At a second-order transition, the two phases cannot coexist, and it is not surprising that we see what seems to be crystallites that go through the transition as a whole. The surprising thing is that these crystallites have no signature in any other part of the phase diagram and they are only seen close to the glass transition. One would expect that if these are indeed crystallites, then along their borders we will see increased flux penetration (as seen in the defects described in 4.1), higher flux concentration and melting nucleation, none of which are observed. The nature of these defects is therefore, unclear.

5. Concluding Discussion

The aluminum based scanning SOT microscope is set up and used to image single vortices. Now that it is working and its operating procedures defined, it is on the brink of acquiring data and hopefully will do so soon. Using the lessons learned from the Al prototype, a new microscope based on the lead SOTs is currently being built. With the Pb SOT high sensitivity and high critical temperature (at least compared with Al), this microscope is expected to be able to resolve single vortices over a wide fraction of the vortex lattice phase space and also reach out to other nanomagnetic phenomena.

In a separate project, Josephson vortices were indirectly imaged using the magneto-optical microscope over a broad range of applied magnetic fields. The high visibility allows the study of the effect of Josephson vortices on the pancake vortex lattice. Specifically, we have studied the effect of the JV lattice on the magnetic hysteresis and melting. In both cases we have shown that the JV lattice *locally* alters the bulk properties. In the case of melting the JV lattice locally reduces the lattice melting temperature and field, creating segments of melted quasi one-dimensional liquid channels. With regard to the magnetic hysteresis, we have shown that the JVs locally reduce the edge geometrical potential barrier, and provide channels for PVs entering and exiting the sample, with an overall effect of reducing the geometrical barrier induced magnetic hysteresis. The latter is an example to how the ability to image single vortices, Josephson vortices in this case, allows solving long standing puzzles that were brought up by experiments of low spatial resolution. Another possible study of a similar spirit is the study of the effect of Josephson vortices on vortex penetration. Our preliminary results (Fig. 3.5) show that there might be a spontaneous formation of JVs due to the buckling bent vortices entering the sample.

The DMO setup was also used in order to map the phase diagram of underdoped BSCCO. The systematic mapping of the magnetic induction across the $H-T$ phase space, showed that the induction changes drastically around the glass transition with an effect far more dramatic than that of the first-order thermally-induced and disorder-induced transitions. The ability to image the sample, simultaneously with the mapping, allows to identify a unique pattern for each transition, which results from the fact that

each of the transitions is susceptible to different material defects and propagates differently. This, in turn, demonstrates the different nature of the transitions, which have different typical length scales, different dominating defects and different transition front propagation dynamics.

6. List of Publications

Y. Segev, I. Gutman, S. Goldberg, Y. Myasoedov, E. Zeldov, E. H. Brandt, G. P. Mikitik, T. Katagiri, and T. Sasagawa, Suppression of geometrical barrier in $Bi_2Sr_2CaCu_2O_{8+\delta}$ crystals by Josephson vortex stacks, *submitted to Phys Rev B.*

A. Finkler, Y. Segev, Y. Myasoedov, M. Rappaport, L. Ne'eman, D. Vasyukov, E. Zeldov, M. E. Huber, J. Martin, A. and Yacoby, Self aligned nanoscale SQUID on a tip, *Nano Letters* **10**, 1046 (2010).

I. Gutman, S. Goldberg, Y. Segev, Y. Myasoedov, E. Zeldov, and T. Tamegai, Experimental evidence for vortex equilibration by an in-plane dc field in $Bi_2Sr_2CaCu_2O_8$, *Physica C: Superconductivity* **470**, S239 (2010).

S. Goldberg, Y. Segev, Y. Myasoedov, I. Gutman, N. Avraham, M. Rappaport, E. Zeldov, T. Tamegai, C. W. Hicks, and K. A. Moler, Mott insulator phases and first-order melting in $Bi_2Sr_2CaCu_2O_{8+\delta}$ crystals with periodic surface holes, *Phys. Rev. B* **79**, 064523 (2009).

This thesis summarizes my independent efforts.

The SQUID on Tip project has been conducted in an equal collaboration with Amit Finkler, whose work emphasis was given to the aluminum SOT sensor making, whereas my work was directed at tuning fork topography sensing and the microscope system design. The measurements of the aluminum SOT characteristics and the vortex images are his. The Pb SOT project was led by me up to the point where I had to give up this project and work on the MO setup. The working Pb tips that are shown here were made Denis Vasyukov, using the system Amit and Myself have built for this purpose. The SSAA cold amplifiers and their electronics were given to us by our collaborator Martin Huber who was also consulted with regard to all issues related to SQUID electronics.

The DMO microscopy experimental setup that has been used in our lab for the past decade, and was introduced to me by Sarah Goldberg. The project that studies the GB reduction by the JVs was initiated by Ilia Gutman. However, the measurements shown and their analysis were all done by myself. The theoretical discussion that relates to this project is the outcome of our collaboration with E. H. Brandt and G. P. Mikitik who have also wrote the numerical simulations. The samples that are described here were all made our collaborators, T. Sasagawa T. Katagiri and T. Tamegai.

References

[1] Finkler, A., Segev, Y., Myasoedov, Y., Rappaport, M. L., Ne'eman, L., Vasyukov, D., Zeldov, E., Huber, M. E., Martin, J., and Yacoby, A. *Nano Letters* **10**, 1046 (2010).

[2] Abrikosov, A. A. *Sov. Phys. JETP* **5**, 1174 (1957).

[3] Larkin, A. I. *Sov. Phys. JETP* **31**, 784 (1970).

[4] Giamarchi, T. and Le Doussal, P. *Phys. Rev. Lett.* **72**, 1530 (1994).

[5] Giamarchi, T. and Le Doussal, P. *Phys. Rev. B* **52**, 1242 (1995).

[6] Kierfeld, J., Nattermann, T., and Hwa, T. *Phys. Rev. B* **55**, 626 (1997).

[7] Beidenkopf, H., Avraham, N., Myasoedov, Y., Shtrikman, H., Zeldov, E., Rosenstein, B., Brandt, E. H., and Tamegai, T. *Phys. Rev. Lett.* **95**, 257004 (2005).

[8] Clem, J. R. *Phys. Rev. B* **43**, 7837 (1991).

[9] Blatter, G., Feigel'man, M. V., Geshkenbein, V. B., Larkin, A. I., and Vinokur, V. M. *Rev. Mod. Phys.* **66**, 1125 (1994).

[10] Huse, D. A., Fisher, M. P. A., and Fisher, D. S. *Nature* **358**, 553 (1992).

[11] Fuchs, D. T., Zeldov, E., Rappaport, M., Tamegai, T., Ooi, S., and Shtrikman, H. *Nature* **391**, 373 (1998).

[12] Fuchs, D. T., Doyle, R. A., Zeldov, E., Majer, D., Seow, W. S., Drost, R. J., Tamegai, T., Ooi, S., Konczykowski, M., and Kes, P. H. *Phys. Rev. B* **55**, R6156 (1997).

[13] Mikitik, G. P. and Brandt, E. H. *Phys. Rev. B* **64**, 184514 (2001).

[14] Avraham, N., Khaykovich, B., Myasoedov, Y., Rappaport, M., Shtrikman, H., Feldman, D. E., Tamegai, T., Kes, P. H., Li, M., Konczykowski, M., van der Beek, K., and Zeldov, E. *Nature* **411**, 451 (2001).

[15] Khaykovich, B., Zeldov, E., Majer, D., Li, T. W., Kes, P. H., and Konczykowski, M. *Phys. Rev. Lett.* **76**, 2555 (1996).

[16] Khaykovich, B., Konczykowski, M., Zeldov, E., Doyle, R. A., Majer, D., Kes, P. H., and Li, T. W. *Phys. Rev. B* **56**, R517 (1997).

[17] Fuchs, D. T., Zeldov, E., Tamegai, T., Ooi, S., Rappaport, M., and Shtrikman, H. *Phys. Rev. Lett.* **80**, 4971 (1998).

[18] Beidenkopf, H., Verdene, T., Myasoedov, Y., Shtrikman, H., Zeldov, E., Rosenstein, B., Li, D., and Tamegai, T. *Phys. Rev. Lett.* **98**, 167004 (2007).

[19] Beidenkopf, H. *Thermodynamics and Dynamics of the Second-order Vortex Glass Transition in* $Bi_2Sr_2CaCu_2O_8$. PhD thesis, Weizmann Institute of Science, Rehovot, Israel (2009).

[20] Fisher, M. P. A. *Phys. Rev. Lett.* **62**, 1415 (1989).

[21] Fisher, D. S., Fisher, M. P. A., and Huse, D. A. *Phys. Rev. B* **43**, 130 (1991).

[22] Koch, R. H., Foglietti, V., Gallagher, W. J., Koren, G., Gupta, A., and Fisher, M. P. A. *Phys. Rev. Lett.* **63**, 1511 (1989).

[23] Koch, R. H., Foglietti, V., and Fisher, M. P. A. *Phys. Rev. Lett.* **64**, 2586 (1990).

[24] Gammel, P. L., Schneemeyer, L. F., and Bishop, D. J. *Phys. Rev. Lett.* **66**, 953 (1991).

[25] Jiang, W., Yeh, N.-C., Tombrello, T. A., Rice, A. P., and Holtzberg, F. *Journal of Physics: Condensed Matter* **9**, 8085 (1997).

[26] Reichhardt, C., van Otterlo, A., and Zimányi, G. T. *Phys. Rev. Lett.* **84**, 1994 (2000).

[27] Olson, C. J., Reichhardt, C., and Nori, F. *Phys. Rev. B* **56**, 6175 (1997).

[28] Fangohr, H., Cox, S. J., and de Groot, P. A. J. *Phys. Rev. B* **64**, 064505 (2001).

[29] Tonomura, A., Kasai, H., Kamimura, O., Matsuda, T., Harada, K., Shimoyama, J., Kishio, K., and Kitazawa, K. *Nature* **397**, 308 (1999).

[30] Moon, K., Scalettar, R. T., and Zimányi, G. T. *Phys. Rev. Lett.* **77**, 2778 (1996).

[31] Thorel, P., Kahn, R., Simon, Y., and Cribier, D. *Journal De Physique* **34**, 447 (1973).

[32] Bhattacharya, S. and Higgins, M. J. *Phys. Rev. Lett.* **70**, 2617 (1993).

[33] Koshelev, A. E. and Vinokur, V. M. *Phys. Rev. Lett.* **73**, 3580 (1994).

[34] Hellerqvist, M. C., Ephron, D., White, W. R., Beasley, M. R., and Kapitulnik, A. *Physical Review Letters* **77**, 4482 (1996).

[35] Xiao, Z. L., Andrei, E. Y., Shuk, P., and Greenblatt, M. *Phys. Rev. Lett.* **85**, 3265 (2000).

[36] Geers, J. M. E., Attanasio, C., Hesselberth, M. B. S., Aarts, J., and Kes, P. H. *Phys. Rev. B* **63**, 094511 (2001).

[37] Giamarchi, T. and Le Doussal, P. *Phys. Rev. Lett.* **76**, 3408 (1996).

[38] Le Doussal, P. and Giamarchi, T. *Phys. Rev. B* **57**, 11356 (1998).

[39] Olson, C. J., Reichhardt, C., and Nori, F. *Phys. Rev. Lett.* **81**, 3757 (1998).

[40] Chandran, M., Scalettar, R. T., and Zimanyi, G. T. *Physical Review B (Condensed Matter and Materials Physics)* **67**, 052507 (2003).

[41] Charalambous, D., Kealey, P. G., Forgan, E. M., Riseman, T. M., Long, M. W., Goupil, C., Khasanov, R., Fort, D., King, P. J. C., Lee, S. L., and Ogrin, F. *Phys. Rev. B* **66**, 054506 (2002).

[42] Marchevsky, M., Aarts, J., Kes, P. H., and Indenbom, M. V. *Phys. Rev. Lett.* **78**, 531 (1997).

[43] Pardo, F., de la Cruz, F., Gammel, P. L., Bucher, E., and Bishop, D. J. *Nature* **396**, 348 (1998).

[44] Togawa, Y., Abiru, R., Iwaya, K., Kitano, H., and Maeda, A. *Phys. Rev. Lett.* **85**, 3716 (2000).

[45] Bullard, T. J., Das, J., Daquila, G. L., and Täuber, U. C. *European Physical Journal B* **65**, 469 (2008).

[46] Maeda, A., Tsuboi, T., Abiru, R., Togawa, Y., Kitano, H., Iwaya, K., and Hanaguri, T. *Phys. Rev. B* **65**, 054506 (2002).

[47] Theodorakis, S. *Phys. Rev. B* **42**, 10172 (1990).

[48] Bulaevskii, L. N., Ledvij, M., and Kogan, V. G. *Phys. Rev. B* **46**, 366 (1992).

[49] Huse, D. A. *Phys. Rev. B* **46**, 8621 (1992).

[50] Bolle, C. A., Gammel, P. L., Grier, D. G., Murray, C. A., Bishop, D. J., Mitzi, D. B., and Kapitulnik, A. *Phys. Rev. Lett.* **66**, 112 (1991).

[51] Koshelev, A. E. *Phys. Rev. Lett.* **83**, 187 (1999).

[52] Dodgson, M. J. W. *Physica C: Superconductivity* **369**, 182 (2002).

[53] Dodgson, M. J. W. *Phys. Rev. B* **66**, 014509 (2002).

[54] Buzdin, A. and Baladié, I. *Phys. Rev. Lett.* **88**, 147002 (2002).

[55] Koshelev, A. E. *Phys. Rev. B* **68**, 094520 (2003).

[56] Koshelev, A. E. *Phys. Rev. B* **71**, 174507 (2005).

[57] Grigorieva, I. V., Steeds, J. W., Balakrishnan, G., and Paul, D. M. *Phys. Rev. B* **51**, 3765 (1995).

[58] Grigorenko, A., Bending, S., Tamegai, T., Ooi, S., and Henini, M. *Nature* **414**, 728 (2001).

[59] Grigorenko, A. N., Bending, S. J., Koshelev, A. E., Clem, J. R., Tamegai, T., and Ooi, S. *Phys. Rev. Lett.* **89**, 217003 (2002).

[60] Tonomura, A., Kasai, H., Kamimura, O., Matsuda, T., Harada, K., Yoshida, T., Akashi, T., Shimoyama, J., Kishio, K., Hanaguri, T., Kitazawa, K., Masui, T., Tajima, S., Koshizuka, N., Gammel, P. L., Bishop, D., Sasase, M., and Okayasu, S. *Phys. Rev. Lett.* **88**, 237001 (2002).

[61] Vlasko-Vlasov, V. K., Koshelev, A., Welp, U., Crabtree, G. W., and Kadowaki, K. *Phys. Rev. B* **66**, 014523 (2002).

[62] Tokunaga, M., Tamegai, T., Fasano, Y., and de la Cruz, F. *Phys. Rev. B* **67**, 134501 (2003).

[63] Tamegai, T., Matsui, M., and Tokunaga, M. *Physica C: Superconductivity* **412-414**, 391 (2004).

[64] Kirtley, J. R. and Wikswo, J. P. *Annual Review of Marerials Science* **29**, 117 (1999).

[65] Josephson, B. D. *Physics Letters* **1**, 251 (1962).

[66] Tinkham, M. *Introduction to Superconductivity.* Dover Publications, Inc., 2 edition, (1996).

[67] Van Duzer, T. and Turner, C. W. *Principles of Superconductive Devices and Circuits.* Prentice Hall PTR, 2 edition, (1999).

[68] Ginzburg, V. L. and Landau, L. D. *Zh. i. Teor. Fiz.* **20**, 1064 (1950).

[69] Feynman, R. P., Leighton, R. B., and Sands, M. *The Feynman Lectures on Physics*, volume 3. Addison-Wesley, (1965).

[70] Tonomura, A. *Jpn. J. Appl. Phys.* **34**, 2951 (1995).

[71] Tonomura, A., Kasai, H., Kamimura, O., Matsuda, T., Harada, K., Nakayama, Y., Shimoyama, J., Kishio, K., Hanaguri, T., Kitazawa, K., Sasase, M., and Okayasu, S. *Nature* **412**, 620 (2001).

[72] Sarma, N. V. *Philosophical Magazine* **17**, 1233 (1968).

[73] Träuble, H. and Essmann, U. *Journal of Applied Physics* **39**, 4052 (1968).

[74] Gammel, P. L., Bishop, D. J., Dolan, G. J., Kwo, J. R., Murray, C. A., Schneemeyer, L. F., and Waszczak, J. V. *Phys. Rev. Lett.* **59**, 2592 (1987).

[75] Goa, P. E., Hauglin, H., Baziljevich, M., Il'yashenko, E., Gammel, P. L., and Johansen, T. H. *Superconductor Science and Technology* **14**, 729 (2001).

[76] Bending, S. J. *Advances in Physics* **48**, 449 (1999).

[77] Oral, A., Bending, S. J., and Henini, M. *Applied Physics Letters* **69**, 1324 (1996).

[78] Kirtley, J. R., Ketchen, M. B., Stawiasz, K. G., Sun, J. Z., Gallagher, W. J., Blanton, S. H., and Wind, S. J. *Appl. Phys. Lett.* **66**, 1138 (1995).

[79] Koshnick, N. C., Huber, M. E., Bert, J. A., Hicks, C. W., Large, J., Edwards, H., and Moler, K. A. *Applied Physics Letters* **93**, 243101 (2008).

[80] Carneiro, G. and Brandt, E. H. *Phys. Rev. B* **61**, 6370 (2000).

[81] Kirtley, J. R., Tsuei, C. C., Moler, K. A., Kogan, V. G., Clem, J. R., and Turberfield, A. J. *Applied Physics Letters* **74**, 4011 (1999).

[82] Rugar, D., Budakian, R., Mamin, H. J., and Chui, B. W. *Nature* **430**, 329 (2004).

[83] Maze, J. R., Stanwix, P. L., Hodges, J. S., Hong, S., Taylor, J. M., Cappellaro, P., Jiang, L., Dutt, M. V. G., Togan, E., Zibrov, A. S., Yacoby, A., Walsworth, R. L., and Lukin, M. D. *Nature* **455**, 644 (2008).

[84] Taylor, J. M., Cappellaro, P., Childress, L., Jiang, L., Budker, D., Hemmer, P. R., Yacoby, A., Walsworth, R., and Lukin, M. D. *Nat Phys* **4**, 810 (2008).

[85] Maertz, B. J., Wijnheijmer, A. P., Fuchs, G. D., Nowakowski, M. E., and Awschalom, D. D. *Applied Physics Letters* **96**, 092504 (2010).

[86] Huber, M., Neil, P., Benson, R., Burns, D., Corey, A., Flynn, C., Kitaygorodskaya, Y., Massihzadeh, O., Martinis, J., and Hilton, G. *IEEE Transactions on Applied Superconductivity* **11**, 4048 (2001).

[87] Karrai, K. and Grober, R. D. *Appl. Phys. Lett.* **66**, 1842 (1995).

[88] Grober, R. D., Acimovic, J., Schuck, J., Hessman, D., Kindlemann, P. J., Hespanha, J., Morse, A. S., Karrai, K., Tiemann, I., and Manus, S. *Review of Scientific Instruments* **71**, 2776 (2000).

[89] Giessibl, F. J. *Applied Physics Letters* **73**, 3956 (1998).

[90] Eytan, G., Yayon, Y., Rappaport, M., Shtrikman, H., and Bar-Joseph, I. *Phys. Rev. Lett.* **81**, 1666 (1998).

[91] Eytan, G., Yayon, Y., Bar-Joseph, I., and Rappaport, M. L. *Ultramicroscopy* **83**, 25 (2000).

[92] Goa, P. E., Hauglin, H., Olsen, A. A. F., Baziljevich, M., and Johansen, T. H. *Review of Scientific Instruments* **74**, 141 (2003).

[93] Koblischka, M. R. and Wijngaarden, R. J. *Superconductor Science and Technology* **8**, 199 (1995).

[94] Soibel, A., Zeldov, E., Rappaport, M., Myasoedov, Y., Tamegai, T., Ooi, S., Konczykowski, M., and Geshkenbein, V. B. *Nature* **406**, 282 (2000).

[95] Soibel, A., Myasoedov, Y., Rappaport, M. L., Tamegai, T., Banerjee, S. S., and Zeldov, E. *Phys. Rev. Lett.* **87**, 167001 (2001).

[96] Banerjee, S. S., Goldberg, S., Soibel, A., Myasoedov, Y., Rappaport, M., Zeldov, E., de la Cruz, F., van der Beek, C. J., Konczykowski, M., Tamegai, T., and Vinokur, V. M. *Phys. Rev. Lett.* **93**, 097002 (2004).

[97] Soibel, A. *Visualization of vortex-lattice melting transition and transport current flow in Bi2Sr2CaCu2O8 with differential magneto-optical technique*. PhD thesis, Weizmann Institute of Science, (2000).

[98] Avraham, N. *Local magnetization measurements of high-temperature superconductors and single molecule magnets*. PhD thesis, Weizmann Institute of Science, (2007).

[99] Goldberg, S. *Inducing and Probing Long-range Order of the Vortex Matter in High-T_c superconductors*. PhD thesis, Weizmann Institute of Science, (2009).

[100] Kalisky, B. *Generation and Annealing of Transient Disordered Vortex States in High-Temperature Superconductors*. PhD thesis, Bar-Ilan University, Ramat Gan, Israel (2003).

[101] Lipson, S. G., Lipson, H., and Tannhauser, D. S. *Optical Physics*. Cambridge University Press, 3rd edition, (1995).

[102] Wijngaarden, R. J., Heeck, K., Welling, M., Limburg, R., Pannetier, M., van Zetten, K., Roorda, V. L. G., and Voorwinden, A. R. *Review of Scientific Instruments* **72**, 2661 (2001).

[103] Golubchick, D. *"Magneto-optical Imaging of Superconductors Out of Equilibrium."*. PhD thesis, Technion, Haifa, Israel, (To be published).

[104] Brandt, E. H. *Phys. Rev. B* **60**, 11939 (1999).

[105] Schmidt, B., Konczykowski, M., Morozov, N., and Zeldov, E. *Phys. Rev. B* **55**, R8705 (1997).

[106] Ooi, S., Shibauchi, T., Okuda, N., and Tamegai, T. *Phys. Rev. Lett.* **82**, 4308 (1999).

[107] Tamegai, T., Matsui, M., Yasugaki, M., Kamada, N., Tokunaga, Y., and Tokunaga, M. *Superconductor Science and Technology* **17**, S88 (2004).

[108] Goldberg, S., Segev, Y., Myasoedov, Y., Gutman, I., Avraham, N., Rappaport, M., Zeldov, E., Tamegai, T., Hicks, C. W., and Moler, K. A. *Phys. Rev. B* **79**, 064523 (2009).

[109] http://http://www.weizmann.ac.il/condmat/superc/.

[110] Blatter, G., Geshkenbein, V., Larkin, A., and Nordborg, H. *Phys. Rev. B* **54**, 72 (1996).

[111] Zeldov, E., Majer, D., Konczykowski, M., Geshkenbein, V. B., Vinokur, V. M., and Shtrikman, H. *Nature* **375**, 373 (1995).

[112] Fuchs, D. T., Doyle, R. A., Zeldov, E., Rycroft, S. F. W. R., Tamegai, T., Ooi, S., Rappaport, M. L., and Myasoedov, Y. *Phys. Rev. Lett.* **81**, 3944 (1998).

[113] Paltiel, Y., Fuchs, D. T., Zeldov, E., Myasoedov, Y. N., Shtrikman, H., Rappaport, M. L., and Andrei, E. Y. *Phys. Rev. B* **58**, R14763 (1998).

[114] Beidenkopf, H., Myasoedov, Y., Zeldov, E., Brandt, E. H., Mikitik, G. P., Tamegai, T., Sasagawa, T., and van der Beek, C. J. *Phys. Rev. B* **80**, 224526 (2009).

[115] Rosenstein, B. and Li, D. *Rev. Mod. Phys.* **82**, 109 (2010).

[116] Bouquet, F., Marcenat, C., Steep, E., Calemczuk, R., Kwok, W. K., Welp, U., Crabtree, G. W., Fisher, R. A., Phillips, N. E., and Schilling, A. *Nature* **411**, 448 (2001).

[117] Kalisky, B., Giller, D., Shaulov, A., and Yeshurun, Y. *Phys. Rev. B* **67**, 140508 (2003).

[118] Kalisky, B., Bruckental, Y., Shaulov, A., and Yeshurun, Y. *Phys. Rev. B* **68**, 224515 (2003).

[119] Giamarchi, T. and Bhattacharya, S. *Lecture Notes in Physics* **595**, 314 (2002).

תקציר

הדחף המניע את חקר הפיסיקה של מערבולות במוליכי-על הוא העובדה כי זוהי מערכת המדגימה עושר רב של תופעות הפיסיקליות אשר מקורן ביחסי הגומלין בין האינטראקציה בין המערבולות, אי הסדר, טמפרטורה ואפקטי שפה. על כן, מחקר מערכת המערבולות משמש להבנה של הפיסיקה של מערכות רב גופיות רבות אחרות. הכלי הניסיוני האידיאלי למחקר זה הינו מיקרוסקופיה מגנטית המאפשרת הבחנה במערבולות בודדות ובכך מדידה ישירה של הסדר של המערבולות, צפיפותן, הדינמיקה שלהן (במידה והחיישן מהיר דיו) וכמובן מאפשרת הבחנה בין תופעות שפה לתופעות תרמודינמיות אשר מקורן בגוף החומר.

לאחרונה, פותח חיישן ננו-מגנטי האפשר דימות מערבולות בתחום פרמטרים – צפיפות ורחב סרט-רחב בהרבה מזה הנגיש עד כה [1]. ההתקן הינו מסוג התקן התאבכות מוליך-על קוונטי, המנודף על קצה מחט חלולה, בעלת קוטר קצה של עשרות עד מאות ננו-מטרים. הגיאומטריה הפשוטה של ההתקן והרגישות הגבוהה שלו הופכים את החיישן למתאים ביותר למיקרוסקופיים מגנטיים סורקים. על ידי הצמדתו לקולן קוורץ פייזואלקטרי, יצרנו חיישן משולב, המסוגל לחוש את פני הדגם בנוסף לשדה המגנטי ובכך לאפשר הבאתו בצורה מבוקרת ננומטרים מפני הדגם. חיישן משולב זה מהווה את לב המיקרוסקופ המגנטי הסורק שפיתחנו. למיקרוסקופ זה רגישות מגנטית גבוהה ביותר, $1mG/\sqrt{Hz}$, ומסוגל בנקלה להבחין במערבולות מגנטיות במוליכי-על. להתקן המגנטי העשוי אלומיניום מספר חסרונות, אשר המשמעותית ביותר הינה טמפרטורת העבודה הנמוכה של החיישן, 300 מיליקלווין, אשר נגזרת מהטמפרטורה הקריטית הנמוכה של חומר זה. חסרון זה הניע את המאמץ לפתח חיישנים דומים ממוליכי-על בעלי טמפרטורה קריטית גבוה יותר, מאמץ אשר הצליח תוך שימוש בעופרת. הטמפרטורה הקריטית של מתכת זו, אינה רק מאפשרת עבודה באמצעים קריאוגניים פשוטים יותר, קרי ^{4}He , אלא גם מביאה לרגישות חיישנים גבוהה יותר. כתוצאה מכך, לחיישנים המגנטיים העשויים עופרת, רגישות גבוהה במעט פחות משני סדרי גודל מאלה העשויים אלומיניום, ועל כן רגישות לדיפול מגנטי בת $2\mu_B/\sqrt{Hz}$, אשר עקרונית מאפשרת הבחנה בספין אלקטרון בודד.

שריג מערבולות ג'וזפסון, הנוצרות עקב הפעלת שדה מגנטי מקביל במוליכי-על שכבתיים, מאופיין במערבולות רחבות ובקבועי שריג ארוכים המאפשרים דימות גם במיקרוסקופים מגנטיים רגישים

פחות. עובדה זו אפשרה לנו לדמֵּת (באופן עדיף) מערכת פיסיקלית זו בעזרת מיקרוסקופיה מגנטו-אופטית ולקבל תמונות ברורות של ערמות מערבולות הג'וזפסון במוליך-על מסוג BSCCO. כך, נתאפשר חקר השפעת מערבולות אלו על ההיסטרזיס המגנטי במוליך-על זה וכן על התכת שריג המערבולות הדו-מימדיות הנוצרות מהפעלת שדה מגנטי ניצב לשכבות הדגם. מצאנו כי ההיסטרזיס המגנטי, בתחום הפרמטרים בו הוא נובע ממחסום גיאומטרי על השפה, מדוכא משמעותית עקב המצאות שריג מערבולות ג'וזפסון. אלה, גורמות להנחתה מקומית ממשמעותית של מחסום הפוטנציאל על השפה, וכך יוצרים תעלות בהן מערבולות דו-מידיות יכולות להכנס ולצאת מהדגם בחופשיות. השפעת מערבולות הג'וזפסון על התכת שריג המערבולות דומה, אלא שכאן, מערבולות הג'וזפסון יוצרות שינוי מקומי בטמפרטורת (או שדה) ההתכה. תוצאותנו מראות כי שדה ההתכה, באזור בו ישנה ערימת מערבולות ג'וזפסון, נמוך בכ- 0.5 Oe לעומת הסביבה וכתוצאה מכך עם תחילת ההתכה נוצרות תעלות נוזל על גבי ערימות אלו.

במיקרוסקופיה המגנטו-אופטית, השתמשנו אף בכדי לדמֵּת את שלושת מעברי הפאזה במוליך-על מסוג BSCCO בסימום חסר, שני המעברים מסדר ראשון הנגרמים עקב פלוקטואציות תרמיות ואי סדר והמעבר מסדר שני המכונה מעבר הזכוכית. התפשטות מעברים אלו ברחבי הדגם הינה שונה מאד בשלוש המעברים, עובדה המעידה על כך שמעברים מושפעים מפגמים שונים ומאופיינים באורכים שונים. בנוסף, מצאנו כי צפיפות המערבולות סביב מעבר הזכוכית הינה מקסימלית, עובדה המעידה על יעילות מקסימלית של הצמדות מערבולות לאי הסדר במעבר זה.

Thesis for the degree
Doctor of Philosophy

Submitted to the Scientific Council of the
Weizmann Institute of Science
Rehovot, Israel

עבודת גמר (תזה) לתואר
דוקטור לפילוסופיה

מוגשת למועצה המדעית של
מכון ויצמן למדע
רחובות, ישראל

By
Yehonathan Segev

מאת
יהונתן שגב

מיקרוסקופיה מגנטית של פאזות המערבולות במוליכי על
Magnetic Microscopy of Vortex Phases in Superconductors

Advisor:
Prof. Eli Zeldov

מנחה:
פרופ' אלי זלדוב

January, 2011

שבט התשע"א